Combined plasmonic and electrochemical biosensing techniques based on gold nanopit arrays

Von der Fakultät für Elektrotechnik und Informationstechnik der Rheinisch-Westfälischen Technischen Hochschule Aachen zur Erlangung des akademischen Grades eines Doktors der Naturwissenschaften

genehmigte Dissertation

vorgelegt von

Ruifeng Zhu, M.Eng.

aus Anhui, China

Berichter:

Universitätsprofessor Prof. Dr. Sven Ingebrandt
Universitätsprofessor Prof. Dr. Andreas Offenhäusser

Tag der mündlichen Prüfung: 21. November 2024

Abstract

To overcome the signal recording uncertainties of single transducer sensor concepts and improve the reliability of the detection assay, innovative biosensing approaches are introduced through the development of dual-transducer aptamer-based sensors (aptasensors), specifically designed for the targeted detection of human serum albumin (HSA) and the SARS-CoV-2 Spike protein (S protein). The design integrates surface plasmon polaritons with electrochemical technology (SPP-EC) and plasmon-enhanced fluorescence with electrochemical technology (PEF-EC). This integration significantly enhances both the sensitivity and reliability of the sensors.

The SPP-EC dual-signal protocol was presented utilizing non-fully penetrating gold nanopit arrays (AuNpA) for combined extraordinary optical transmission (EOT)-based plasmonic detection and electrochemical sensing. It is worthy to note that these nanopit arrays, which do not fully penetrate the gold film, demonstrated narrower plasmonic peak width and refractive index sensitivity in both finite-difference time-domain (FDTD) simulations and experimental investigations than the fully penetrating nanohole arrays. This improvement is attributed to the effective shielding of the gold/quartz mode, together with an increase in the electrochemical active surface area. The aptasensor, modified with ferrocene (Fc)-labeled HSA aptamer receptors, undergo conformational changes upon binding events, influencing both electron transfer and SPP wavelength shift. Although both transducers monitor the same binding process, they exhibit different limit of detection (LOD), dynamic ranges, and sensitivities, highlighting the versatility of this approach for disease diagnostics and point-of-care (POC) testing.

Integrating plasmonic and electrochemical signal transduction mechanisms in a single biosensor can lead to improved accuracy and reliability in analyte detection. The advantages provided by the nanopit arrays, such as eliminating unwanted resonances and enhancing sensing performance, justified the effort put into development and optimization. However, the dynamic range of the SPP wavelength shift is not comparable with electrochemical detection. Further improvements in optical sensing capabilities could be achieved by optimizing the integration of additional transduction mechanisms, such as PEF utilizing the high electric fields generated between the noble metal and the surrounding media during excitation of SPP in proximity to the sample surface, potentially enabling highly sensitive detection.

Employing direct nanoimprint lithography (NIL), the AuNpA were fabricated with unexpected fringe structures. These structures enabled a SPP peak that overlapped with the excitation peak of the methylene blue (MB) fluorophore, associated with the C7 S protein aptamer. A significant enhancement in average fluorescence intensity, five and seven times higher over the AuNpA and fringe structures, respectively, compared to plain gold films (AuFilm), is observed. This dual-transducer system combines the advantages of PEF and EC measurements, utilizing MB as a dual transduction label. The aptasensor exhibits robust detection ranges for the SARS-CoV-2 S protein, with the PEF transducer offering a lower LOD and the EC transducer providing a broader concentration range.

Both dual-transducer aptasensors represent a significant advancement in the development of rapid and sensitive diagnostic tools. Their comprehensive characterization confirms high sensitivity and specificity, positioning these systems as competitive platforms for potential clinical applications. Therefore, it is a significant step forward in combined transducer biosensing technologies, offering a versatile diagnostic tool with broad implications for POC testing and epidemiological surveillance.

Contents

1 Introduction

Biosensor technology uses specific biorecognition elements, such as antibodies, antigens, proteins, entire viruses, nucleic acids, and aptamers, for precise detection of analytes [1]. Among these, aptamers stand out as promising candidates in biosensing and diagnostic applications. Aptamers are synthetic, single-stranded oligonucleotides that bind with high affinity and specificity to the target molecules. Their advantages are noteworthy, including small size, minimal batch-to-batch variation, cost-effectiveness, high stability under temperature fluctuations and chemical treatments, versatility in various applications, and reproducibility in synthesis [2]. Importantly, aptamers provide remarkable flexibility in structural design, enabling the development of innovative bioassays with enhanced affinity, sensitivity, and selectivity for specific targets. Up to now, numerous types of aptamer-based biosensors (aptasensors), including electrochemical, mass-sensitive, mechanical, and optical varieties, have been developed, each offering distinct advantages [3, 4]. Optical transducers, for instance, enable real-time monitoring of biosensing processes, while electrochemical aptasensors are known for their high sensitivity [5, 6]. Particularly in electrochemical aptasensors, redox groups or molecular beacons are commonly employed to signal the biomarker's binding to the aptamer receptor. Despite their widespread use, these redox-based signaling methods can be prone to false positives or negatives. Factors contributing to such inaccuracies include low aptamer/redox probe surface density, nonspecific binding by matrix molecules (biofouling), unwanted interactions between the redox probe and receptor molecules, and instability in the aptamer or blocking molecular receptor layer. Additionally, the degradation of the redox probe may falsely be interpreted as a target response, especially in electrochemical aptasensors with a "signal-off" mechanism, leading to potential false positives [7].

To address the limitations inherent in single-transducer sensor systems, researchers have introduced multi-transducer sensing concepts. These systems enable cross-verification of sensor outputs, thereby minimizing the risk of false-positive results, extending the detection range, and providing more comprehensive information about biological targets [8]. A significant focus in this area has been on combining surface plasmon resonance (SPR) with electrochemical (EC) responses to form SPR-EC systems, while SPR facilitates monitoring changes in optical properties near the gold surface, the same surface concurrently enables the recording of electrochemical processes within its Helmholtz layer. SPR is a technique that relies on the electromagnetic oscillation of electrons at a metal/dielectric interface, sensitive to changes in

the refractive index of adjacent materials [9]. In practical applications, substrates coated with a gold film based on the Kretschmann configuration [10], or substrates decorated with gold nanostructures to enable extraordinary optical transmission (EOT) [11, 12], are commonly used. Compared to the traditional Kretschmann configuration of SPR, the EOT configuration is suitable for biosensing applications by analyzing the transmission peaks variations in the spectrum of a thin metal film with efficiency surpassing that predicted by standard aperture theory, the technique utilizes a subwavelength grating of noble metal nanostructures, bypassing the need for the bulky prism coupling mechanism [13–15]. This innovation simplifies the instrumentation and ease alignment, which is essential for miniaturization. It enables straightforward integration into point-of-care (POC) setups and lab-on-a-chip systems, thus facilitating higher throughput for multiplexed analysis [16].

Human serum albumin (HSA) is a crucial protein in human blood plasma or serum, constituting about 30 to 50 g/L of the serum proteins [17–19]. Its levels are indicative of various health conditions, including coronary heart diseases, diabetes, and liver cirrhosis [20]. Despite its importance, traditional detection methods like the bromocresol green (BCG) assay have limitations in selectivity and sensitivity, especially in complex samples [21]. Therefore, developing accurate, selective methods for HSA detection is essential for both clinical medicine and biological research.

COVID-19, an acute respiratory disease caused by the SARS-CoV-2 virus, presents symptoms ranging from cough and fever to severe pneumonia and potential fatality [22]. The SARS-CoV-2 virus, a positive-sense single-stranded RNA virus with a genome of approximately 30 Kb, uses its Spike protein (S protein) for host cell entry, making it a critical target in COVID-19 diagnosis [23]. The S protein features two essential domains: the receptor-binding domain (RBD), which binds to the ACE2 receptor on human cells, and the fusion domain, facilitating cell-virus membrane fusion [24]. Current diagnostic methods for COVID-19 include CT imaging, nucleic acid tests, gene sequencing, lateral flow assays, and serological tests. The gold standard, however, is the reverse transcription-polymerase chain reaction test (RT-PCR), targeting the virus's genome in respiratory samples [1, 22, 25, 26]. Despite its accuracy, RT-PCR requires purified RNA and sophisticated equipment, presenting challenges in rapid and cost-effective testing [27]. Given these limitations, there is a urgent need for a rapid, affordable, and accessible diagnostic method that can detect the virus early in the incubation period, aiding timely treatment and reducing its spread.

In response to the challenges of signal recording uncertainties, a dual signal protocol was developed by combining an independent and complementary plasmonic transducer system with an electrochemical transducer (SPP-EC). This approach was demonstrated using gold nanohole arrays (AuNhA) for malaria biomarker detection [11]. However, the limited refractive index sensitivity of this system prompted us to optimize the gold structure's geometry to enhance

this sensitivity. Key geometrical parameters such as the symmetry and periodicity of the aperture array, hole diameter, and film thickness are crucial in the EOT configuration, allowing fine-tuning of spectral responses [28–30]. However, optimization efforts have primarily focused on fully penetrating hole geometries, which present challenges in biosensing applications due to closely spaced multiple resonance peaks in the EOT spectra, affecting the figure of merit (FOM). In initial investigations, the dual-transducer principle (SPP-EC) was employed using gold nanopit arrays (AuNpA) fabricated through nanoimprint lithography (NIL) using a Cr layer as hard mask. The geometry of AuNpA was optimized using results from finite-difference time-domain (FDTD) simulations to obtain sharper plasmonic spectral width, higher refractive index sensitivity, and a larger electrochemically active surface area compared with the AuNhA obtained by nanosphere lithography (NSL). These thin gold films perforated with hexagonal periodic arrays of nanopits, then modified with aptamer receptors, and were employed for HSA detection. The AuNpA serves a dual purpose: as the working electrode for electrochemical measurements and as the metal surface for recording SPP peak shifts in transmitted light correlated with analyte binding. This dual signal function aims to enhance diagnosis accuracy, reliability, and expand the detection range.

The Kretschmann SPR configuration is generally recognized for its superior analytical performance, particularly in terms of refractive index sensitivity when utilizing plasmonic wavelength shift mode, compared to the EOT configuration [13]. Hence, merely optimizing SPP geometries for enhanced sensitivity of SPP wavelength shifts might not be sufficient to fully harness the potential of the EOT setup. To increase the plasmonic sensing capabilities of the EOT configuration, a promising approach involves taking advantage of the intense electric fields generated between the noble metal and surrounding media during the excitation of SPP. This can amplify the fluorescence of fluorophores near the sample surface. The highly confined electromagnetic fields associated with surface plasmons (SP), which are collective oscillations of charge density at the metal surface, can be tailored to increase fluorescence intensity and reduce photo-bleaching, thereby boosting the plasmon-enhanced fluorescence (PEF). These capabilities are particularly advantageous for detecting trace amounts of analytes with improved limits of detection (LOD) [31,32]. In second investigation, plasmon-enhanced fluorescence with electrochemical measurements (PEF-EC) were combined innovatively to precisely monitor the binding events between the S protein and the C7 aptamer receptor. This approach utilizes an EOT configuration with AuNpA featuring fringe structures fabricated by direct NIL processes. These AuNpA were designed to align the SPP peak with the excitation wavelength of methylene blue (MB), enabling strong coupling effects that exploit plasmonic properties to amplify the fluorescence signal. MB, known for its dual functionality as both a redox reporter in electrochemical aptasensors and a fluorescence probe emitting light in the near-infrared region, offers a unique advantage in this dual-signal biosensor setup [33,34]. It is envisioned that MB can be serve as a dual probe for both electrochemical and fluorescence

transduction as its reversible redox propterties and concurrent fluorescence emission. Unlike previous studies, such as Chang et al. [8], which did not incorporate PEF and instead utilized intrinsic fluorescence of MB released from MB@ZIF-90 in bulk solution, the MB in this work was attached to the C7 S protein aptamer (labeled as S2_20T_MB) and hybridized with a specially designed single-stranded DNA (ssDNA) molecule (S1) equipped with a dual-thiol group. By monitoring surface-associated binding processes through the PEF-EC systems, sensor not only enhances performance but also offers deeper insights into the physicochemical processes occurring at the solid-liquid interface, marking a significant advancement in dual-transducer aptasensor technology.

2 Fundamentals

2.1 Fundamentals of surface plasmon resonance

The nature of plasma (ionized gas in the tube) was observed by Thomson in 1897. Towards the end of the 1920s, Langmuir introduced the term "plasma" and elucidated the charge density waves in plasma through his observations [35]. Both the ionosphere and metals serve as instances of plasmas, characterized by the presence of freely moving charges [36]. In the realm of solid-state physics, plasmons represent the quantum description of the collective oscillations of free electrons in a solid matrix. These are often conceptualized as "quantized plasma" (charge density) waves [37]. The phenomena of electron plasma are particularly significant in metals that exhibit free-electron-like properties. For such materials, the frequency (ω) dependent dielectric function can be modeled as $\varepsilon_m(\omega) = 1 - (\omega_p/\omega)^2$, where $\varepsilon_m(\omega)$ is the complex dielectric constant of the meta, ω_p is the plasma frequency, representing the frequency of bulk longitudinal electron excitations [38–40].

Surface plasmons (SP) result from the interaction of electromagnetic radiation with free electrons distributed on a metal surface, leading to the collective oscillation of these free electrons [41]. SP are the electron plasma oscillations near a metal surface, arising from the broken translational invariance perpendicular to the surface. Similar effects related to collective two-dimensional free-electron excitations significantly contribute to the electromagnetic characteristics of diverse systems, such as semiconductor surfaces and electrons over a liquid helium surface. The frequency ω_{SP} of a surface plasmon on a flat surface of semi-infinite metal can be easily determined from the frequency of a bulk plasmon of metal, as it corresponds to $\operatorname{Re}\varepsilon_m(\omega_{SP}) = -\varepsilon_i$, where $\varepsilon_i > 0$ is the dielectric constant of the adjacent dielectric medium. For a free-electron metal in contact with a vacuum, $\omega_{SP} = \omega_p/\sqrt{2}$. Various surface effects and non-local (spatial dispersion) effects in real metals can introduce corrections to the surface plasmon frequency [39].

Surface plasmon resonance (SPR) refers to the collective oscillations of the conduction electrons in metallic nanostructures. Both the intensity and the position of the SPR strongly depend on the size, shape, and composition of the nanostructures, as well as the dielectric properties of the surrounding environment [42]. SPR occurs in two distinct forms: propagating surface plasmon polaritons (SPP) and localized surface plasmon resonance (LSPR).

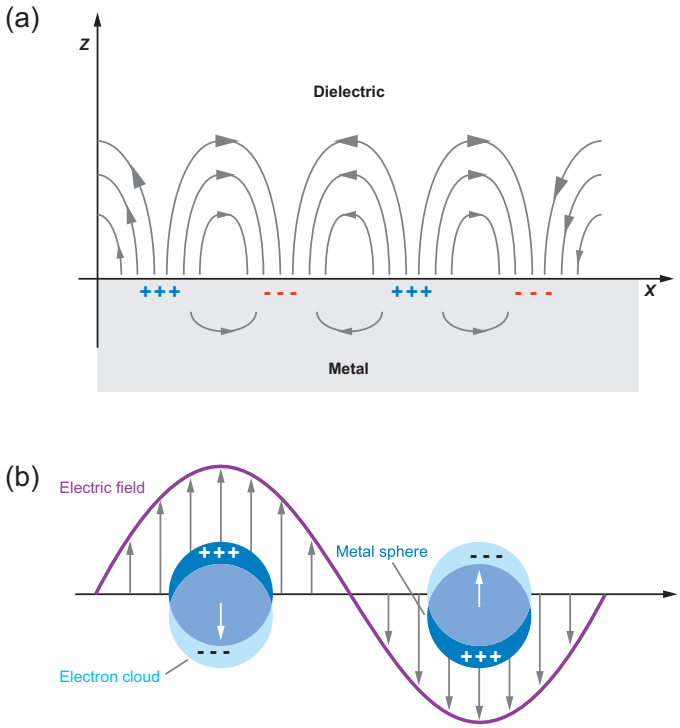

Figure 2.1: Schematic diagrams illustrating of SPP (a) and LSPR (b). Adapted from reference [42].

The SPP are the propagating charge oscillations on the surface of thin metal films. SPP cannot be excited by free-space radiation; instead, they require momentum matching, such as through periodicity in a nanostructure, for resonance excitation. LSPR occurs when the dimensions of a metallic nanostructure are less than the wavelength of incident light, leading to collective but non-propagating oscillations of surface electrons in the metallic nanostructure [43].

SPP and LSPR are both plasma oscillations of electrons at surfaces. However, they differ in terms of the way in which they interact with light [44]. Figure 2.1 provides a visual representation highlighting the charge distribution disparity between SPP and LSPR. In the context of SPP, these plasmons propagate in the x- and y-directions along the metal-dielectric interface, covering distances on the order of tens to hundreds of microns. Simultaneously, they decay evanescently in the z-direction, with $1/e$ decay lengths approximately on the order of 200 nm. The interaction between the metal surface-confined electromagnetic wave and a molecular surface layer induces shifts in the plasmon resonance condition. For the case of localized surface plasmons, light interacts with particles significantly smaller than the incident wavelength, resulting in a plasmon that oscillates locally around the nanoparticle at a frequency referred to as the LSPR. Similar to the SPP, the LSPR is also sensitive to changes in the local dielectric environment [42]. Both phenomena enable enhanced light-matter

interactions due to their ability to concentrate electromagnetic fields at very small scales. The properties of SPP and LSP can be tuned by varying the geometry of the structure, making them attractive for many applications such as biosensing and optical communication systems [44].

2.1.1 Surface plasmon polaritons

Under appropriate illumination conditions, the excitation of SPP induces an alternate distribution of positive and negative charges along the metal surface, resulting in the generation of forward-propagating energy (Figure 2.1a). The decay of this energy occurs due to factors such as metallic losses. The collective oscillation of charges can excite electric fields on both sides of the metal-dielectric interface, leading to the enhancement of electric fields in proximity to the metal surface. The strength of the electric field associated with SPP experiences exponential decay into both the dielectric side and the metal itself, each characterized by a distinct decay length. It is evident that SPP falls within the category of evanescent fields. The penetration depth into the dielectric side (δ_{d}) and the metal side (δ_{m}) is defined by [45]:

$$\delta_{\mathrm{d}} = \frac{\lambda_{\mathrm{spp}}}{2n} \tag{2.1}$$

$$\delta_{\mathrm{m}} = \frac{\lambda_{\mathrm{spp}}}{2\pi} \tag{2.2}$$

Here, λ_{spp} is the plasmon frequency, and n is the refractive index of the dielectric side. Examination of Equations 2.1 and 2.2 easily reveals that δ_{m} is typically smaller than δ_{d} due to a smaller value of n than π in the denominator.

Much can be understood about SPP by examining their dispersion relation, the relationship between the angular frequency (ω) and in-plane wavevector of SPP modes. The in-plane wavevector is the wavevector of the SPP in the plane of the surface along which it propagates, which is given by [45]:

$$k_{\mathrm{spp}} = n_{\mathrm{spp}} k_0 \tag{2.3}$$

Where $k_0 = \frac{\omega}{c}$ is the free-space propagating wavevector in Equation 2.3, c represents the speed of light in vacuum, and n_{SPP} is the refractive index of the SPP.

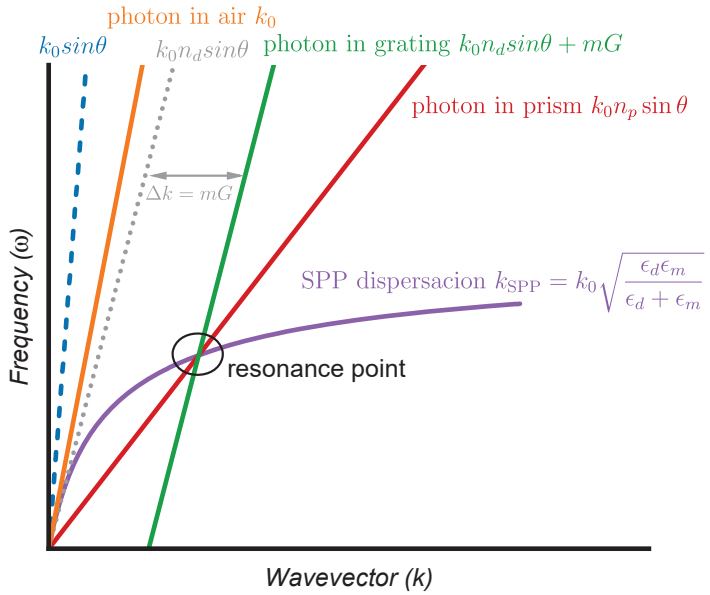

Figure 2.2: Dispersion relation of Kretschmann and grating based SPP excitation configuration (Blue and gray dashed lines are presented here for reference).

$$n_{\text{spp}} = \frac{c}{v_{\text{spp}}} \tag{2.4}$$

In Equation 2.4, v_{SPP} is the phase velocity of SPP. Consequently, the relationship presented in Equation 2.5 is derived:

$$v_{\text{SPP}} = \frac{c}{\sqrt{\varepsilon_{\text{SPP}}}}, \tag{2.5}$$

Here, $\varepsilon_{\text{spp}} = \frac{\varepsilon_{\text{d}}\varepsilon_{\text{m}}}{\varepsilon_{\text{d}}+\varepsilon_{\text{m}}}$ is the effective relative permittivity experienced by the SPP. ε_d and ε_m are the relative permittivity of the dielectric and metal adjacent to the interface, respectively. Consequently, Equation 2.6 is derived from the above relations [41,46]:

$$k_{\text{SPP}} = \frac{\omega}{c}\sqrt{\frac{\varepsilon_d \varepsilon_m}{\varepsilon_d + \varepsilon_m}}. \tag{2.6}$$

Where $\varepsilon_d = n_d^2$, with n_d being the refractive index of the dielectric. As can be seen from Equation 2.6, for real values of k_{SPP}, it is necessary to have $\varepsilon_m < 0$ and $|\varepsilon_m| > \varepsilon_d$, the square root term is generally greater than 1 and positive. Some metals, such as gold and silver, satisfy this condition [47]. On the other hand, simply shining light on a smooth metal surface may not excite SP, as the wavevector of photons in free space, denoted as k_0, is smaller than that of SP, as illustrated in the dispersion relation curve (Figure 2.2). Thus, there exists a mismatch

between the momenta of the incident light photon and SPP for the same frequency in free space. Therefore, Kretschmann and grating coupling mechanisms were proposed to increase the wavevector of incident light in the dielectric medium (as given by Equation 2.7) to achieve the necessary matching conditions for the excitation of SP.

$$k = k_0\sqrt{\varepsilon_\mathrm{d}} = \frac{2\pi}{\lambda}n_\mathrm{d} \tag{2.7}$$

In the case of the Kretschmann configuration, employing the attenuated total reflection (ATR) method, a transverse magnetic (TM) polarized light reaching the metallic surface from the prism possesses a wavevector component parallel to the surface. Therefore, the wavevector of the incident light undergoes modification as:

$$k_x = \frac{2\pi}{\lambda}\sqrt{\varepsilon_\mathrm{p}}\sin\theta \tag{2.8}$$

Where k_x is in-plane wavevector, θ is the angle of incidence in the prism, and ε_p is the permittivity of the prism. The resonance angle under the condition of resonance is derived from Equations 2.6 and 2.8 as follows:

$$\theta_\mathrm{r} = \sin^{-1}\left(\frac{1}{\sqrt{\varepsilon_\mathrm{p}}}\sqrt{\frac{\varepsilon_\mathrm{m}\varepsilon_\mathrm{d}}{\varepsilon_\mathrm{m}+\varepsilon_\mathrm{d}}}\right) \tag{2.9}$$

Where θ_r is the coupling angle, commonly known as the resonance angle. This angle is where the resonance condition is met, and it is highly sensitive to the dielectric properties of the surrounding media. Therefore, it is extensively exploited for applications in plasmonic sensing and biosensing purposes.

Despite the high performance of these structures, the reliance on prism couplers for SPR excitation poses challenges for on-chip integration [46, 48]. As an alternative, diffraction is employed to couple light to SPR modes through a diffraction grating. In this case, light is split into a series of beams with $k_d = k_x + mG$, where k_d is the wavevector of the diffracted light, k_x is the original x-component of wavevector of the incident light ($k_x = k_0 n_d \sin\theta$), G stands for the wavenumber of the grating ($G = 2\pi/\Lambda$, with m $= 0, \pm1, \pm2, \ldots$ and Λ being the diffraction order and the period length of the grating, respectively), and n_d is the dielectric refractive index. The wavevector matching condition in this case is expressed as:

$$k_0 n_d \sin\theta + \frac{2\pi}{\Lambda}m = k_0\sqrt{\frac{\varepsilon_\mathrm{m}\varepsilon_\mathrm{d}}{\varepsilon_\mathrm{m}+\varepsilon_\mathrm{d}}} \tag{2.10}$$

Similar to the prism coupler approach, these plasmonic grating structures have also been used for sensing and biosensing applications [46, 49, 50].

2.1.2 Localized surface plasmon resonance

LSPR is an optical phenomenon that induces a collective oscillation of valence electrons, leading to subsequent absorption within the ultraviolet-visible (UV-Vis) band due to interactions between incident photons and the conduction band of metallic nanoparticles or other finite structures (Figure 2.1b). In this case, the harmonic oscillation of the electric field of light induces oscillation in the free-electron density on the metal surface, analogous to a forced harmonic oscillator [46].

LSPR can be described by Mie's solution to Maxwell's equations, occurring as a consequence of the confinement to the movement of electrons through the internal lattice of a noble metal when the size of the noble metal structure is scaled down to the nanoscale (<100 nm). Equation 2.11 illustrates the dependence of extinction, $E(\lambda)$, on the dimension, shape, density, and local environment of the nanostructure:

$$E(\lambda) = \frac{24\pi N_{\mathrm{A}} a^3 \varepsilon_{\mathrm{m}}^{3/2}}{\lambda \ln(10)} \left[\frac{\varepsilon_{\mathrm{i}}}{\left(\varepsilon_{\mathrm{r}} + \chi \varepsilon_{\mathrm{m}}\right)^2 + \varepsilon_{\mathrm{i}}^2} \right] \tag{2.11}$$

Where N_A is the areal density of the nanostructure, a is the radius of the nanostructure (modeled as a sphere), λ is the wavelength of the absorbing radiation, ε_m is the dielectric constant of the medium surrounding the nanostructure (assumed to be a positive, real integer and wavelength-independent), ε_i is the imaginary portion of the nanostructure's dielectric function, ε_r is the real portion of the nanostructure's dielectric function, and χ is the term used to describe the aspect ratio of the nanostructure, and is assigned a magnitude of two for a spherical particle and can be as large as 20 for particles with high aspect ratios such as nanorods [51, 52].

LSPR differs from SPP in that the induced plasmons oscillate locally to the nanostructure rather than along the metal-dielectric interface. The difference in SPP and LSPR leads to changes in optical configurations, LSPR measures wavelength absorbed by binding sites of resonantly oscillating electrons of nanoparticles and gives a peak in the absorbance spectrum [51, 53, 54]. LSPR spectroscopy offers sensing through the transduction of refractive index changes in close proximity to the surface of the noble metal nanostructure. The formation of adlayers and biorecognition events on the surface induces quantifiable shifts in the LSPR extinction wavelength maximum, λ_{max}, due to the dependence of the adlayer refractive index, n, as demonstrated by Equation 2.12:

$$\Delta\lambda_{\max} = m\Delta n \left[1 - \exp\left(-\frac{2d}{l_d}\right)\right] \tag{2.12}$$

Where m represents the bulk refractive index response of the nanostructure, d is the effective adsorbate layer thickness, and l_d is the characteristic electromagnetic field decay length, modeled as an exponential decay. The binding kinetics can then be monitored by tracking $\Delta\lambda_{\max}$ as a function of either time or analyte concentration [51].

2.2 Plasmon-enhanced fluorescence

The investigations of plasmon-enhanced fluorescence (PEF) began in the 1960s when Drexhage discovered that a fluorescent molecule in close proximity to a metallic film displays modified decay times and angular distribution. Interest in PEF intensified following the groundbreaking works of Lakowicz and Geddes, who investigated scenarios in which a fluorophore is positioned at a nanometer-scale distance from metallic structures, and where the absorption and/or emission bands of the fluorophore overlap with the plasmonic band of the metallic structure [55–57].

PEF is also known as surface-enhanced fluorescence (SEF), or metal-enhanced fluorescence (MEF). Until now, a standardized naming convention for this type of sensor does not exist. The PEF research was relatively inactive before 2007, but since then, many nanostructures have been studied to plasmonically enhance fluorescence, coinciding with the rise of controllable nanoparticle synthesis and lithography-based fabrication of nanostructured chips. The rapid development of PEF sensors in the future is conceivable given the recent trends in nanofabrication and advancements in the understanding and theory of PEF [43].

2.2.1 The principle of plasmon-enhanced fluorescence

PEF occurs through the enhancement of quantum efficiency and photostability of fluorophores. When a fluorophore is located in the proximity of a metallic nanostructure, the free electrons within the metal surface couple with the electrons of the fluorophore, and both the emission and excitation characteristics of the fluorophore undergo modifications. The metal here can be considered as an optical antenna, creating hot spots where electromagnetic radiation can be confined. This can be easily comprehended by considering the simplified Jablonski diagram (Figure 2.3) [58].

In the absence of a metal, a fluorophore is excited from the ground state (S_0) to the excited states (S_1, S_2, etc.). Subsequently, internal conversion occurs as the fluorophores relax to

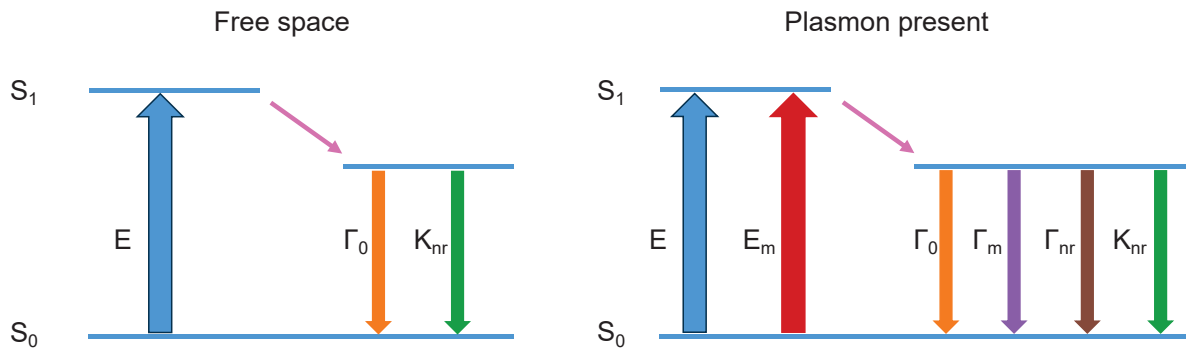

Figure 2.3: Simplified Jablonski diagram for the free-space condition (left) and the modified form in the presence of metallic nanostructure (right).

lower vibrational states, leading to the emission of energy as fluorescence and a return to the ground state. Additionally, spin conversion may take place, causing transitions from the singlet to the triplet state (T_1 - not displayed). Both processes result in a radiative decay rate (Γ_0). In addition, non-radiative decay (k_{nr}) is present, and a quenching process (rate k_q - not displayed) may occur. The fluorescence lifetime is measured as the time the fluorophore spends in an excited state before returning to its original ground state. The quantum yield defines the number of times fluorescence occurs per photon absorbed by the system (Q_0). During this process, the overall fluorescence rate can be expressed as the product of both the excitation rate and the quantum yield. This phenomenon can be mathematically expressed using well-documented formulae [43, 58, 59]:

$$Q_0 = \Gamma_0 \tau_0 \tag{2.13}$$

$$\tau_0 = \frac{1}{\Gamma_0 + k_{\mathrm{nr}}} \tag{2.14}$$

Equations 2.13 and 2.14 demonstrate the quantum yield (Q_0) and lifetime (τ_0) for an isolated fluorophore in free space.

In the presence of an optical antenna, the fluorophore is excited at a wavelength λ_{ex} when exposed to incident light. The near field around a metal can further excite a nearby fluorophore, leading to emission at an emission wavelength, λ_{em}. Once excited, the fluorophore undergoes either radiative or non-radiative transitions, releasing excess energy in the form of a photon (light) or a phonon (vibration), respectively [60]. Similar to standard fluorescence, photon emission then experiences radiative (Γ_0) or non-radiative decay (k_{nr}). PEF can be considered a coupled system between a fluorophore and a metallic nanostructure. In this system, when a metal is present beyond the quenching distance, the decay rate is modified to ($\Gamma_0 + \Gamma_m$), where Γ_m represents the modified decay rate in the presence of the metal. Importantly, the metal

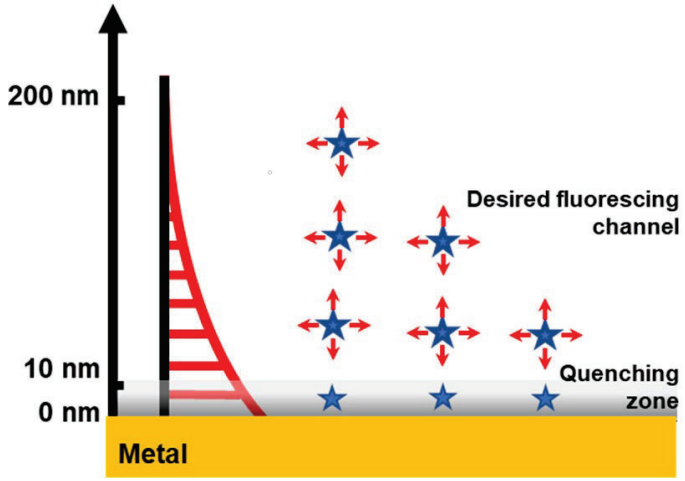

Figure 2.4: Main channels interact with the fluorophores on a metallic surface. The short distance is the fluorescence quenching channel. A desired fluorescing channel out of this range can excite the localized fluorophores. The intensity of an optical field decays exponentially into a bulk medium. Adapted from reference [62].

modifies the radiative decay rate and creates new channels of non-radiative decay through energy and charge transfer between the fluorophore and the metal. Consequently, there is an increase in quantum yield and a decrease in lifetime. The modified quantum yield (Q_m) and the lifetime (τ_m) may therefore be expressed as [58, 61]:

$$Q_{\mathrm{m}} = \frac{\Gamma_0 + \Gamma_{\mathrm{m}}}{\Gamma_0 + \Gamma_{\mathrm{m}} + \Gamma_{\mathrm{nr}} + k_{\mathrm{nr}}} \tag{2.15}$$

$$\tau_m = \frac{1}{\Gamma_0 + \Gamma_{\mathrm{m}} + \Gamma_{\mathrm{nr}} + k_{\mathrm{nr}}} \tag{2.16}$$

2.2.2 The influencing factors of plasmon-enhanced fluorescence

The phenomenon of PEF involves complex interactions between metallic nanostructure and luminophores, governed by mechanisms such as Förster Resonance Energy Transfer (FRET) and the Purcell effect. The key to understanding and optimizing PEF lies in controlling the distance between the luminophore and metal surface [63].

The energy transfer between the plasmon and the fluorophore is dominated by dipole-dipole interactions, with the exact mechanism being determined by the separation distance. First, if the plasmon and the fluorophore are within ∼1-10 nm of each other, the non-radiative local field of one dipole can excite the second one. This is known as FRET. The efficiency of energy transfer in FRET depends on two factors [64].

$$\mathrm{Eff}_{\mathrm{FRET}} = \frac{1}{1 + \left(\frac{R}{R_0}\right)^6} \tag{2.17}$$

The separation distance, R, which decays as $1/R^6$ because each dipole has a $1/R^3$ near field. The distance behavior is scaled by the factor R_0, which depends on the spectral overlap between the emission of the donor's excited state and the acceptor's ground state absorption. Typically, the value of R_0 ranges from 3 to 8 nm in plasmon/fluorophore FRET. The FRET process is very efficient, approaching 100% for $R < R_0$ because of the amplified electric field. FRET can occur from plasmon to fluorophore or from fluorophore to plasmon.

Secondly, the plasmon can enhance the radiative rate of the fluorophore through the Purcell effect. The Purcell effect can be understood as follows. If a radiative dipole is placed in a resonant cavity, the emission intensity will be amplified on-resonance and quenched off-resonance when compared to free space. This is because the cavity modifies the local density of optical states (LDOS) as follows [65]:

$$\rho_{\mathrm{LDOS}}(\omega) \sim |E_{\mathrm{loc}}(\omega)|^2 \tag{2.18}$$

Where $|E_{\mathrm{loc}}(\omega)|^2$ is the local electric field of the cavity normalized to the incident intensity. In air, the LDOS is nearly constant and the dipole radiates at all emission energies. In the cavity, the LDOS is peaked at the resonance wavelength, and the dipole can emit into this mode at a higher rate than in air alone, like coupling into an antenna. The cavity can then re-radiate the transferred energy, resulting in an overall enhancement of the dipole's emission.

When the absorption spectrum of the luminophore overlaps with the SPR of metallic nanostructure, FRET and the Purcell effect come into play. FRET dominates at short distances (< 10 nm), while the Purcell effect becomes significant at longer distances ($10 - 50$ nm). The excitation enhancement is primarily determined by FRET at distances of a few nanometers, as the Purcell enhancement for plasmon radiation is usually negligible due to the low LDOS at long distances.

In the case where the luminophore emission spectrum overlaps with the SPR of metallic nanostructure and the distance is more than ~ 10 nm, FRET is not effective, but the Purcell effect strongly enhances luminescence emission. Conversely, if the emission spectrum of the luminophore overlaps with the SPR, but the distance is small, FRET quenches luminescence emission. Therefore, maintaining a controlled distance between the luminophore and metallic nanostructure is crucial for achieving a powerful PEF effect as illustrated on Figure 2.4.

To optimize PEF, various spacer layers, including inorganic (e.g., silica, alumina) and organic spacers (e.g., aptamers, antibodies, DNA), have been developed to precisely control the distance between the luminophore and metallic nanostructure. The choice of spacer layers involves a trade-off, considering their unique advantages and disadvantages.

The shape of metallic nanostructure also influences luminescence enhancement. Metallic nanostructure with sharp corners and edges generate intense electric fields, enhancing luminescence intensity under resonance excitation, such as nanodisks, nanotriangles, and nanoholes and disordered nanostructures such as nanorods and nanoislands. The choice of these nanostructure depends on factors like scattering efficiency and biocompatibility [60, 63, 65].

In summary, the intricate interplay between FRET, the Purcell effect, spacer layers, and the choice of metal nanostructure defines the dynamics of PEF, offering a platform for designing highly responsive sensors and applications in various fields [43,65].

2.3 Fundamentals of electroanalytical chemistry

2.3.1 The electrical double layer

A biosensor, defined as devices capable of delivering qualitative and/or quantitative insights into biomolecular interactions, consists of four main elements, a target, a receptor, a transducer and a signal processing system as illustrated in Figure 2.5. A biological recognition element generally consists of an immobilized biocomponent that is able to detect the specific target analyte. The transducer on the other hand is a converter. The reaction between the target and bioreceptor bring about chemical changes such as the production of a new chemical molecules, release of heat, flow of electrons and changes in pH or mass. The biochemical signal is converted into an electrical signal by the transducer. Eventually, the electrical signal is amplified and sent to a microelectronics and data processor. A measurable signal is produced, such as a digital display, a print-out or an optical change [66].

In electrochemical biosensors, the reaction under investigation would either generate a measurable current (amperometric), a measurable potential or charge accumulation (potentiometric), or a measurable impedance (both resistance and reactance) [67], and the electrodes function as interfaces between electrical and biological compartments of the hybrid system. Modification of an electrode with affinity reagents, such as antibodies or aptamers, allows the design of interfaces that specifically bind to biomolecular analytes of interest. However, the sensitivity of biosensors is constrained by the screening of electric fields by mobile ions.

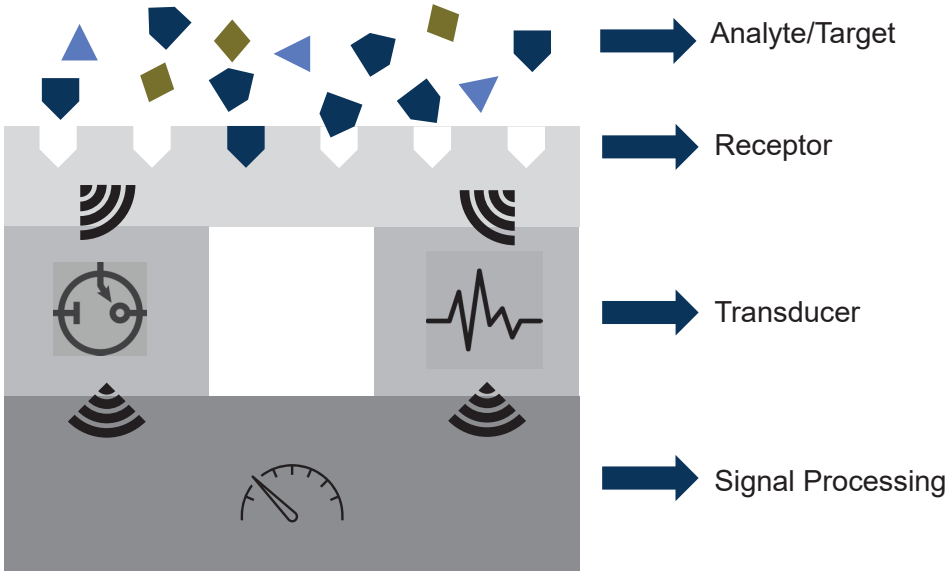

Figure 2.5: Schematic representation of a biosensor. The biosensor primarily consists of four major components: the analyte/target, receptor, transducer, and signal processing.

Since all biological samples contain high concentrations of such ions, the electrostatic screening effect can significantly attenuate biosensor signals. This fundamental physical effect, known as the electrical double layer (EDL), hinders the broad utility of many detection platforms [68].

The concept of the EDL's existence at the surface of a metal in contact with an electrolyte emerged in 1879 (Helmholtz). The initial theoretical model assumed the presence of a compact layer of ions in contact with the charged metal surface (Figure 2.6a) [69]. However, the Helmholtz model did not consider the thermal motion of ions in the solution, as considered for ion-ion interaction in the Debye-Hückel model. Building on this, Gouy and Chapman proposed the diffuse layer model, where the accumulated ions, influenced by the Boltzmann distribution, extend to some distance from the solid surface. The total charge of the diffuse layer is expected to be the same as the electrode surface for electroneutrality.

Taking into account the thermal motion of particles, the populations of cations and anions can be described by Boltzmann distributions:

$$N_{\pm} = N_{\pm}^{\infty} \exp\left(-\frac{z_{\pm} e \Psi}{k_B T}\right) \tag{2.19}$$

Where N_+ is associated with the cation population, N_- with the anion population, $N_{\pm}^{\infty}$ with the bulk ion population, and $z_{\pm}$ with the ion charge number; e is the electron charge, k_B is the Boltzmann constant, and T is the temperature. The charge density (ρ) is expressed as:

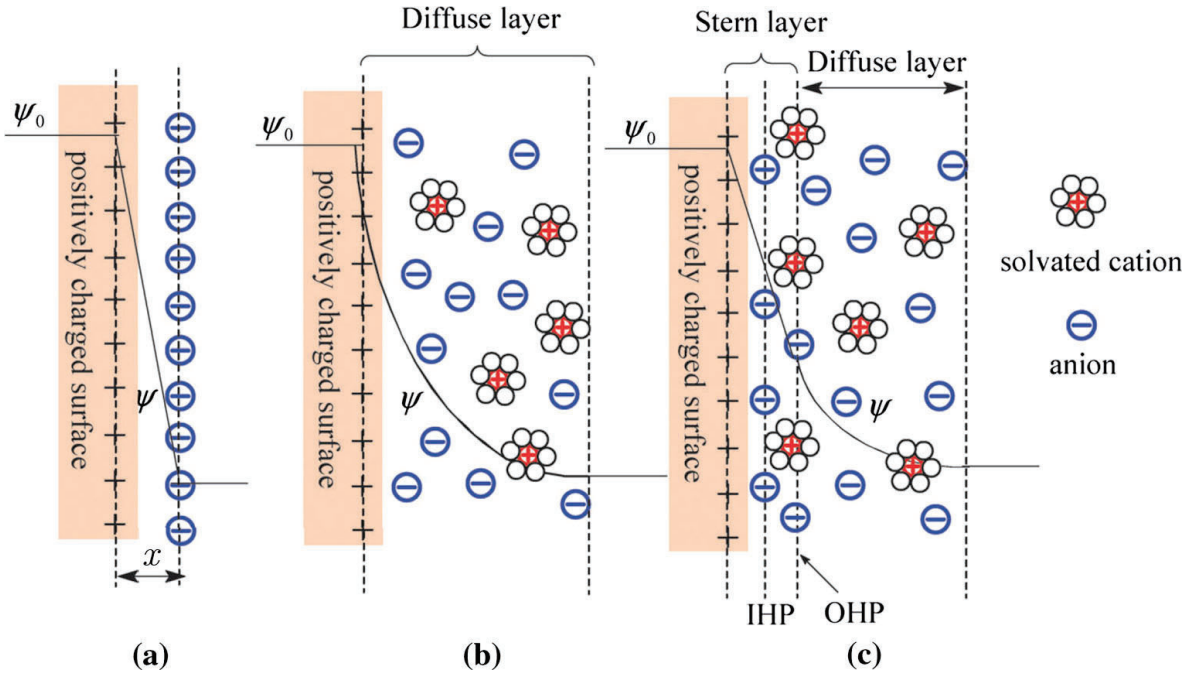

Figure 2.6: Models of the electrical double layer at positively charged surface: the Helmholtz model (a), the Gouy-Chapman model (b), and Grahame's adaptation of Stern model (c) showing the inner Helmholtz plane (IHP) and outer Helmholtz plane (OHP). x is the double-layer distance described by the Helmholtz model. Ψ_0 and Ψ are the potentials at the electrode surface and the electrode/electrolyte interface, respectively. Reproduced from reference [70].

$$\rho = \sum N_{\pm} z_{\pm} e \tag{2.20}$$

Substituting Equation 2.19 in 2.20:

$$\rho = \sum \left[N_{\pm}^{\infty} z_{\pm} e \exp\left(-\frac{z_{\pm} e \Psi}{k_B T} \right) \right] \tag{2.21}$$

The Poisson equation for a plane is:

$$\frac{d^2\Psi}{dx^2} = \frac{-\rho}{\varepsilon} \tag{2.22}$$

With ε being the liquid's permittivity and x related to the distance from the electrode surface. In this way, the Poisson-Boltzmann equation is reached when Equation 2.21 is substituted in 2.22:

$$\frac{d^2\Psi}{dx^2} = -\sum \left[\frac{N_{\pm}^{\infty} z_{\pm} e}{\varepsilon} \exp\left(-\frac{z_{\pm} e \Psi}{k_B T} \right) \right] \tag{2.23}$$

The kinetic energy of ions is attributed to thermal motion. If this quantity exceeds the expected electric potential energy, expressed as $k_BT \gg |ze\Psi|$, the exponential term in Equation 2.23 can be expanded in a polynomial form and truncated in the second term, linearizing the equation:

$$\frac{d^2\Psi}{dx^2} = -\sum\left(\frac{N_{\pm}^{\infty} z_{\pm} e}{\varepsilon}\right) + \sum\left(\frac{N_{\pm}^{\infty} z_{\pm} e}{\varepsilon}\right)\left(\frac{z_{\pm} e\Psi}{k_BT}\right) \tag{2.24}$$

The first term on the right-hand side of Equation 2.24 is associated with the total charge of the electrolyte bulk, a quantity recognized to be zero due to the maintenance of electroneutrality. Consequently, it becomes feasible to simplify Equations 2.24 to 2.25:

$$\frac{d^2\Psi}{dx^2} = \sum\left(\frac{N_{\pm}^{\infty} z_{\pm} e}{\varepsilon}\right)\left(\frac{z_{\pm} e\Psi}{k_BT}\right) \tag{2.25}$$

After some rearrangement [71]:

$$\frac{d^2\Psi}{dx^2} = \frac{e^2\Psi}{\varepsilon k_BT}\sum N_{\pm}^{\infty} z_{\pm}^2 \tag{2.26}$$

This is known as the linearized Poisson-Boltzmann equation or the linear Poisson-Boltzmann equation. This reflects the fact that the full Poisson-Boltzmann equation has been linearized by expanding the exponential and only keeping the term in the expansion that is linear in the potential, Ψ [72]. Since Equation 2.26 is a second order differential equation, it will require two boundary conditions to solve. One solution for the differential equation is:

$$\Psi = A\exp\left(-x\sqrt{\frac{e^2}{\varepsilon k_BT}\sum N_{\pm}^{\infty} z_{\pm}^2}\right) + B\exp\left(x\sqrt{\frac{e^2}{\varepsilon k_BT}\sum N_{\pm}^{\infty} z_{\pm}^2}\right) \tag{2.27}$$

The boundary conditions are $\Psi(x = 0) = \Psi_0$ and $\Psi(x = \infty) = 0$. The first condition is a definition of the "surface potential". This is the potential at the physical surface of the solid with respect to the bulk solution. The second boundary condition sets the potential in the bulk solution, assumed to be at an infinite distance from the surface, to be zero. Doing so sets the reference point of the potential scale for this system to a point within the bulk solution. Plugging these into Equation 2.27 yields $A = \Psi_0$ and $B = 0$ [72]. Therefore,

$$\Psi = \Psi_0 \exp\left(-x\sqrt{\frac{e^2}{\varepsilon k_B T}\sum N_{\pm}^{\infty} z_{\pm}^2}\right) \tag{2.28}$$

The Debye length, denoted as κ^{-1}, is characterized as the thickness of the ionic cloud surrounding the central ion within the Debye-Hückel theory. In this theory, the total charge of the ionic cloud has the same magnitude as the central ion charge but with an opposite sign, ensuring electroneutrality. This parameter is defined by Equation 2.29:

$$\kappa^2 = \left(\frac{2e^2 N_A}{\varepsilon k_B T}\right) I \tag{2.29}$$

Where N_A is Avogadro's number, and I is the ionic strength, defined as:

$$I = \frac{1}{2N_A}\sum N_{\pm} z_{\pm}^2 \tag{2.30}$$

Upon substitution of the Debye length into Equation 2.28, Equation 2.31 is derived:

$$\Psi = \Psi_0 \exp(-\kappa x) \tag{2.31}$$

Equation 2.31 indicates the electrical potential decays exponentially. The potential drop, along with the distribution of excess ionic population at the surface [71], is shown in Figure 2.6b. The Gouy-Chapman model also presents certain misconceptions, for example, the assumption that ions are punctual charges. This approximation is invalid for the dimensions of the EDL, particularly due to the solvation shell causing small ions to exhibit larger sizes in the solution.

In further developments, Stern (1924) proposed that the electrified solid-liquid interface comprises both the rigid Helmholtz layer and the diffuse layer of Gouy and Chapman [69]. In adopting this perspective, it becomes evident that the Stern model combines the Helmholtz and Gouy-Chapman models, positing that the Helmholtz layer (HL) alone is insufficient to counterbalance Ψ. Consequently, at the HL's termination (x_h), a residual potential (Ψ_h) becomes apparent. Hence, the potential of the diffuse layer is now expressed as:

$$\Psi = \Psi_h \exp\left[-\kappa\left(x - x_h\right)\right] \tag{2.32}$$

The Stern model provides a satisfactory description of the EDL. However, it falls short of offering a molecular-level depiction of the electrode interface, particularly within HL.

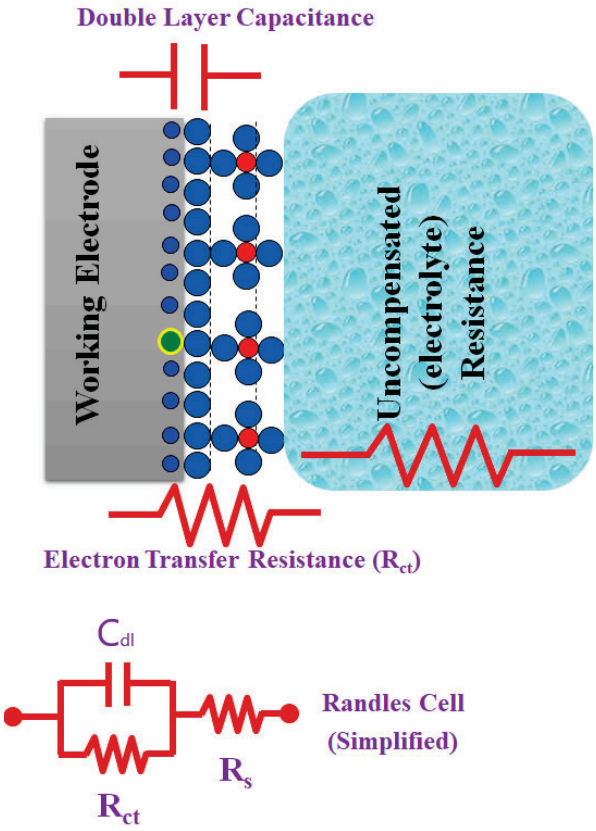

Figure 2.7: A simple scheme to describe the EIS circuit and the redox reaction that takes place at the surface of working electrodes in a conventional electrochemical cell (i.e., three-electrode system). R_{ct} is the charge transfer resistance, R_s is the electrolyte resistance, and C_{dl} is the capacitance of double layer. Reproduced from reference [73].

Subsequently, Grahame modified the Stern model to address this limitation by characterizing the HL as two distinct layers in 1947, with the first being more rigid than the second, as illustrated in Figure 2.6c. The first layer comprises solvent (water) molecules oriented in alignment with the electrode charge. These molecules may also participate in ion solvation, a feature that is already inherent in the composition of the second layer. Conventionally, the first layer is referred to as the inner Helmholtz plane (IHP), while the second is known as the outer Helmholtz plane (OHP) [71].

2.3.2 Electrochemical impedance spectroscopy

In a conventional electrochemical cell, interactions between matter (redox species) and electrodes include the concentration of electroactive species, charge transfer, and mass transfer from the bulk solution to the electrode surface, along with the resistance of the electrolyte. Each of these phenomena is represented by an electrical circuit consisting of resistances,

capacitors, or constant phase elements that are connected in parallel or in series, forming an equivalent circuit, as depicted in Figure 2.7 [73]. Consequently, electrochemical impedance spectroscopy (EIS) can be used to investigate mass transfer, charge transfer, and diffusion processes. The name impedance "spectroscopy" is derived from the fact that the impedance is generally determined at different frequencies rather than just one. Thus, EIS has the capability to explore intrinsic material properties or specific processes that may influence the conductance, resistance, or capacitance of an electrochemical system [74].

It is worth noting that impedance differs from resistance, as resistance in direct current (DC) circuits adheres directly to Ohm's Law. EIS is based on the perturbation of an electrochemical system in equilibrium or in steady state, via the application of a sinusoidal signal (alternating current (AC) voltage or AC current) over a wide range of frequencies and the monitoring of the sinusoidal response (current or voltage, respectively) of the system toward the applied perturbation [75]. The electrochemical cell response exhibits a pseudo-linear behavior, where a phase shift is acquired while the current response to a sinusoidal potential forms a sinusoid at the applied frequency. Thus, the excitation signal is presented as a function of time, as illustrated in Equation 2.33:

$$E_t = E_0 \cdot \sin(\omega t) \tag{2.33}$$

Where E_t is the potential at time t, E_0 is the amplitude of the signal, and ω is the radial frequency.

The relationship between the radial frequency (ω) and the applied frequency (f) is calculated by Equation 2.34:

$$\omega = 2 \cdot \pi \cdot f \tag{2.34}$$

In a linear system, the signal is shifted in phase (ϕ) and has a distinct amplitude compared to I_0, as expressed in Equation 2.35:

$$I_t = I_0 \sin(\omega t + \phi) \tag{2.35}$$

Taking into account the electrical parameters of E and I as a function of angular frequency in the time domain, as well as the shifted-phase angle. Thus, the impedance of the entire system can be determined using Equation 2.36 [76]:

$$Z = \frac{E}{I} = Z_0 \exp(i\phi) = Z_0(\cos\phi + i \sin\phi) \tag{2.36}$$

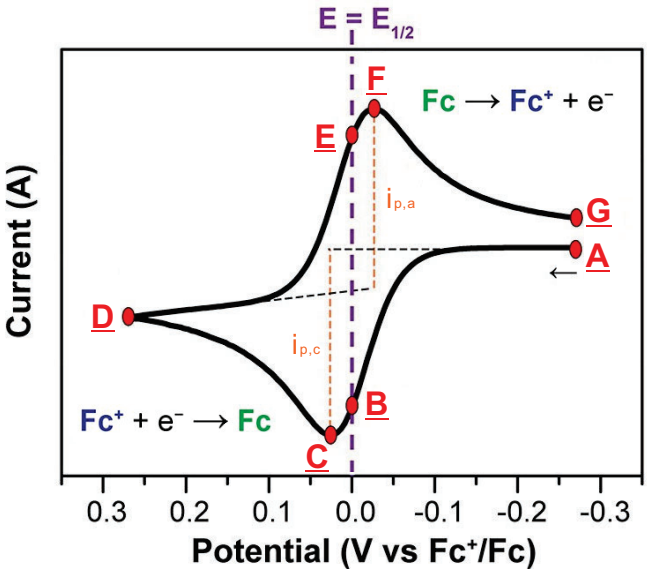

Figure 2.8: Cyclic Voltammogram of the reversible reduction of a 1 mM Fc^+ solution to Fc, at a scan rate of 100 mV/s. Reproduced from reference [78] according to the International Union of Pure and Applied Chemistry (IUPAC) convention.

Where Z, E, I, ω, and ϕ are impedance, potential, current, frequency, and phase shift between E and I, respectively. The impedance is characterized by both a magnitude, Z_0, and a phase shift, ϕ [73]. Once the experimental data are collected, a series of potential-time and current-time are obtained, which correspond to the impedance at each frequency studied. The representation of the EIS data is by means of impedance spectra known as Nyquist plots ($-Z_{imag}$ VS. Z_{real}) that represent the real impedance plotted against its imaginary part and also is often used the Bode plots ($\log|Z|$ vs $\log freq$, ϕ vs $\log freq$) that is the graphical representation of the modulus of the impedance and its phase-angle, as a function of the frequency domain [76, 77].

2.3.3 Voltammetric techniques

Cyclic voltammetry

According to Nerst or Butler-Volmer equations, at the electrode surface, the redox species concentrations are controlled by the potential applied and the rate of reaction (k) respectively. The Nernst equation establishes a relationship between the potential of an electrochemical cell (E), the standard potential of a species (E^0), and the relative activities of the oxidized (Ox) and reduced (Red) analyte in the system at equilibrium. This equilibrium is described by the Nernst equation (Equation 2.37):

$$E = E^0 + \frac{RT}{nF} \ln \frac{(\mathrm{Ox})}{(\mathrm{Red})} = E^0 + 2.3026 \frac{RT}{nF} \log_{10} \frac{(\mathrm{Ox})}{(\mathrm{Red})} \tag{2.37}$$

In this equation, F represents Faraday's constant, R is the universal gas constant, n is the number of electrons, and T is the temperature. As the applied potential changes, the ratio Ox/Red also changes. For a more negative potential the ratio becomes smaller (Ox is reduced) and for a more positive potential the ratio becomes larger (Red is oxidized). The Butler-Volmer equation links potential, concentration, and current and is given by:

$$\frac{i}{nFA} = k \left\{ Ox \exp[-\alpha\theta] - Red \exp[(1-\alpha)\theta] \right\} \tag{2.38}$$

Where $\theta = nF\frac{(E-E^\circ)}{RT}$, k = heterogeneous rate constant, α = transfer coefficient and A = area of the electrode. The flow of current is directly dependent on the flux of material and the electrode surface [79].

Cyclic voltammetry (CV) stands as an important and widely employed electrochemical technique, commonly utilized for investigating the reduction and oxidation processes of molecular species. Moreover, CV proves invaluable in the examination of electron transfer-initiated chemical reactions. As shown in Figure 2.8, during the forward scan, the potential undergoes a negative sweep from the starting potential A to the switching potential D, forming the cathodic trace. The scan direction is then reversed, and the potential is positively swept back to G, constituting the anodic trace [77, 78].

The presence of peaks in a cyclic voltammogram can be understood by take an example of the equilibrium between ferrocenium (Fc^+) and ferrocene (Fc), a reversible redox couple dissolved in the electrolyte. In the application of the Nernst Equation to the one-electron reduction of Fc^+ to Fc, the activities are replaced with their concentrations, which are more experimentally accessible. Additionally, the standard potential E^0 is replaced with the formal potential $E^{0\prime}$, and n is set equal to 1:

$$E = E^{0\prime} + \frac{RT}{F} \ln \frac{[\mathrm{Fc}^+]}{[\mathrm{Fc}]} = E^{0\prime} + 2.3026 \frac{RT}{F} \log_{10} \frac{[\mathrm{Fc}^+]}{[\mathrm{Fc}]} \tag{2.39}$$

As the potential undergoes a negative (cathodic) scan from point A to point D (Figure 2.8), the concentration of $[Fc^+]$ gradually depleted near the electrode as it is being reduced to Fc. At point C, where the peak cathodic current ($i_{p,c}$) is observed, the current is determined by the delivery of additional $[Fc^+]$ through diffusion from the bulk solution. The volume of the solution at the electrode surface containing the reduced Fc, known as the diffusion layer, continues to expand during the scan. This expansion decelerates the mass transport of $[Fc^+]$ towards the

electrode. Consequently, upon progressing to more negative potentials, the rate of diffusion of [Fc^+] from the bulk solution to the electrode surface becomes slower, resulting in a decline in the current as the scan advances from point C to point D.

Upon reaching the switching potential (D), the scan direction is reversed, and the potential is scanned in the positive (anodic) direction. While the concentration of [Fc^+] at the electrode surface was depleted during the cathodic scan, the concentration of Fc at the electrode surface increases. The Fc present at the electrode surface undergoes oxidation back to [Fc^+] as the applied potential becomes more positive. At points B and E, the concentrations of [Fc^+] and Fc at the electrode surface become equal, $E = E_{1/2}$. This corresponds to the halfway potential between the two observed peaks (C and F) and offers a straightforward method to estimate the formal potential ($E^{0\prime}$) for a reversible electron transfer, as mentioned earlier. The separation of the two peaks arises from the diffusion of the analyte to and from the electrode [78, 80].

Criteria measurable by CV can be decide if an electrode reaction is reversible. The voltammogram is characteristic, with rather unsymmetrical shapes but equal heights of anodic and cathodic peaks because of both oxidized and reduced species need to exist with equal concentration in the solution. The number of electrons transferred (n) during the electrode reaction for a reversible couple can be determined from the separation between the anodic and cathodic peak potentials by $59/n$ mV at 25 °C [81, 82]. For a reversible reaction, the concentration is related to peak current by the Randles-Sevcik expression (at 25 °C):

$$i_p = 2.686 \times 10^5 n^{3/2} A D^{1/2} v^{1/2} C \tag{2.40}$$

Where i_p is the peak current, n is the number of electrons transferred in the redox event, A is the macroelectrode area, D is the redox diffusion coefficient, v is the scan rate, and C is the bulk redox concentration [83, 84].

Alternating current voltammetry

Alternating current voltammetry (ACV) closely resembles cyclic voltammetry, operating as a potential sweep method within the frequency domain. It involves superimposing a small-amplitude AC voltage onto a linear ramp. The process involves specifying starting and ending potentials that index the E_0 of the redox species. Additionally, a sinusoidally oscillating AC wave is combined with the potential waveform (Figure 2.9). The frequency of the AC can be adjusted, with the magnitude of the AC oscillations being small compared to the overall voltage change. The resultant alternating current is recorded, and the electrochemical response presents as a single peak [86].

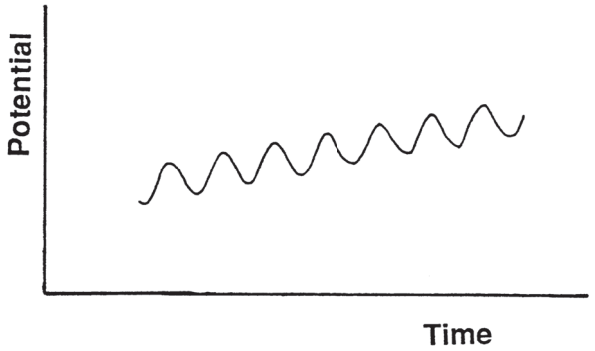

Figure 2.9: Potential-time waveform used in alternating current voltammetry. Adapted from reference [85].

The pulse is repeatedly applied to the system, causing the potential to return to its initial value each time. This measurement method includes the advantages of alternating current (sensitivity) and pulse methods (returning to the initial value of the voltages after the measurement cycle) and is less affected by the adsorption of analytes or the products of electrochemical reactions [87].

Typically, the alternating potential has a frequency ranging from 50-100 Hz and an amplitude of 10-20 mV. The AC signal induces a perturbation in the surface concentration, around the concentration maintained by the DC potential ramp. The resulting AC current is plotted against the potential. Such a voltammogram exhibits a peak, with its potential aligning with the polarographic half-wave potential, particularly for a reversible system. This response essentially represents the derivative of the DC polarographic response for a reversible system. The height of the AC voltammetric peak is proportional to the analyte's concentration (C) and, in the case of a reversible reaction, to the square root of the frequency (ω):

$$i_p = \frac{n^2 F^2 A \omega^{1/2} D^{1/2} \Delta E}{4RT} C \tag{2.41}$$

Where A is the electrode area, D is the diffusion coefficient of the electroactive species, and the term ΔE is the amplitude of the AC potential signal [85].

Square wave voltammetry

Square wave voltammetry (SWV) stands as a well-known and versatile voltammetric technique widely utilized for analytical applications, mechanistic studies, and kinetic measurements of electrode processes. It belongs to the family of pulse voltammetric techniques and can be considered a special form of the popular differential pulse voltammetry. Originating from the historical roots of the Kalousek commutator and Barker square wave polarography, the technique gained

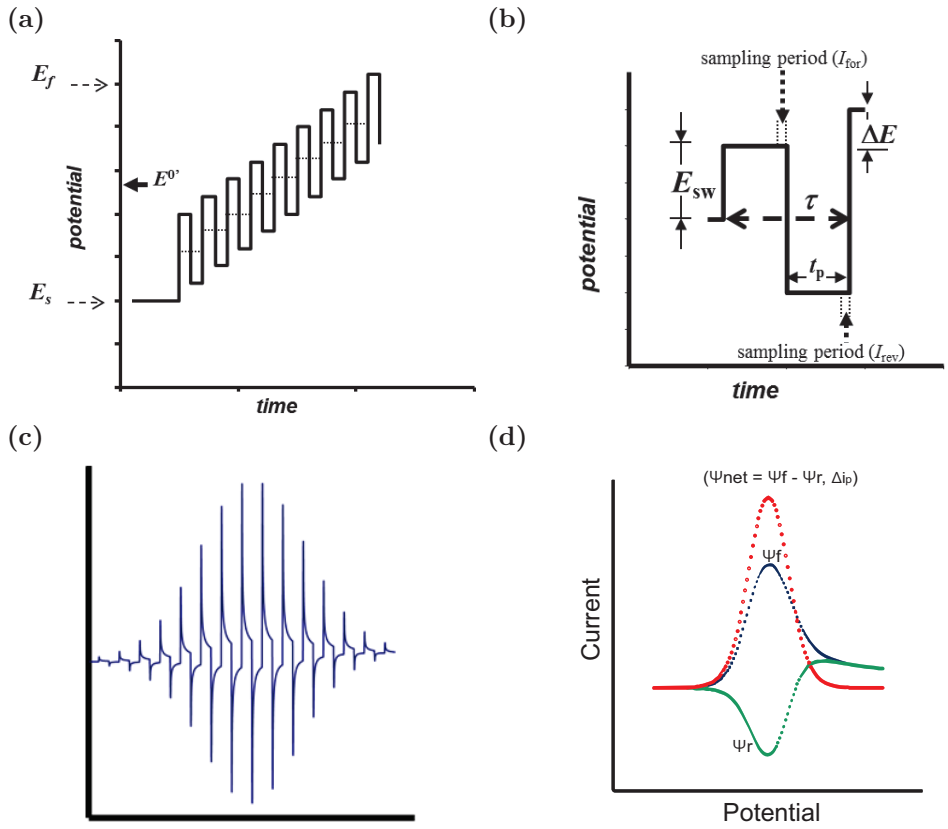

Figure 2.10: Potential modulation (a), single potential cycle (b), and variation of the current in the course of the SWV (c); A typical SWV consisting of a forward (anodic, Ψ_f), reverse (cathodic, Ψ_r), and net (Ψ_{net}) component with net peak current Δi_p (d). Reproduced from reference [88].

popularity significantly following the work of Osteryoungs, the remarkable theoretical contributions of Lovrić, and the collaborative efforts of others [88].

Basic features of potential modulation, illustrated with the simulated response during experiments, are depicted in Figure 2.10. In contemporary SWV, potential modulation comprises a staircase potential combined with square-shaped potential pulses (Figure 2.10a), first introduced by Ramaley and Krause. The key parameters of the potential cycle, composed of two neighboring pulses (Figure 2.10b), include the height of the pulses (referred to as square wave (SW) amplitude, E_{sw}) and the duration of the single potential cycle τ expressed in terms of SW frequency (f), defined as $f = 1/\tau$. The frequency can also be defined in terms of the duration of a potential pulse t_p ($\tau = 2t_p$), as $f = 1/(2t_p)$, representing the number of potential cycles in a unit of time. The typical frequency range provided by commercially available instrumentation is from 5 to 2000 Hz, which corresponds to the duration of a single potential pulse from 0.25 to 100 ms. The scan rate (v) of the overall experiment is defined as $v = f\Delta E$, where ΔE (Figure 2.10b) is the step of the staircase potential [88, 89].

Relative to the direction of the staircase modulation, forward and reverse (backward) potential

pulses can be distinguished. In the course of each potential cycle the electrode reaction is driven in both anodic and cathodic directions by the two opposite pulses, thus providing an insight into the electrode mechanism. In the course of the experiment, the current varies with time as theoretically predicted in Figure 2.10c. However, it is not the real outcome of the experiment as the current sampling is done at the end of each potential pulse only, aiming to discriminate against the charging current. In the SWV, both forward (I_f) and reverse (I_r) components correspond to the currents associated with the forward and reverse potential pulses, respectively. The SWV response is notable for plotting both forward and reverse components versus the potential of the staircase modulation, i.e., the mid-potential of the two adjoining pulses. This results in assigning two current values to each potential value of the staircase modulation. The net SW component is calculated by subtracting the reverse from the forward currents, the subtraction procedure of the forward and reverse currents contributes further to canceling out the remaining charging current, which is one of the reasons for the high quality and enhanced sensitivity of experimentally collected net SW, often forming a bell-shaped curve that facilitates precise determination of the position (Ψ_{net} - net peak potential) and the height (Δi_p) (Figure 2.10d) [88–90].

The net peak current depends linearly on the square root of the frequency which can be expressed as following Equation 2.42 [69]:

$$\Delta i_p = nFAD^{1/2}\Delta\Psi_p f^{1/2}C \tag{2.42}$$

Where Δi_p is the differential current peak value, A is the surface area of the electrode, C is the concentration of the species, D is the diffusivity of the species, and $\Delta\Psi_p$ is a dimensionless parameter which gauges the peak height in SWV relative to the limiting response in normal pulse voltammetry. The dimensionless peak current depends on the sampling procedure. The relationship between Δi_p and the square root of the frequency depends on the fraction of the pulse at which the current is sampled. This relationship is linear if the relative size of the sampling window is constant. If the absolute size of the sampling window is constant, its relative size increases and the pulse fraction decreases as the frequency is increased [69].

2.4 Concept of aptamer

2.4.1 Process of SELEX

In 1990, Ellington and Szostak introduced the term “aptamer”, which is Latin for “to fit”, and “meros” which is Greek for “part” or “region” [92, 93]. Aptamers, oligonucleotides (or

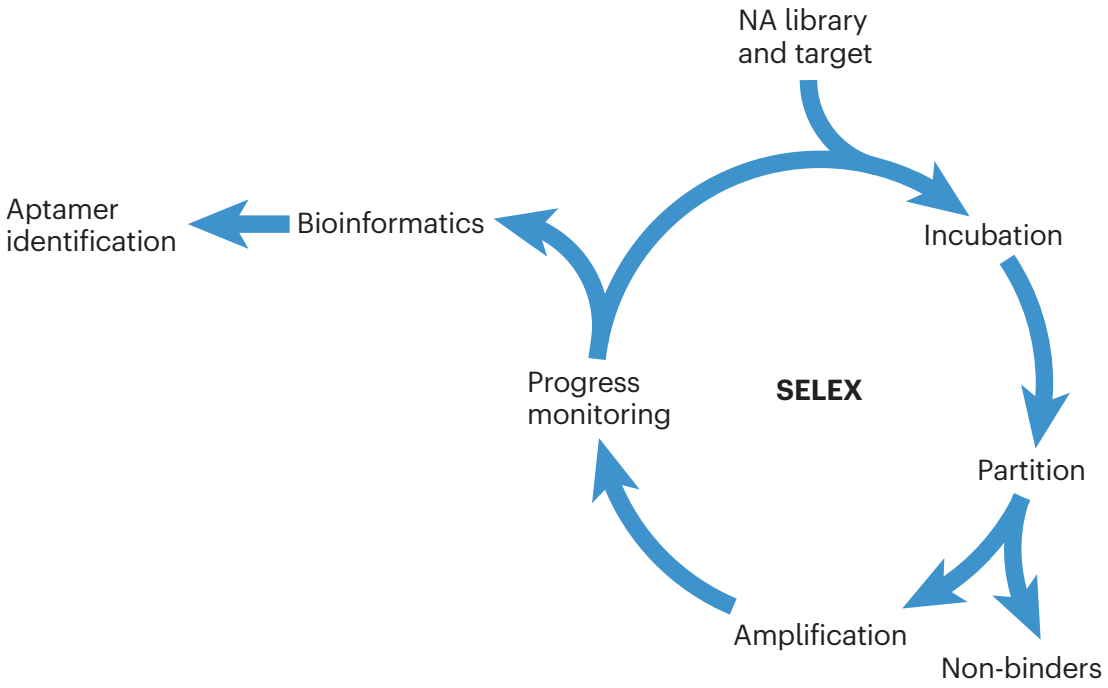

Figure 2.11: General outline of the SELEX process and aptamer identification [91].

oligopeptides) typically ranging from 20 to 80 nucleotides in length, are selected in vitro or in vivo from large randomized libraries to exhibit high affinity and specificity towards target molecules. The nature of the interaction between aptamers and their targets depends on the characteristics of the target molecule, with small molecules being integrated into aptamer structures through stacking interactions, electrostatic complementarity, and/or the formation of hydrogen bonds [2, 92]. The typical method for the isolation of aptamers was first described by Tuerk and Gold, as is konwn as the systematic evolution of ligands by exponential enrichment (SELEX, Figure 2.11) [94]. SELEX is based on the concept that among a vast array of three-dimensional nanostructures, there exists an oligonucleotide with a unique affinity for almost any target molecule, which can be isolated. The interaction strength between an aptamer and its target is commonly quantified using the equilibrium dissociation constant (K_D), with lower K_D values indicating stronger binding affinity:

$$K_D = \frac{[A][T]}{[AT]} \tag{2.43}$$

Where A is the aptamer, T is the target, and AT is the aptamer-target complex. K_D can also be described using the ratio of the on-rate and off-rate, where k_{off} is the rate of disassociation and k_{on} is the rate of association:

$$K_D = \frac{k_{off}}{k_{on}} \tag{2.44}$$

Determination of the dissociation constant by either method reveals the optimal working conditions of an aptamer for detecting its cognate target [91].

The initial single-stranded DNA (ssDNA) library typically comprises up to 10^{14-16} different sequences, each featuring a random region flanked by two constant sequence regions. These constant regions serve as primer-binding sites, which are necessary for the amplification step [95]. The DNA-based SELEX protocol generally encompasses four sequential steps: incubation, partition, amplification, and progress monitoring of ssDNA. During the incubation phase, 0.5-2 nmol of the initial ssDNA library incubates with the target under specific conditions simulating the target's natural environment. Subsequently, a partitioning strategy is applied to segregate aptamers bound to the target from non-binding molecules. Once recovered, the aptamers undergo amplification through polymerase chain reaction (PCR) to regenerate the ssDNA library with reduced variability, facilitating subsequent selection rounds. The evolved libraries are monitored for enrichment and sequenced to identify hit aptamer candidates [2, 91].

2.4.2 Aptamer-based sensors (aptasensors)

Biosensors offer a rapid analytical approach, economical operation, and real-time detection capabilities. A biosensor's functionality is rooted in the specific binding of a biomolecule to the analyte of interest, and the subsequent translation of this binding event into detectable and measurable signals [92, 96]. The receptor, a key element in biosensor design, consists of biomolecules such as antibodies, enzymes, cells, and aptamers. Among them, aptamers exhibit remarkable specificity and physicochemical stability in contrast to their counterparts. Their notable features include resistance to denaturation, cost-effectiveness, minimal batch variation, ease of modification for covalent bonding to material surfaces, and prolonged storage life [96, 97].

Due to these advantages, aptamers have got noteworthy advancements in aptamer-based sensors commonly referred to as aptasensors. Various designed strategies can be employed in the construction of aptasensors, including configurational change (where analyte binding induces assembly or dissociation of the sensor construct), conformational change (where analyte binding alters the conformation of the surface-immobilized aptamer strands) and conductivity change (where analyte binding "switches on" the conductivity of the surface-bound aptamer-DNA constructs). These changes can be translated into signal outputs that reflect the biomolecular

interaction between the aptamer and the target. Signal output modes used to monitor aptamer-target interactions in electrical and optical terms include fluorescence, electrochemical, surface plasmon resonance and colorimetric-based measurements [96, 98, 99]. This diversification in signal transduction modes further enhances the versatility and applicability of aptasensors in various analytical contexts.

2.5 Finite-difference time-domain simulation

The finite-difference time-domain (FDTD) method is one of the most accurate and straightforward approaches for rigorously modeling nanophotonic devices, processes, and materials. Despite its computational intensity, the FDTD method effectively handles arbitrarily shaped structures using an explicit numerical solution to Maxwell's curl equations. This method is instrumental in evaluating the electric and magnetic field components through the utilization of a discrete mesh composed of Yee cells [100, 101].

The FDTD method has several strength. It evolves in time, just as nature evolves over time. As a result, FDTD results can give a direct insight into the time evolution of electromagnetic fields. The models are matrix-free and may be efficiently parallelized onto supercomputers in a straightforward manner. Additionally, the FDTD method treats impulsive and nonlinear behaviour naturally, although sources of error are well understood and may be bounded to certain tolerance levels. Finally, FDTD models do not automatically need to be reformulated for different problems. Instead, changes are typically only made to account for additional physics as needed [102].

2.5.1 Theory of FDTD

The FDTD method was first introduced by Kane Yee in 1966 [103] and was furthered by Taflove, Yee developed the mathematical approach to spatially discretize the computational space into what is now known as a Yee cell, Figure 2.12. The Yee cell is the unit cell of the equally offset electric and magnetic field computation points. The FDTD method, described thoroughly in Taflove's book "Computational electrodynamics: the finite-difference time-domain method" [104], was first developed to model electromagnetic radio waves. However, due to the simple and versatile approach, it is able to naturally handle any electromagnetic modeling situation given sufficient computing resources [101].

Each field component is computed on a discrete spatial and temporal grid cell (Yee cell), where an electric component is located on the edges of the box and the magnetic component is located on the faces. Moreover, FDTD is a time domain technique, by setting a Δt time step for time

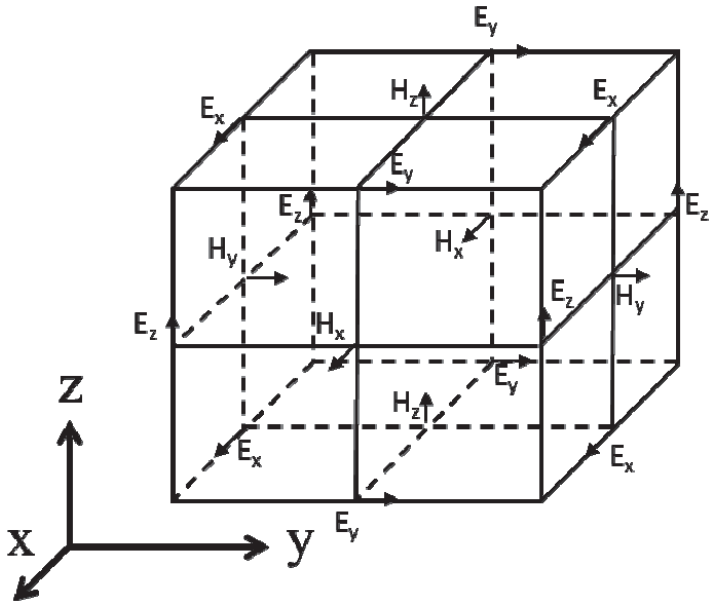

Figure 2.12: Yee cell. Arrows indicate the direction of the E or H field that is calculated at each point [101].

discretization, the H-fields and E-fields can be calculated after a first-order approximation is made. For example, at first, the electric field vector components are solved at a given time in the schematized Yee cell. In the next time step, the magnetic field vector components are solved for the same cell. This process is continued for many iterations until convergence is obtained [105]. The results collected from the FDTD solver are automatically interpolated to the origin of each grid point. Additionally, for insights into the field behavior as a function of different wavelengths $E(\lambda)$, or equivalently frequency $E(\lambda)$.

FDTD method is used to solve Maxwell's differential equations in nonmagnetic materials:

$$\nabla \times E = -\frac{\partial B}{\partial t} \tag{2.45}$$

$$\nabla \times H = J + \frac{\partial D}{\partial t} \tag{2.46}$$

Where E, B, H, J, D are the electric field, magnetic induction intensity, magnetic field, current density, and electric displacement, respectively. For isotropic media, the relationship between these physical quantities is:

$$D = \varepsilon E, B = \mu H, J = \sigma E \tag{2.47}$$

Where ε, μ and σ are the medium dielectric constant, magnetic permeability coefficient and electrical conductivity, respectively.

In three-dimensional space, Maxwell's equations describe six EM field components. Assuming the structure is infinite in the z dimension and that the fields are independent of z, Maxwell's equations can be split into two independent groups of equations that can be solved in the $x-y$ plane only, which results in the transverse electric (TE) and transverse magnetic (TM) modes. Then, we can use the components of E_x, E_y, and H_z to solve TE equations and those of H_x, H_y, and E_z to solve TM equations.

$$\frac{\partial E_z}{\partial y} - \frac{\partial E_y}{\partial z} = -\mu_0 \frac{\partial H_x}{\partial t} \tag{2.48}$$

$$\frac{\partial E_x}{\partial z} - \frac{\partial E_z}{\partial x} = -\mu_0 \frac{\partial H_y}{\partial t} \tag{2.49}$$

$$\frac{\partial E_y}{\partial x} - \frac{\partial E_x}{\partial y} = -\mu_0 \frac{\partial H_z}{\partial t} \tag{2.50}$$

$$\frac{\partial H_z}{\partial y} - \frac{\partial H_y}{\partial z} = \varepsilon \frac{\partial E_x}{\partial t} + \sigma E_x \tag{2.51}$$

$$\frac{\partial H_x}{\partial z} - \frac{\partial H_z}{\partial x} = \varepsilon \frac{\partial E_y}{\partial t} + \sigma E_y \tag{2.52}$$

$$\frac{\partial H_y}{\partial x} - \frac{\partial H_x}{\partial y} = \varepsilon \frac{\partial E_z}{\partial t} + \sigma E_z \tag{2.53}$$

The set of six coupled partial differential equations constitutes the foundational framework of the FDTD numerical algorithm, employed for simulating the interactions of electromagnetic waves with arbitrary three-dimensional objects [106]. In the context of this mathematical formulation, the variable $f(x, y, z, t)$ signifies the electric or magnetic field within the coordinate system and we have the form $f(x, y, z, t) = f(i\Delta x, j\Delta y, k\Delta z, n\Delta t) = f^n(i, j, k)$. It can be discretized through the central difference approximation in both space and time:

$$\left.\frac{\partial f(x, y, z, t)}{\partial x}\right|_{x=i\Delta x} \approx \frac{f^n(i+0.5, j, k) - f^n(i-0.5, j, k)}{\Delta x} \tag{2.54}$$

$$\left.\frac{\partial f(x,y,z,t)}{\partial y}\right|_{y=j\Delta y} \approx \frac{f^n(i,j+0.5,k) - f^n(i,j-0.5,k)}{\Delta y} \tag{2.55}$$

$$\left.\frac{\partial f(x,y,z,t)}{\partial z}\right|_{z=k\Delta z} \approx \frac{f^n(i,j,k+0.5) - f^n(i,j,k-0.5)}{\Delta z} \tag{2.56}$$

$$\left.\frac{\partial f(x,y,z,t)}{\partial t}\right|_{t=n\Delta t} \approx \frac{f^{n+0.5}(i,j,k) - f^{n-0.5}(i,j,k)}{\Delta t} \tag{2.57}$$

This sampling approach for the electromagnetic field components within the Yee cell is advantageous for the differential computation of Maxwell's equations and aligns with Faraday's law of electromagnetic induction [107, 108].

2.5.2 Lumerical FDTD

There are various software packages available for implementing FDTD algorithms due to its simplicity, user-friendly interface, and versatility in addressing various problem types [107], including both open-source and commercial tools [100]. One notable software program frequently used for FDTD simulations of photonic structures is Lumerical FDTD. This program offers a user-friendly graphical interface with built-in objects (e.g., cylinders, spheres, pyramids, diffraction gratings) and essential features such as light sources, monitors, boundary conditions, and analysis tools. Lumerical also provides scripting interfaces, both global and local, allowing users to streamline processes and customize simulations. The script language is well-documented, straightforward to learn, and can be used independently or in conjunction with the graphical interface.

Simulations can be executed on various platforms, ranging from a local computer with one or more cores to more powerful remote computers, local networks, or distributed computing platforms like computer clusters or cloud environments. Notably, Lumerical FDTD simulations often do not demand high-performance computing, and a standard laptop or desktop can often suffice for completing simulations within a few hours [109].

2.6 Combined plasmonic and electrochemical techniques

The scientific community has reported numerous applications of plasmonic or electrochemical assays in the field of biosensing over the years. However, the combination of these two methods within the same sensing spot for analytical purposes has received relatively limited exploration and discourse so far. The considerable potential inherent in the combination

of SPR with electrochemistry underscore this combination technique as an analytical tool with the capability to screen both chemically and biologically relevant (bio)molecules. This integration can take advantage of the distinctive features of SPR, seamlessly integrated with an electrochemical readout [110].

2.6.1 The concept of surface plasmon resonance and electrochemical technique

Surface plasmon resonance (SPR) utilizes SPP to directly assess alterations in the local refractive index induced by biomolecular interactions taking place on a noble metal surface. Surface plasmons are optically excited at the interface between a dielectric and a metal by aligning the wavevector of incoming light with that of the surface plasmon, typically accomplished by controlling the angle of the incident light beam. A modification in the wavevector of the plasmon, induced, for instance, by the binding of an antigen to a surface-immobilized antibody, results in a resonance angle shift, offering a label-free and quantifiable measurement of the mass adsorbed on the surface.

A recent trend in (bio)chemical sensors is to combine SPR with electrochemical technique (SPR-EC) due to both techniques exploit reactions occurring on a metal surface, often Au due to its inertness, in both types of system [111]. In such systems, a three-electrode assembly is integrated into SPR to examine the interaction between electrical energy and chemical change. In the three-electrode electrochemical cell, a potential difference is applied between the working electrode (gold film where the surface plasmon is excited) and the counter electrode, while the current flowing through the circuit due to an electrochemical reaction is measured. The potential needed to drive the working electrode is supplied relative to the reference electrode, which presents a known and stable potential relative to the solution [112].

2.6.2 The potential of plasmon-enhanced fluorescence and electrochemical technique

The fluorescent-electrochemical (FL-EC) dual-responsive assay provide sensitive electrochemical signal and stable fluorescence response simultaneously and widely developed [114]. However, thus far, the plasmon-enhanced fluorescence (PEF, see section 2.2) and electrochemical combination method (PEF-EC) is rarely reported.

In the context of Kretschmann configuration SPR (Figure 2.13, left), when the dielectric film is extremely thin or the concentration of the substance to be measured is very low, the absorption of the resonance wave becomes markedly small, resulting in minimal changes in the SPR curve. Consequently, to enhance the sensitivity of SPR sensing technology, the

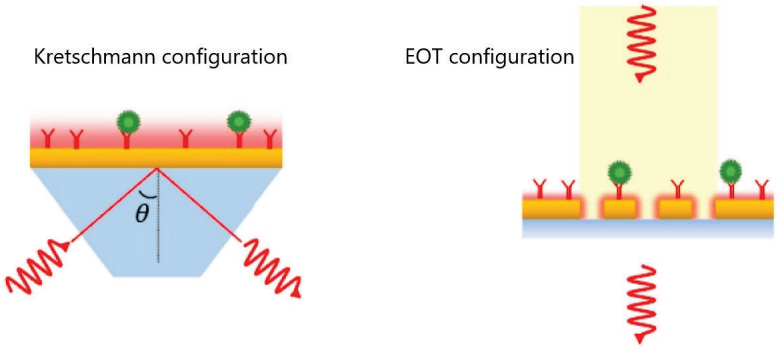

Figure 2.13: Schematic illustration of SPR configuration of Kretschmann (left) and extraordinary optical transmission (EOT, right). Reproduced from reference [113].

surface-sensitive SPR phenomenon is integrated with fluorescence spectroscopy. Knoll and collaborators conducted pioneering work in 2000-2003 [115–117], demonstrating that the improved surface sensitivity of surface PEF spectroscopy complements SPR technology, which allows for the simultaneous collection of additional chemical and physical information at the interface of films [118].

However, the utilization of bulky prism setups in such configurations is not ideal for combination of PEF-EC. Besides the prism-based configuration, another emerging method is utilizing the extraordinary optical transmission (EOT) configuration (Figure 2.13, right) through a subwavelength aperture in a metallic film which has been patterned with a periodic structure. As a result, the prism-free EOT configuration represent one of the most promising techniques for developing portable, high-throughput devices based on plasmonics. These devices are often preferred over traditional Kretschmann SPR for their simplicity and ease of miniaturization, as they typically do not require components like a prism or polarizer [119, 120]. Importantly, the integration of highly confined electric fields to amplify fluorescence through a gating coupling configuration presents a promising research direction.

3 Materials and methods

3.1 Reagents and chemicals

Tris(2-carboxyethyl)phosphine hydrochloride (TCEP), 6-mercapto-1-hexanol (6-MCH), monofunctional methoxy polyethylene glycol thiol (PEG, 2 kDa), tris(hydroxymethyl)aminomethane hydrochloride (Tris), glycerin, sodium chloride, potassium chloride, hydrochloric acid, sulfuric acid, sodium hydroxide, potassium ferricyanide (($K_3[Fe(CN)_6]$)), potassium ferrocyanide (($K_4[Fe(CN)_6]$)), acetone, isopropanol, ethanol, and human serum albumin (HSA) were purchased from Merck/Sigma-Aldrich Chemie GmbH (Darmstadt, Germany). The Recombinant SARS-CoV-2 Spike protein (S1+S2 ECD, His Tag, S protein), the Hemagglutinin/HA1 protein of the Influenza A H1N1 (A/Mexico/InDRE4114/2009), the glycoprotein G/RSV-G protein of the respiratory syncytial virus (RSV, A, rsb1734), and the Spike protein (S1+S2 ECD, as 1-1297) of the middle eastern respiratory syndrome coronavirus (MERS-CoV) were procured from Sino Biological (Sino Biological Inc., Beijing, China). Polystyrene particles were purchased from Bangs Laboratories (Indiana, USA). 10 mM Tris buffer (NaCl 0.15 M, KCl 5 mM, Tris 10 mM, pH 7.4) and high-salt Tris buffer (NaCl 1.0 M, $MgCl_2$ 1 mM, Tris 10 mM, pH 7.4) were prepared. All aqueous solutions were prepared using a Milli-Q ultrapure water system (18.25 MΩ cm, Gradient A10, Merck Millipore, Burlington, MA, USA).

3.2 Preparation of the aptasensor

3.2.1 Aptasensor for HSA

The HSA aptamer (5'-ferrocene (Fc)-GTC TCA GCT ACC TTA CCG TAT GTG GCC CAA AGC GTC TGG ATG GCT ATG AA-$(CH_2)_6$-SH-SH-3') [121] was HPLC-purified and bought from Sangon Biotech (Shanghai, China). Aptamer concentrations were determined using a DS-11 Series Spectrophotometer (DeNovix, USA). A 20 nM aptamer solution [122] was initially activated in a high-salt Tris buffer containing 10 mM TCEP solution (in a molar ratio of 1:1000) for 1 hour to facilitate disulfide bond cleavage. The nanostructured samples were incubated with this solution at room temperature for molecule immobilization on the surface

through Au-S bonds, achieved by circulating the solution over the surface with a peristaltic pump for 16 hours. Subsequently, samples were rinsed with Tris buffer to remove unbound aptamer. The samples were then incubated with 0.5 mM 6-MCH for 1 hour to obtain a compact SAM, blocking unmodified electrode sites and reducing non-specific binding. A final rinse with Tris buffer was conducted to eliminate non-covalently bound blocking molecules. For the HSA assay, the aptasensor was incubated in various concentrations of the analyte for 30 minutes. After incubation, the Au electrodes were rinsed with Tris buffer to remove non-specifically adsorbed HSA molecules.

3.2.2 Aptasensor for SARS-CoV-2 S protein

The following synthesized oligonucleotides were also HPLC-purified and obtained from Sangon Biotech (Shanghai, China).

The first oligonucleotide, a stem-loop single-stranded DNA (5'-dithiol-TAA GT ATC GAG CTT GAC TTA-3', referred to as S1), was specifically engineered for strong covalent attachment to gold surfaces via Au-S bonds. This strand, designed to be partially complementary to the C7 aptamer, served as an anchor for tethering the C7 aptamer to the Au surface through DNA hybridization.

A modified C7 aptamer (5'-methylene blue (MB)-TTT TTT TTT TTT TTT TTT TT CAC GTG GCC CAC GTT AAT CCG TTA TAA GTC AAG CTC GAT-3', S2_20T_MB) was extended by an additional 20 thymine bases and formulated to bind either to S1 or to the SARS-CoV-2 S protein. The original C7 aptamer, chosen for its low dissociation constant (K_D) of 89.41 $\pm$ 18 nM and high selectivity, was previously identified by our colleague, Mateo's work [23].

For comparative purposes, a shorter aptamer (5'-MB-CAC GTG GCC CAC GTT AAT CCG TTA TAA GTC AAG CTC GAT-3', S2_MB), lacking the additional thymine bases, was also utilized to evaluate the performance.

Additionally, dual molecular beacons for individual strands were designed, one for electrochemical detection (5'-dithiol-TAA GT ATC GAG CTT GAC TTA-Fc-3', S1_Fc) and the other for fluorescent signaling (5'-cyanine5.5 (Cy5.5)-TTT TTT TTT TTT TTT TTT TT CAC GTG GCC CAC GTT AAT CCG TTA TAA GTC AAG CTC GAT-3', S2_20T_Cy5.5).

During the assembly of the aptasensor, the AuNpA was first cleaned using oxygen plasma (Diener electronic GmbH, Ebhausen, Germany) at 0.5 mPa for 3 minutes to remove any surface residues. The AuNpA was then immersed in ethanol for 5 minutes to reduce the gold oxides formed and subsequently rinsed with Milli-Q water. The S1 solution was prepared by incubating with 10 mM TCEP for 1 hour to cleave the disulfide bonds of the aptamer

receptors in a high-salt Tris buffer. The nanostructured samples were then incubated with this solution for 16 hours at room temperature to immobilize the molecules on the surface through thiol-gold bonds. Following this, the samples were thoroughly rinsed with Tris buffer to remove any non-bonded aptamer. Next, the prepared samples were incubated with 0.5 mM 6-MCH solution for 0.5 hours to form a compact, self-assembled receptor layer by blocking unmodified sites and suppressing nonspecific binding. The excess 6-MCH molecules were removed by rinsing the AuNpA three times with ethanol and then three times with 10 mM Tris buffer. Finally, S2 strands were incubated on the surface for 2 hours at room temperature to hybridize with the S1 strand. For the S protein assay, the aptasensor was incubated with various concentrations of the analyte molecules for 30 minutes. After incubation, the nanostructured Au samples were rinsed with Tris buffer to remove any excess S protein molecules that were not specifically adsorbed.

Gel electrophoresis experiment: The gel electrophoresis experiment was conducted with the assistance of Mateo Alejandro Martínez-Roque. To evaluate the hybridization efficiency of two ssDNA molecules, S1 and S2_20T_MB, a 4% agarose gel electrophoresis technique was employed. Both molecules have complementary regions. The 4% agarose gel was prepared by dissolving agarose in 1X TBE buffer, heated for complete solubilization, followed by adding 1X RedSafe^{TM} Nucleic Acid Staining Solution (Intron Biotechnology). After setting in a casting tray with inserted well combs, individual and pre-mixed pairs of S1 and S2_20T_MB were incubated for 2 hours at 25 °C, then loaded into wells for electrophoresis. We also introduced an Ultra Low Range DNA Ladder (ThermoFisher Scientific) as a size reference. The gel ran at 125 V for 30 minutes in an electrophoresis chamber filled with 1X TBE buffer.

NUPACK simulation: The hybridization interaction between S1 and S2_20T was simulated using NUPACK (www.nupack.org). The simulation parameters included: (i) nucleic acid type: DNA, (ii) temperature: 25 °C, (iii) oligo concentration: 1000 nM, (iv) number of strand species: S1 and S2_20T, (v) maximum complex size: 2 strands, (vi) dangle treatment: some, (vii) [Na^{+}] concentration: 0.015 M, and (viii) [Mg^{2+}] concentration: 0.001 M.

3.3 Fabrication of Au chips

Au chips were fabricated using various techniques: non-fully penetrating gold nanopit arrays (AuNpA) were fabricated through nanoimprint lithography (NIL), employing a Cr layer as a hard mask; fully-penetrating gold nanohole arrays (AuNhA) were produced using nanosphere lithography (NSL); and non-fully penetrating AuNpA with fringe structures were fabricated through a direct NIL process.

3.3.1 AuNpA fabrication based on NIL using hard mask

The fabrication of the master template involved the formation of nanopit arrays on a master mold. This was initiated by oxidizing a silicon wafer (diameter: 4 inches, n-type, ⟨100⟩ orientation, thickness: 500-550 μm, Silicon Materials, USA) to obtain an top layer of silicon dioxide (SiO_2), which exhibited a dark blue color and had a thickness of approximately 100 nm. A layer of polymethylmethacrylate (PMMA, AR-P 669.04, Allresist GmbH, Germany) was subsequently spin-coated onto the Si/SiO_2 substrate. This coated wafer was then subjected to electron beam with an acceleration voltage of 50 kV, followed by a development process. The subsequent etching of SiO_2 was conducted using a CH_3/SF_6 plasma in a reactive ion etching system (RIE, Oxford PL 100, Oxford Instruments, UK). The removal of the remaining resist was done by employing an O_2 plasma in the RIE chamber by cooling the wafer to a temperature of -140 °C.

The surface of the master mold was subjected to an additional treatment to deposit an anti-adhesive layer through a vapor-phase silanization process. Initially, the mold underwent a cleaning and activation phase using an O_2 plasma treatment (Pico low-pressure plasma, Diener electronic GmbH, Germany) for 3 minutes at a power of 80 W and a pressure of 0.7 mbar to enhance the covalent binding the anti-adhesive layer of FOTCS (trichloro (1H,1H,2H,2H-perfluorooctyl) silane) to the SiO_2 surface via silanol groups [123, 124]. Subsequently, the wafer was transferred to an argon atmosphere glove box (99.99% argon atmosphere

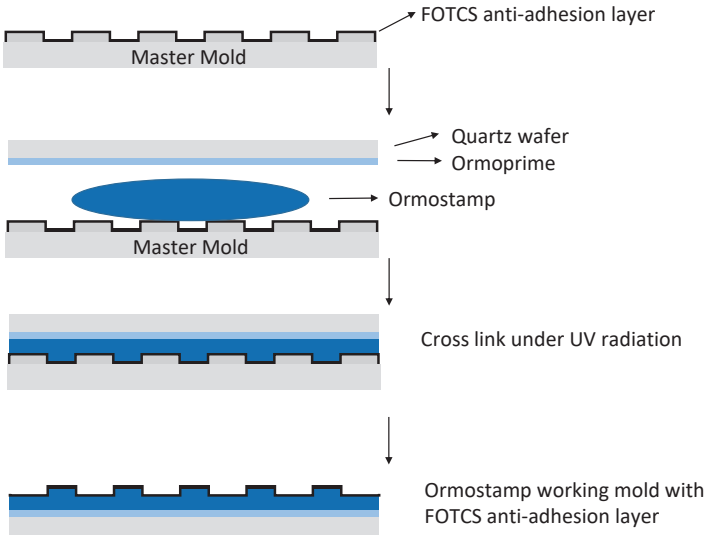

Figure 3.1: Fabrication process of the working mold.

MB200B, MBRAUN, Germany) equipped with a desiccator for the silanization phase. In this phase, 200 μl of FOTCS was vaporized under a pressure of 45 mbar and allowed to deposit on the surface for a duration of 1.5 hours, resulting in the formation of a homogeneous self-assembled monolayer (SAM). Following this surface modification, the wafer was rinsed in a sequential acetone, isopropanol, and water cascade to prepare it for the replication process.

The process for fabricating the NIL working stamp is depicted in Figure 3.1. The initial step involved preparing a 4-inch transparent quartz wafer. This wafer was treated in an oxygen plasma using a Gigabatch system (TePla Gigabatch 360, PVA MPS GmbH, Germany) for a duration of 5 minutes (O_2 flow rate: 600 sccm, power: 600 W) in order to remove any organic contamination from the quartz surface. Following this, an adhesive promoter, OrmoPrime 08 (Micro resist technology GmbH, Germany), was applied to the wafer to enhance the adhesion of the Ormostamp polymer onto the quartz substrate. OrmoPrime was spin-coated at 4000 rpm for 60 seconds, with an acceleration rate of 1000 rpm/s, followed by a hardbake for 5 minutes at 150 °C. According to the datasheet provided in Table 3.1, this process resulted in a film thickness of 130 ± 15 nm.

The subsequent step was to dispense 80 μL of Ormostamp resist (Micro resist technology GmbH, Germany) onto the 4-inch master mold, previously treated with the FOTCS anti-adhesive layer. The quartz wafer was then carefully placed on top of the OrmoStamp droplet (taking care to avoid the formation of small bubbles). Upon contact with the droplet, the OrmoStamp began to spread, filling the gap between the master stamp surface and the wafer backplane. The Ormostamp resist, known for its low viscosity, effectively filled the nanopit structures of the master stamp and helped minimize air bubble defects. The transferred negative replica from the master stamp was solidified through UV flood exposure (MA-6 Mask aligner, 1000 mJ/cm^2 for 2 minutes, Süss Microtech AG, Germany), followed by a final thermal post-bake at 130 °C for 30 minutes. Similarly, the Ormostamp surface was treated with FOTCS anti-sticking agent in a glove box environment.

NIL is widely acknowledged as an advanced and efficient technique for fabricating nanometer-

Table 3.1: Ormoprime datasheet.

OrmoPrime	
Spin coating	
spin speed [rpm]:	4000
time [s]:	60
acceleration [rpm/s]:	1000
hardbake [°C]:	150
time [min]:	5
film thickness [nm]:	130 ± 15

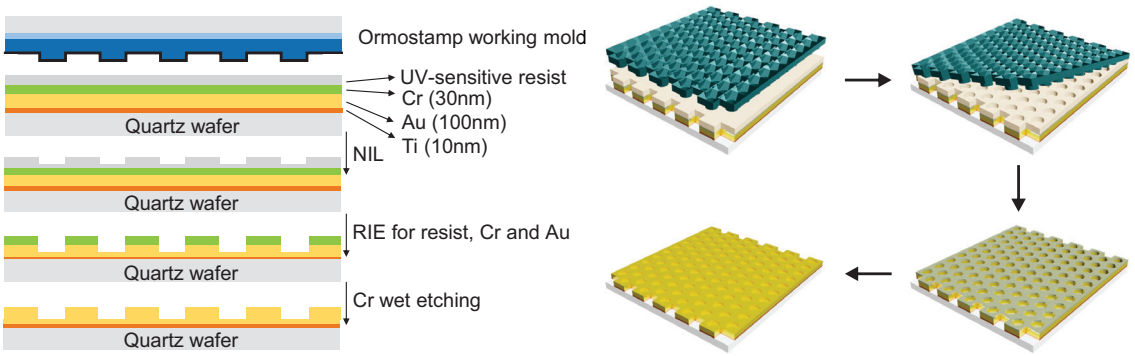

Figure 3.2: Schematic representation of the fabrication of AuNpA based on NIL.

scale features on large wafers. It offers several advantages, including high throughput, cost-effectiveness, compatibility with large areas, and remarkable uniformity [125]. The NIL procedure is illustrated in Figure 3.2. Firstly, a tri-metallic layer consisting of 10 nm Ti, 100 nm Au, and 30 nm Cr (serving as a hard mask layer) was deposited (using Pfeiffer PLS 570, Germany) onto the quartz wafer. The mr-NIL200 (Micro resist technology GmbH, Germany) is a photo-curable NIL resist particularly suitable for hard and non-permeable stamp materials. Prior to coating, all substrates underwent a pre-treatment step involving baking at 110 °C for 3 minutes to remove any organic solvents. Subsequently, the mr-NIL200 resist was spin-coated onto the Quartz/Ti/Au/Cr surface at 3000 rpm for 30 seconds, with an acceleration of 1000 rpm/s, followed by a soft bake at 60 °C for 3 minutes. An Ellipsometer SE800 (Sentech GmbH, Germany) was used to measure the resist thickness to be approximately 200 nm. The nanoimprinting of the Quartz/Ti/Cr/Au/mr-NIL200 wafer was carried out using the NX-2000 system (Nanonex, USA). During this process, the Quartz/Ti/Cr/Au/mrNIL200 wafer and the working stamp wafer were sandwiched between two silicone foils and compressed following the air cushion principle. A preliminary imprint phase of 1 minute at 100 psi was necessary to ensure stability and uniformity. The main imprint phase lasted for 5 minutes at 200 psi, followed by UV irradiation (365 nm wavelength) for 1 minute. All imprinting steps were performed at room temperature. The wafers were then carefully separated using a razor blade. The final patterned Quartz/Ti/Cr/Au/mr-NIL200 wafer was then ready for subsequent etching steps.

Following the UV-NIL procedure, a series of RIE steps were conducted including the initial O_2 plasma etching of the mr-NIL200 residual layer, followed by Cl_2/O_2 etching of the Cr hard mask, and the Cl_2/Ar etching of the Au layer. Considering the etching selectivity of mr-NIL200 over the Cr layer and Cr over the Au layer, specific etching recipes were employed for each distinct layer. Direct etching of the Au layer using only the mr-NIL200 resist resulted in inadequate etching depths. Cr is widely favored as a hard-etching mask material due to its robust resistance against plasma etching. The plasma etching process for Cr is well-established,

Table 3.2: Dry etching parameter.

Cr etch recipe		Au etch recipe	
Cl_2 gas flow	50 sccm	Cl_2 gas flow	15 sccm
O_2 gas flow	3 sccm	Ar gas flow	5 sccm
RF power	150 W	RF power	50 W
ICP power	0 W	ICP power	800 W
Chamber pressure	0.09 Torr	Chamber pressure	0.007 Torr
Temperature	30 °C	Temperature	50 °C
Etching rate for mr-NIL200	176 nm/min	Etching rate for Cr	13 nm/min
Etching rate for Cr	39 nm/min	Etching rate for Au	72 nm/min
Selectivity (mr-NIL200/Cr)	4.51	Selectivity (Cr/Au)	0.18

typically involving Cl-containing gases (such as Cl_2 and CCl_4) and oxygen, the reaction is: $Cr + 2O^* + 2Cl^* \rightarrow CrO_2Cl_2$ (boiling point 117 °C, volatile at room temperature) [126]. The etching characteristics for Au based on Cl_2/Ar-based chemistry occurred by a combination of ion-assisted chemical reaction ($Al + 3Cl^* \rightarrow AuCl_3$) and physical sputtering. Avoiding oxygen added also could lower the etching rate of the Cr, resulting in effective etching selectivity between Au and Cr in principle. Precise temperature control is crucial during this etching step to ensure the volatility of $AuCl_3$ is maintained while preventing its thermal decomposition into non-volatile AuCl [127]. The parameters for these dry etching steps were measured using a Dektak profilometer (DektakXT, Bruker, USA) and are comprehensively summarized in Table 3.2.

Upon completion of the dry etching steps, the residual Cr layer was dissolved using a Cr etchant (TechniEtch Cr01 from MicroChemicals GmbH, Ulm, Germany) resulting in the formation of a finely patterned Au layer with nanopit arrays. Subsequent to the etching, the fabricated AuNpA were treated with a cleaning process involving a sequential rinse in acetone, isopropanol, and water, then treated with an oxygen plasma, followed by further rinsing in ethanol and Milli-Q water, and eventually dried using N_2 gas for further use.

The dry etching process employed in this study was similar to the techniques previously described by Robinson et al. [128]. It is worthy to note that the technical intricacy involved in etching completely through the gold layer down to the quartz substrate to create fully penetrating nanohole structures that requires careful control to avoid over-etching. In contrast, the fabrication of nanopit arrays is relatively straightforward and offers distinct advantages (see the section of section 2.1.1) in terms of plasmonic excitations by eliminating of the Au/substrate mode.

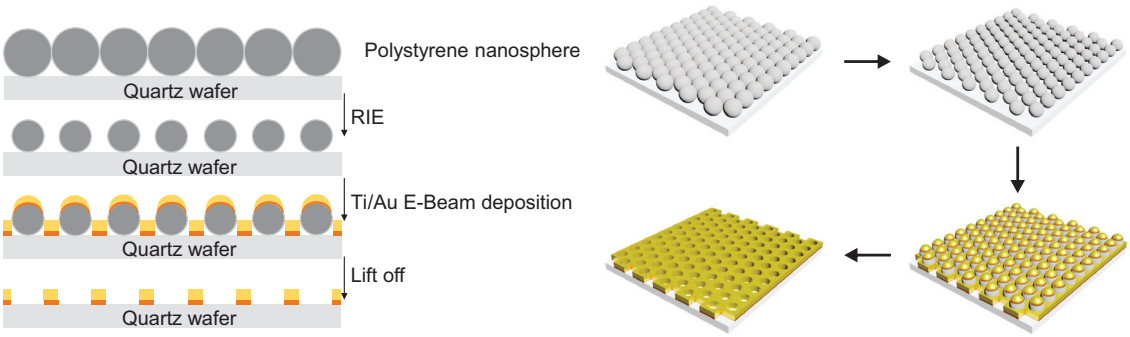

Figure 3.3: Schematic representation of the fabrication of fully penetrating AuNhA based on NSL.

3.3.2 AuNhA fabrication based on NSL

To obtain the AuNhA structure for comparison, NSL was employed, similar to the protocol our group previously established [129–131], by using the PE funnel-assisted interfacial assembly technique on 4-inch quartz wafers (thickness: 100 × 0.525 mm, Wafer Universe, Germany), as depicted in Figure 3.3. Initially, the quartz wafer was subjected to an oxygen plasma treatment at 0.7 mbar with power of 200 W for 5 minutes. This step was essential for hydrophilizing the surface, thereby facilitating the NSL process.

Subsequently, a beaker filled with Milli-Q water equipped with the quartz wafer on a sample stage within a PE funnel. To enhance particle packing, 20 μL of a surfactant (TX-100, 10 mM) was added to the water surface. Next, 0.8 mL of a 2.5% polystyrene nanosphere dispersion (Bangs Laboratories, USA) in a Milli-Q water and absolute ethanol mixture (1:1, v/v) was gently dispensed onto a glass slide, allowing it to spread across the water surface. The sample was then dried through a tube, resulting in a homogeneously packed hexagonal particle film.

RIE (Oxford PL 100, Oxford Instruments, UK) was subsequently applied to reduce the particle sizes, creating a non-close-packed particle array. The etching gas mixture comprised O_2 and CHF_3 in a 40:10 sccm ratio, with the process occurring at 0.026 mbar, 0°C, and using a 30 W radio frequency (RF) power for 6 minutes.

The next phase involved metallization, where two metal layers - 10 nm Ti and 100 nm Au - were deposited on the wafer using electron beam evaporation at rates of 0.1 and 0.5 nm/s, respectively. The polystyrene particles were then removed using adhesive cello-tape, leaving the formation of hexagonal hole arrays on the quartz substrate.

To finalize the process, the prepared AuNhA underwent sonication in acetone and isopropanol for 5 minutes, followed by a rinse with Milli-Q water and drying under a stream of N_2. The final step involved treating the AuNhA with oxygen plasma (O_2 at 0.5 mbar, 50% power for 3

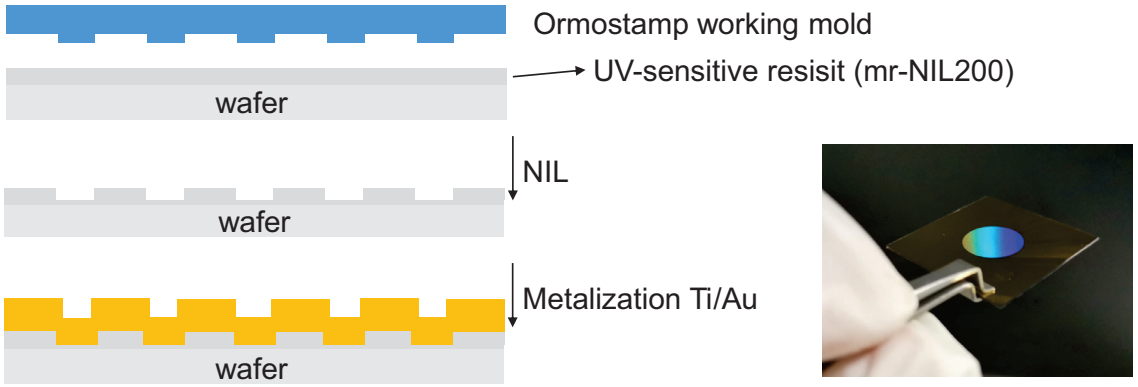

Figure 3.4: Left: schematic view of the fabrication process, including the NIL process between the Ormostamp working mold and UV-sensitive resist (mr-NIL200), and the metalization process of 20 nm Ti and 40 nm Au layers. Right: a digital photograph of the AuNpA (diameter of the patterned area is 1 cm).

minutes), sonication in ethanol for 5 minutes to reduce any gold oxides formed, a final rinse with Milli-Q water, and drying with N_2 for further use.

3.3.3 AuNpA with fringe structures fabrication based on direct NIL

The methodology for fabricating the AuNpA was further improved and simplified, building upon the AuNpA fabrication using Cr as hard mask [12]. We enhanced the efficiency of the process by incorporating a direct NIL technique, thereby eliminating the complex layer etching steps as depicted in Figure 3.4.

The procedure began with a master stamp, designed with a positive pit structure, featuring a lattice constant of 500 nm and a hole diameter of 200 nm. A quartz wafer was spin-coated a thin Ormoprime resist layer as adhesion promoter. Subsequently, 80 μL of Ormostamp resist was dispensed onto the 4-inch master stamp. The quartz wafer was then placed on top of the Ormostamp droplet, allowing the resist to spread and completely fill the gap between the master stamp surface and the wafer backplane. Exposure to UV light (365 nm wavelength, mask aligner from Süss MicroTec MA/BA8) was then performed, resulting in a cross-linked pattern formation. The negative Ormostamp working mold was further processed with FOTCS vapor deposition to create a self-assembled anti-adhesion layer.

For the imprinting phase, a thin layer of UV-sensitive mr-NIL200 resist was spin-coated on a quartz wafer. The imprinting was executed at a reduced pressure of 138 mbar to ensure uniform pattern distribution across the substrate. Subsequent to the NIL process, layers of 20 nm Ti and 40 nm Au were deposited onto the mr-NIL200 resist. The final stage was dicing

the wafer into seven individual samples, each measuring 2.5 × 2.5 cm, with a patterned area of 1 cm, as illustrated in Figure 3.4.

3.4 FDTD simulations

FDTD method is a widespread numerical technique for full-wave analysis of electromagnetic fields in various media and for intricate geometries. Applications of the FDTD method cover a range of time and spatial scales, extending from subatomic to galactic lengths and from classical to quantum physics. Its versatility makes it particularly useful in several areas, including biomedicine and bioimaging, biophotonics, bioelectronics, and biosensors [102].

3.4.1 FDTD simulation for AuNpA and AuNhA

Lumerical FDTD simulations (2021 R1.4, Lumerical Solutions) were employed to optimize the transmission spectra of various geometrical parameters and also the distribution of the electric fields on the gold nanostructures. The models for the quartz, titanium (Ti), and gold (Au) layers were sourced from the software's standard material database. For the simulations, perfectly matched layer (PML) boundary conditions were employed along the propagating direction (z-direction). To reduce the simulation volume and time, anti-symmetric and symmetric boundary conditions were applied along the x- and y-directions, respectively. The spatial steps of the discrete mesh grid in the simulation were set as $\Delta x = \Delta y = 5$ nm, $\Delta z = 2.5$ nm, ensuring a fine resolution for accurate simulation results.

3.4.2 FDTD simulation for AuNpA with fringe structures using ideal and AFM models

The material parameters for quartz, Ti, and Au layers were also obtained from the software's standard material database. The refractive index (n) and extinction coefficient (k) data for the mr-NIL200 resist were determined using an Ellipsometer SE800 (Sentech GmbH, Germany).

The ideal simulation model was created with a uniform arrangement of hexagonal pit arrays, devoid of fringe structures. To enhance efficiency and reduce computational load, anti-symmetric and symmetric boundary conditions were again applied along the x and y directions.

To more accurately simulate real fabricated surfaces, the surface topography and dimensions of the AuNpA with fringe structures were imported from AFM matrix data (x, y, and z data points) into the software's working space, and periodic boundary conditions were applied in the x and y directions.

In both cases, a PML was employed in the z direction under normal incidence. The spatial steps of the discrete mesh in the simulation were set as $\Delta x = \Delta y = 4$ nm, and $\Delta z = 1$ nm (Using a smaller mesh size can bring the simulation results closer to theoretical predictions, but it also increases the simulation time. The mesh size chosen here is due to the complexity of the imported AFM surface). In contrast to the ideal model, which was entirely computer-generated, the imported AFM profiles replicate all topographical features of the fabricated nanopit array, including surface roughness and imaging artifacts.

3.5 Morphological characterization

Atomic force microscopy (AFM), scanning electron microscopy (SEM), and focused ion beam (FIB) are fundamental tools in the field of material characterization, each offering unique insights into the properties of materials at the nanoscale.

3.5.1 AFM measurements

AFM is a type of scanning probe microscopy that employs a micromachined cantilever with a sharp tip to scan surfaces and measure the tip's deflection due to forces like electrostatic and van der Waals interactions between atoms on the tip and the conducting and nonconducting materials. Different operational modes of AFM, such as contact (static) and dynamic modes (tapping, non-contact, peakforce tapping), are selected based on the nature of tip-sample interactions. The tapping mode currently is the most popular AFM imaging mode. In tapping mode, the cantilever of the probe oscillates in the vertical direction (Z-direction) at or near its resonance frequency so that the AFM tip taps the specimen lightly, which uses the amplitude of cantilever oscillation to detect changes in the tip-sample interaction forces and thereby the sample topography [132, 133].

AFM imaging was performed using a Bruker Nanoscope V Multimode AFM setup (Bruker, USA) to characterize the surface topography with high resolution. The images were acquired in tapping mode with tesp-v2 cantilevers (Tip radius: 7 nm, length: 123 μm, width: 40 μm, Bruker, USA).

3.5.2 SEM measurements

SEM, on the other hand, is a powerful and versatile tool for examining surface topography of conducting and semiconducting materials. In SEM, the sample is shot with high-energy electrons, and the resultant secondary electrons/X-rays/backscattered electrons are then analyzed. The analysis yields detailed insights into the topography, morphology, composition, grain orientation, crystallographic structure, and other pertinent characteristics of the material. SEM is particularly valued in nanoscience due to its non-destructive nature and ability to produce high-quality images [134, 135].

SEM was utilized to obtain high-resolution morphology of the samples by means of Zeiss Gemini 1550 system (Zeiss, Germany) employing an in-lens detector with different applied acceleration voltage.

3.5.3 FIB measurements

FIB technology, typically using Ga^+ ions, is known for its precise material ablation capabilities at the micrometric scale. By integrating with SEM in dual FIB-SEM systems, it allows for simultaneous imaging and material modification. The secondary electrons emitted during the ion-sample interaction in FIB provide valuable imaging data, enhancing the ability to study materials in great detail [136, 137].

FIB was implemented using HELIOS NanoLab 600i (FEI Deutschland GmbH, Frankfurt, Germany) by a dual-beam microscope with an electron beam and galium ion beam under an angle of 52°. In order to protect the region of interest during the sectioning process, a thin layer of platinum was deposited by electron beam induced deposition. Then, a thick layer of platinum layer was deposited via ion beam induced deposition.

Together, AFM, SEM, and FIB are indispensable in material science, each contributing uniquely to the understanding of material properties. AFM provides detailed topographical data, SEM offers fast imaging and morphological information, and FIB enables precise material modification and subsurface examination. These techniques are essential for advancing knowledge in nanotechnology and materials science.

3.6 Plasmonic and electrochemical dual signal measurements

The monitoring of biomolecular interactions is a key requirement for the study of complex biological processes and the diagnosis of disease. Technologies that are capable of providing label-free, real-time insight into these interactions are of great value for the scientific and

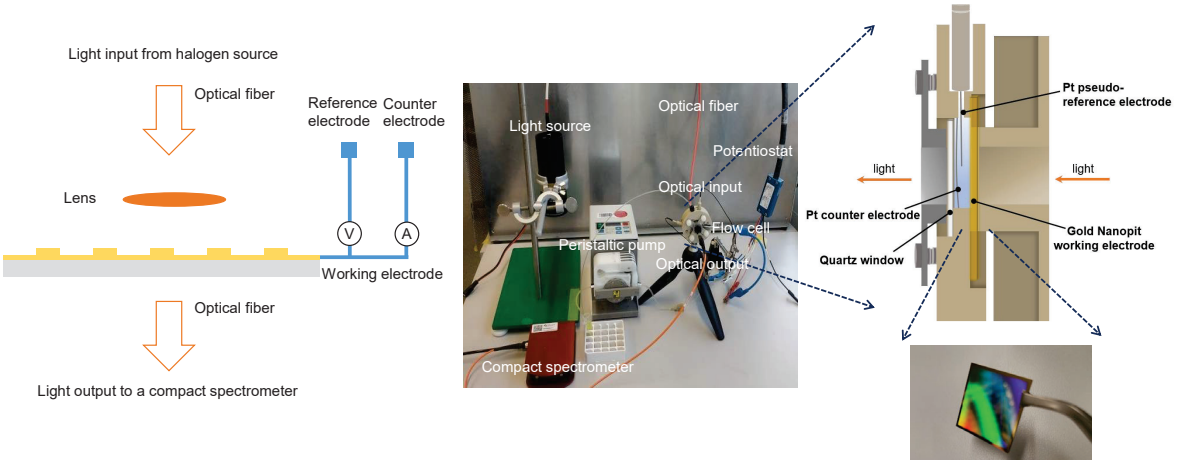

Figure 3.5: Schematic of the simultaneous SPP-EC dual signal experimental setup.

clinical communities. Greater understanding of biomolecular interactions alongside increased detection accuracy can be achieved using technologies that can provide parallel information about multiple parameters of a single biomolecular process [112]. Here, two plasmonic and electrochemical combination methods for optical-electro biosensing were presented, namely, surface plasmon polaritons and electrochemical (SPP-EC) technique and plasmon-enhanced fluorescence and electrochemical (PEF-EC) technique.

3.6.1 SPP-EC experimental setup

The used SPP-EC experimental setup is depicted in Figure 3.5. For the optical part, an unpolarized halogen lamp was used, given that the hexangular nanopit arrays are symmetric and the transmittance at normal incidence is not dependent on the polarization. The light transmitted through the AuNpA was directed into a compact spectrometer (Thorlabs CCS200, USA). Transmittance spectra were determined by calculating the ratio of the spectra of the transmitted light from the Tris buffer solution with modified AuNpA against the blank Tris buffer solution. During the plasmonic characterization, the integration time was set to 1.8 ms and recorded with 200 spectrum frames. A custom Python script (see Appendix) using sklearn package was applied to fit a third-order polynomial function around the average fitted SPP peak, enabling us to track the peak wavelength value.

Simultaneously, the electrochemical part of the experiment was conducted by a spectro-electrochemical flow cell designed with a reduced optical path (Redoxme AB, Sweden) at room temperature. The flow cell consists of a polyether ether ketone flow chamber, equipped with a magnetic mount to hold the electrode (25×25 mm^2). The chamber's internal volume of 0.7 mL allowed for a shortened optical path of 4 mm. The AuNpA samples were firstly cleaned using a sequence of acetone and isopropanol sonication (5 min), followed by rinsing with Milli-Q

water and drying with N_2. An oxygen plasma treatment (O_2 pressure 0.5 mbar, 50% power, 5 min) and subsequent immersion in ethanol were performed to reduce any gold oxides formed. The samples were then dried with N_2 and mounted in the cell as the working electrode. For the electrochemical measurements, a Pt wire (50 mm long) in the sample solution served as a pseudo-reference electrode, and a Pt wire (90 mm long) as the counter electrode. The arrangement of these three electrodes was illustrated on the right side of Figure 3.5. ACV measurements were executed using a potentiostat (Autolab PGSTAT302, Eco Chemie, the Netherlands) with NOVA software (version 2.1). The experiments were conducted in a Tris buffer solution, setting the ACV scan range between -0.1 and 0.7 V, with potential steps of 0.01 V, modulation amplitude of 0.04 V, modulation time of 0.4 s, frequency of 20 Hz, and an interval time of 0.8 s.

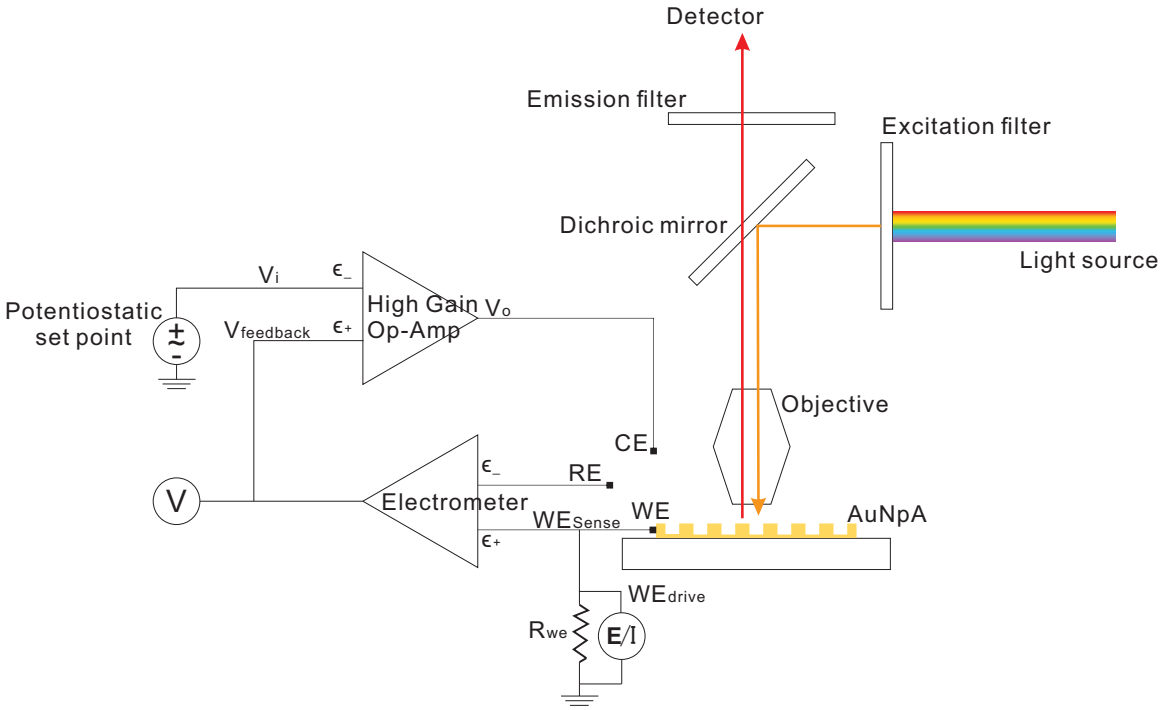

Figure 3.6: The schematic representation of the PEF-EC dual signal measurement setup. V_i represents a user-controlled applied potential called the potentiostatic set point that is referenced to ground. V_i enters the inverting input (ϵ_-) on the High Gain Operational Amplifiers (Op-Amp). The output (V_o) connects to the counter electrode lead (CE). The reference electrode lead (RE) and the working sense lead (WE) connect to a true difference amplifier called the electrometer. The output voltage ($V_{feedback}$) from the electrometer feeds into a voltmeter (V) and into the non-inverting input (ϵ_+) on the High Gain Op-Amp. The working electrode drive lead (WE_{drive}) connects to a sense resistor (R_{we}) that connects to ground. The voltmeter (E/I), measures the potential across R_we, and converts it to a current. WE_{sense} and WE_{drive} are shorted together and connect to the WE of interest. CE, RE, WE are all cables that come out of the potentiostat and connect to the electrochemical cell. The potentiostat circuit diagram is reproduced from reference [138].

3.6.2 PEF-EC experimental setup

The setup for the PEF-EC dual signal measurement is depicted in Figure 3.6. Fluorescence microscopy images were acquired using a ZEISS Axio Imager Z1, which was equipped with an Illuminator HXP120 light source, a 63× water immersion objective (Plan-Achroplan, NA 1.0), Zeiss 50 filter sets for specified wavelengths (Excitation 640/30 nm, Beamsplitter: 660 nm, Emission: 690/50 nm), an Analy differential interference contrast (DIC) transLight, and an AxioCam MR R3 digital CCD camera. The images had a scaled size of 142.10 μm × 106.48 μm, a 16-bit dynamic range, and a pixel scale of 0.102 μm × 0.102 μm. Each fluorescence image was captured with an exposure time of 500 ms. The arithmetic mean fluorescence intensity was quantified by calculating the entire image area using ZEN Blue Edition 2012 software, as the aptamer-target binding homogeneously occurred across the AuNpA surface.

Electrochemical measurements were conducted using a portable EmStat potentiostat (Palm Sense, the Netherlands), connected with a same PC through PSTrace 5.9 software for data acquisition and analysis. The custom-built reaction chamber, 3D printed with clear resin, featured a semi-open central area to accommodate the AuNpA as the working electrode while allowing access for the microscope's objective lens. The chamber was designed for easy addition and rinsing of the solution using a pipette and a peristaltic pump, respectively. Two Pt wires connected to the EmStat served as pseudo-reference and counter electrodes. The use of a small, less stable Pt pseudo-reference electrode was necessitated by the compact design of our portable electrochemical system [139]. SWV was employed for the electrochemical characterization of the sensor, with scan range from -0.6 to -0.2 V. These scans included an equilibration time of 5 s, potential steps of 0.005 V, an amplitude of 0.02 V, and a frequency of 5 Hz.

3.7 Fluorescence lifetime imaging microscopy characterization

The fluorescence lifetime imaging microscopy (FLIM) data presented here were recorded in collaboration with Dr. Thomas Gensch from IBI-1. FLIM with pulsed, two-photon excitation for was performed to determine the spatial distribution of fluorescence lifetimes using a laser scanning fluorescence microscope (LSM880, Zeiss, Jena, Germany) equipped with a 20×water immersion objective (NA 1.0, WD 2.1mm; Zeiss, Jena). For the excitation of MB (in the form of S1/S2_20T_MB), a wavelength of 925 nm (120 fs pulses with 80 MHz repetition frequency (Insight X3; Newport, Spectra Physics, Palo Alto, USA)) was chosen and its fluorescence was detected after reflection on a dichroic mirror (LBF 690++, Zeiss), and passing through another near-infrared light-blocking short-pass filter (760++, Zeiss) and a broad band-pass

filter covering almost the entire visible spectrum (400-650 nm; ET650sp-2p, LOT, Darmstadt, Germany). This filter combination ensured that no scatter signal of the excitation light (925 nm) reached the detector, also ensured by the very low excitation powers ($\leq$ 2 mW) used with the Au-samples. Fluorescence photons were detected with a GaAsP hybrid photodetector (HPM-100-40, Becker & Hickl, Berlin, Germany). TCSPC electronics (SPC-152; Becker & Hickl) and acquisition software were used for FLIM [140, 141]. Fluorescence lifetime images were generated using SPCImage 8.8 (Becker & Hickl).

3.8 Quartz crystal microbalance characterization

The quartz crystal microbalance (QCM) was equipped with a fluidic system provided by Q-sense Biolin Scientific (Västra Frölunda, Sweden) to utilized to the mass change associated with the immobilization of S1, PEG blockers (alternative molecules of 6-MCH), S2_20T_MB aptamer, and the S protein. The cleaning protocol for both, the QCM components and the Au sensor, was conducted following the manufacturer's guidelines.

In the initial stage, the QCM Au chip underwent a treatment involving a 3-minute treatment at 50% power and 0.5 mbar in an oxygen plasma oven. This was followed by a subsequent 5-minute ethanol immersion to counter the formation of gold oxide resulting from the plasma exposure. Once this cleaning and activation procedure was complete, the chip was mounted to the microbalance module, followed by the attachment of the fluidic cell. By introducing a Tris buffer solution, a continuous flow was established through the cell until the sensor signal exhibited stability, as indicated by a frequency shift under 0.2 Hz over a 10-minute interval. Subsequently, the experimental procedure was initiated, involving the sequential infusion of molecule solutions followed by a subsequent rinsing step employing a Tris buffer through the QCM cell.

3.9 Surface plasmon resonance microscopy characterization

The surface plasmon resonance microscopy (SPR-M) data presented here were recorded together with Justus Bednár. The employed SPR-M setup is a self-built prototype that uses a HeNe-Laser light source of (632.8 nm) wavelength [142–144]. This light is focused onto a 47 nm thick Au layer using an NA 1.7 APON100×HOTIRF objective from Olympus, specifically for the excitation of SP. The coupling from the objective to the Au-layer is facilitated through use of a high refractive index immersion oil (Cargille Series M, n_D = 1.705-1.800 $\pm$ 0.0005), a high refractive index Lanthan-Flint cover glass (N-LAF21) from SCHOTT), and a 3 nm Cr adhesion layer. Due to the (quasi-)radial polarization of the laser

source, the limited propagation length of surface plasmons allows for a localized response from the Au surface [145]. This way, the SPR-M can probe points in a scanning fashion, using a piezo-electric xy-stage.

4 Results and discussion

In the pursuit of enhancing biosensor reliability and versatility, the study integrated the advantages of dual-transducer systems, focusing on surface plasmon polaritons (SPP) due to its high sensitivity to refractive index changes and its potential for miniaturized, label-free detection. Current state-of-the-art biosensors focus on single-transducer systems that often lack the comprehensive detection range and sensitivity required for complex biological samples, therefore, the approach aimed to transcend these limitations through innovative dual-transducer designs.

The first aptasensor combined SPP and electrochemical (EC) detection using AuNpA. The choice of non-fully penetrating AuNpA was motivated by its sharp plasmonic spectrum and enhanced refractive index sensitivity, as confirmed by finite-difference time-domain (FDTD) simulations and experimental results. The SPP-EC dual-signal detection was achieved by functionalizing these structures with Ferrocene (Fc)-labeled human serum albumin (HSA) aptamer receptors. The binding of HSA to the aptamer induced conformational changes, resulting in measurable variations in both electron transfer at the EC interface and SPP wavelength shifts. The EC transducer demonstrated a dynamic detection range from 1 nM to 600 μM, while the optical transducer was effective from 100 μM to 600 μM. Each transducer exhibited distinct limits of detection (LOD), dynamic ranges, and sensitivities, showcasing the versatility and robustness of the dual-signal approach. This novel method not only enhances the design of plasmonic nanostructures but also shows significant potential for dual-signal disease diagnostics and point-of-care (POC) testing applications.

The second aptasensor employed a combination of plasmon-enhanced fluorescence (PEF) and EC transduction mechanisms, utilizing direct nanoimprint lithography (NIL) to fabricate AuNpA with unique fringe structures. These structures facilitated SPP excitation and the PEF effect. The PEF-EC dual-transduction was achieved by using an aptamer-associated fluorophore, methylene blue (MB), for simultaneous fluorescence and EC measurements. Specifically, for detecting the SARS-CoV-2 Spike protein (S protein) via a C7 aptamer and strand displacement protocol, the PEF transducer achieved a detection range from 1 fg/mL to 10 ng/mL with an LOD of 0.07 fg/mL, while the EC transducer extended the range from 1 fg/mL to 100 ng/mL with an LOD of 0.15 fg/mL. Notably, this dual-transducer aptasensor maintained stability in a diluted 10% human saliva matrix. The results demonstrate not only

a straightforward large-scale fabrication process for nanostructures enabling PEF but also a substantial advancement in the understanding of their optical properties, paving the way for a sophisticated and universal aptasensor platform.

4.1 SPP-EC aptasensor based on AuNpA for the detection of HSA

The combined plasmonic and electrochemical approach is commonly referred to in the literature as "electrochemical surface plasmon resonance" (SPR-EC or eSPR). Most commercial SPR and research instruments are still based on the classical Kretschmann configuration, which relies on the phenomenon of total internal reflection [110]. For example, Lu et al. [146] proposed a novel EC-SPR method utilizing electrochemical impedance spectroscopy, which is highly sensitive to molecular binding on the chip surface while being less affected by bulk refractive index changes or nonspecific binding. Additionally, Salamifar et al. [147] employed SPR-EC to distinguish between nonspecific binding of random targets to the biorecognition probe and nonspecific adsorption of matrix contaminants on the monolayer by simultaneously monitoring both optical and electrochemical signals.

However, considering the portability and the need for point-of-care testing (POCT) in biosensor development, it is essential to miniaturize the setup. One primary method is employing the extraordinary optical transmission (EOT, see section 2.6) configuration, a resonant phenomenon at the nanoscale resulting from the coupling between light and surface waves. EOT-based sensing offers a significant advantage over Kretschmann-style SPR chemical sensors due to its inherently nanometer-micrometer scale, making it particularly suitable for miniaturization [148].

The first investigation was employing the SPP-EC protocol for simultaneously electrochemical and plasmonic detection. The AuNpA, fabricated by NIL using Cr layer as hard mask, unlike fully hole geometries, exhibits sharper plasmonic spectral width, higher refractive index sensitivity, and an enlarged electrochemically active surface area. This unique combination, studied here for the first time, is employed for HSA detection. The AuNpA serves as both the working electrode for electrochemical measurements and the metal surface for recording SPP peak shifts in transmitted light, which were expected enhance the diagnostic accuracy, reliability, and broadening the detection range. This novel dual-transducer aptasensor contributes to the evolution of biosensing strategies, offering improved selectivity and reliability in HSA detection for diverse applications.

4.1.1 Periodicity optimization by FDTD simulation

The emergence of EOT, icharacterized by transmission spectrum peaks in a film that exceed the anticipated efficiency based on traditional aperture theory, results from a complex mechanism of surface plasmon excitation. This mechanism is inherently dependent on the geometric structure of the sample surface [149]. SPP can be excited when the oscillations of surface charges at the metal interface correspond with the wavevector of the incident photon, matching the grating on the metal according to the equation (4.1) [150–152]:

$$\vec{k}_{sp} = \vec{k}_x \pm i\overrightarrow{G_x} \pm j\overrightarrow{G_y} \tag{4.1}$$

The dispersion relation for surface plasmons defines $\vec{k}_{\mathrm{sp}} = 2\pi/\lambda\sqrt{\varepsilon_m\varepsilon_d/\left(\varepsilon_m + \varepsilon_d\right)}$ as the surface plasmon wave vector. Here, ε_m and ε_d are the dielectric constants of the metal and dielectric layer, $\vec{k}_x = (2\pi/\lambda)\sin\theta$ is the incident photon wave vector's component parallel to the grating plane, with θ being the incidence angle with respect to the normal of the interface, $\vec{G}_x, \vec{G}_y = 4\pi/\sqrt{3}P$ are the reciprocal lattice vectors for the hexagonal array of nanoholes, and i and j are integers, representing the array's scattering orders.

Nanohole arrays, as high aspect-ratio nanostructures on metallic surfaces, exploit EOT to generate intense electric fields in the subwavelength regime. These metallic surfaces facilitate surface plasmon excitation even under incoherent light sources. Spectral analysis of transmission peaks, indicative of local refractive index alterations, can be conducted using a portable spectrometer to exploit various plasmonic modes [153].

For SPP sensors that employ a periodic hexagonal array of nanoholes under normal incidence, equation (4.1) simplifies, allowing the resonance wavelength to be calculated using equation (4.2) [28, 154]:

$$\lambda_{\mathrm{SPP}} = \frac{P}{\sqrt{\frac{4}{3}\left(i^2 + ij + j^2\right)}}\sqrt{\frac{\varepsilon_{\mathrm{m}} n^2}{\varepsilon_{\mathrm{m}} + n^2}} \tag{4.2}$$

Where n is the refractive index of the dielectric layer. The refractive index sensitivity of an SPP sensor can be derived by taking the first-order derivative of equation (4.2) over n as shown in equation (4.3):

$$\mathrm{S} = \frac{\mathrm{d}\lambda_{\mathrm{SPP}}}{\mathrm{d}n} = \frac{P}{\sqrt{\frac{4}{3}\left(i^2 + ij + j^2\right)}}\sqrt{\left(\frac{\varepsilon_{\mathrm{m}}}{\varepsilon_{\mathrm{m}} + n^2}\right)^3} \tag{4.3}$$

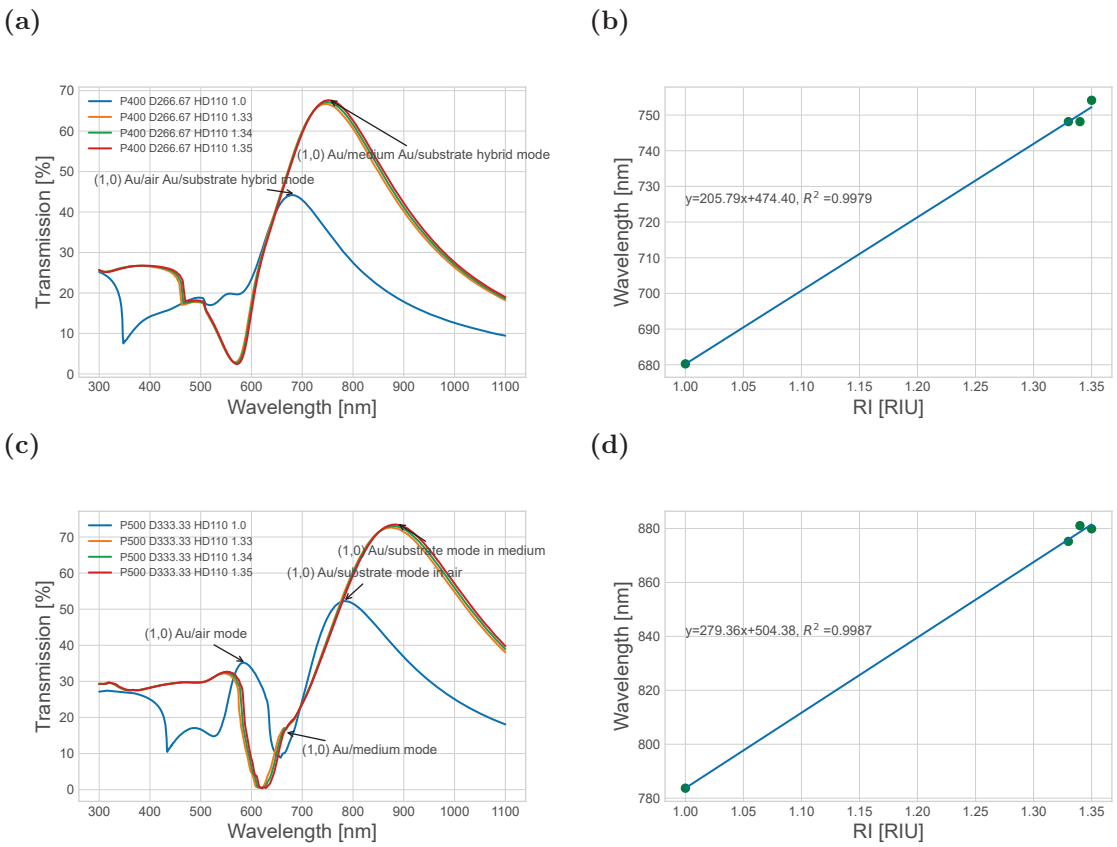

Figure 4.1: FDTD simulation spectrum of the fully penetrating AuNhA with different periodicity (Periodicity/Diameter = 1.5) and corresponding refractive index sensitivity of the (1,0) Au/medium mode including periodicity of 400 nm (a, b), 500 nm (c, d).

This equation reveals that the refractive index sensitivity of SPP modes is primarily determined by the periodicity and scattering orders. However, it's also acknowledged that factors such as aperture size and the specific characteristics of metallic nanostructures significantly influence the EOT properties [14].

In the initial simulations, a hexagonal array of AuNhA was modeled with a 10 nm titanium adhesion layer and a 100 nm gold layer, maintaining a constant ratio of periodicity to diameter (P/D = 1.5) ranging from 400 nm to 800 nm. The parameters of periodicity (lattice constant), hole diameter, and total hole depth are denoted as P, D, and HD, respectively (HD = 110 indicates a complete hole structure in both Ti and Au layers). The simulation results, illustrated in Figures 4.1 and 4.2, focused on the (1,0) Au/medium mode. This mode demonstrates greater refractive index sensitivity compared to the (1,0) Au/substrate mode due to its accessible and extensive local electromagnetic fields, which enhance the spatial overlap between the optical fields and biomolecules [155, 156].

For a periodicity of 400 nm, a single broad (1,0) Au/medium and Au/substrate hybrid peak

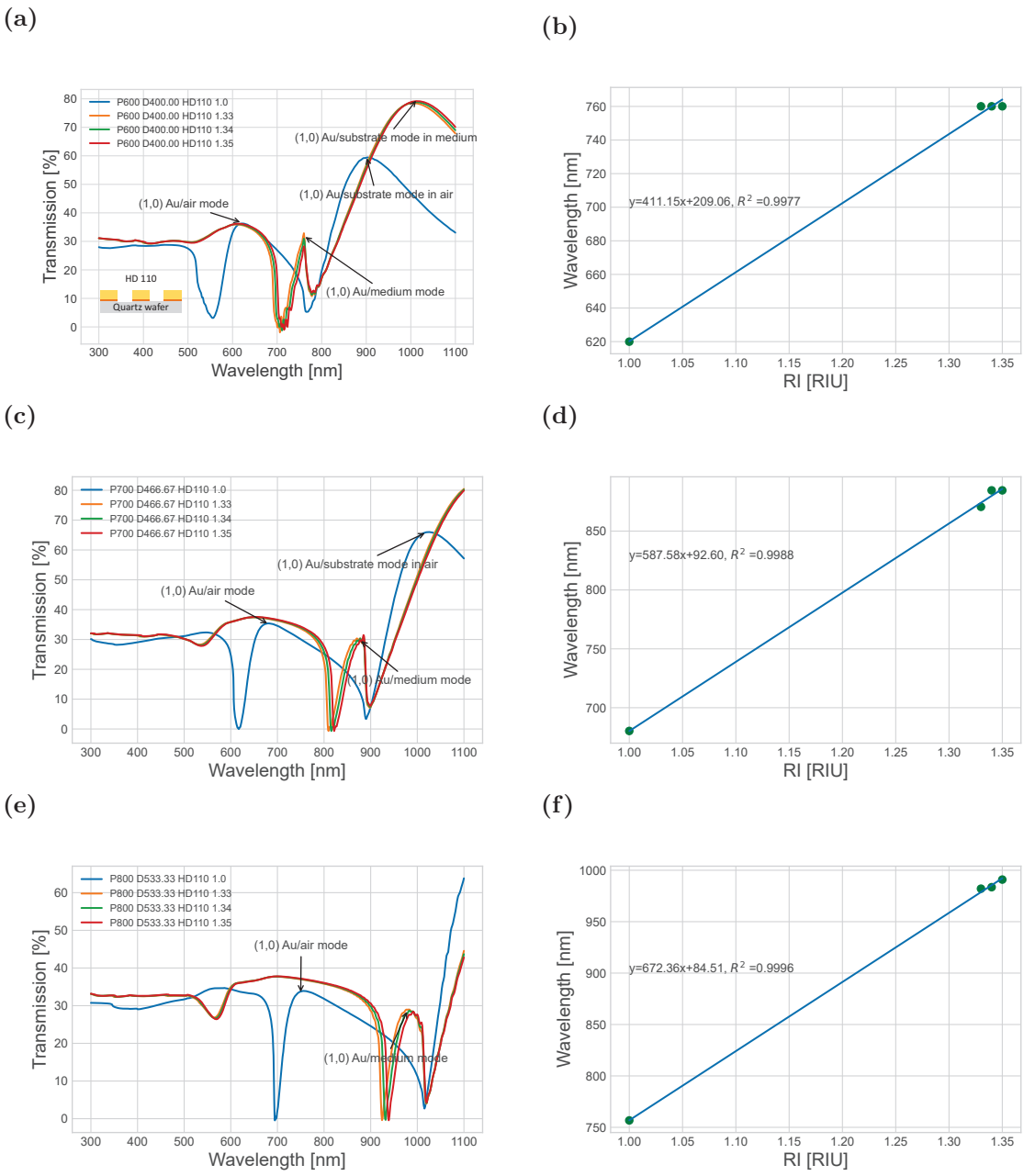

Figure 4.2: FDTD simulation spectrum of the fully penetrating AuNhA with different periodicity (Periodicity/Diameter = 1.5) and corresponding refractive index sensitivity of the (1,0) Au/medium mode including periodicity of 600 nm (a, b), 700 nm (c, d), and 800 nm (e, f).

Table 4.1: Sensitivity, transmittance, FWHM, and FOM of the (1,0) Au/medium mode changing with periodicity.

Periodicity (Lattice constant) nm	Sensitivity nm/RIU	Transmittance % (RI = 1.0/1.33)	FWHM nm (RI = 1.0/1.33)	FOM (RI = 1.33)
400	205.79	44.2/66.7	253/313	0.66
500	279.36	35.2/72.6	94.4/376	0.74
600	411.15	36.3/32.9	164.9/34.7	11.85
700	587.58	35.4/30.4	278.3/56.0	10.49
800	672.36	33.9/29.0	261.4/73.0	9.21

was observed that shifts with varying refractive index. At 500 nm periodicity, the (1,0) Au/medium mode becomes less distinguishable, overshadowed by the broad (1,0) Au/substrate mode in the medium (Figure 4.1).

Conversely, at periodicities of 600 nm, 700 nm, and 800 nm (Figure 4.2), the (1,0) Au/medium modes are readily identifiable. The findings indicate that increased periodicity enhances sensitivity, as summarized in Table 4.1. However, considering the detection capabilities of our portable optical spectrometer (CCS200 - Compact Spectrometer, Extended Range: 200 - 1000 nm) and actual measurements in an aqueous medium with a refractive index around 1.33, a 600 nm periodicity emerges as the optimal choice. This periodicity not only ensures high sensitivity and transmittance but also achieves the highest figure of merit (FOM) value (11.85 RIU^{-1}), where FOM is defined as the ratio of sensitivity (S) to the full width at half maximum (FWHM) of the resonant peak (FOM = S/FWHM [157]).

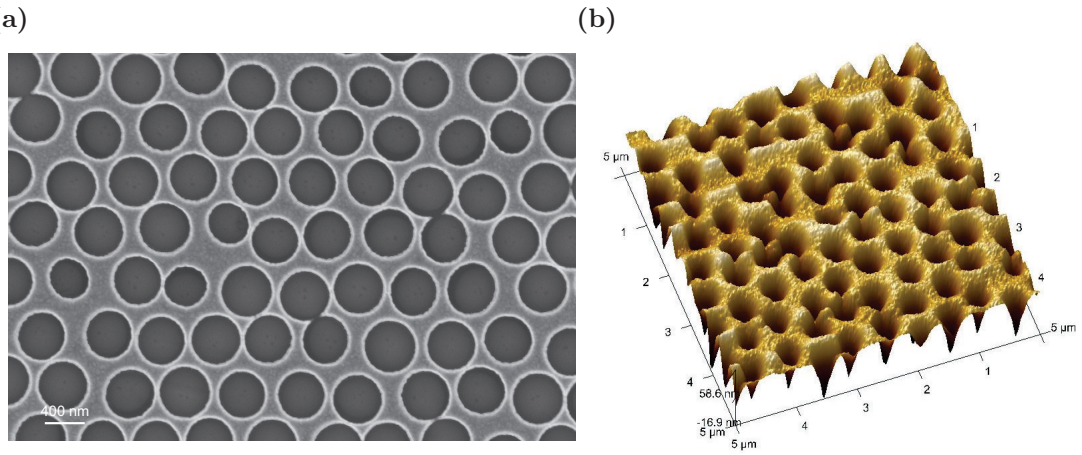

Figure 4.3: SEM (a) and AFM (b) images of the fabricated fully AuNhA (periodicity 600 nm) by NSL.

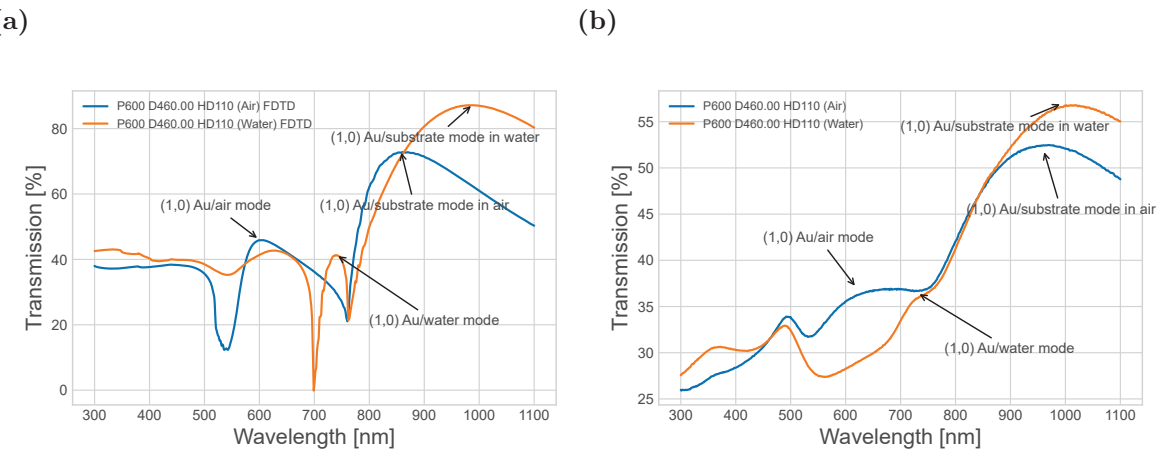

Figure 4.4: FDTD simulation(a), and measured transmission spectra (b) in air (blue line) and water medium (orange line) with P (600 nm), D (460 nm), HD (110 nm).

4.1.2 AuNhA characterization

Fully penetrated AuNhA with a 600 nm periodicity were fabricated using the NSL technique (see section 3.3.2), ensuring complete penetration through both the Ti and Au layers. Figure 4.3 shows representative AFM and SEM images of the AuNhA after the lift-off and cleaning processes. The samples exhibited regular hexagonal nanohole patterns, with an average periodicity of 601.3 ± 65.3 nm and a hole diameter of 459.5 ± 28.7 nm. The hole thickness, determined from AFM measurements, was 110.7 ± 5.6 nm.

Notably, this hole diameter is larger than the dimensions used in the initial simulations. Therefore, an additional FDTD simulation was conducted for AuNhA with a 460 nm diameter, considering air and water as surrounding dielectric layers (Figure 4.4a). When compared to the actual transmission measurements shown in Figure 4.4b, the (1,0) Au/medium mode was challenging to discern, particularly in water.

Clearly, there is mismatch between the simulation and real measured transmission spectra. A similar discrepancy between simulation and experimental transmission results was observed in the recent study by Zhang et al. [158]. They reported that the Au/water (1,0) SPP mode was not as pronounced in their AuNhA (with a 520 nm periodicity and 350 nm diameter) compared to their simulated spectra. One plausible explanation for this could be that the broad peak of the (1,0) Au/substrate mode overshadows parts of the adjacent (1,0) Au/medium mode peak.

To address this issue and enhance EOT transmission sensing, minimizing the (1,0) Au/substrate mode was proposed by disrupting the periodic nanostructure array at the Au/substrate interface through forming a continuous, unbroken gold film at the Au-quartz junction. Therefore, such samples were fabricated by NIL processes, featuring non-fully penetrating nanopits in the gold

film, by simply stopping the Au etching process before it reached the bottom of the Au layer. This resulting AuNpA effectively facilitated the (1,0) Au/medium mode, which was essential for sensing, while avoiding the (1,0) Au/substrate mode.

4.1.3 Hole depth investigated by FDTD simulation

To validate the hypothesis that the (1,0) Au/substrate mode shields parts of the adjacent (1,0) Au/medium mode peak, a systematic study was conducted on the impact of varying hole depths (HD) from 80 nm to 110 nm on the spectral characteristics, utilizing FDTD cross-sectional electric field distribution analysis (Figure 4.5). For structures with fully penetrating holes (HD = 110 nm), the most intense electric field is observed at the top of the gold hole ring in the (1,0) Au/medium mode at 615 nm. Importantly, the confined local electromagnetic fields at the gold surface's top extend from the electrode area into the surrounding medium, which is crucial for detecting local refractive index changes during the analyte sensing process. On the contrary, in the (1,0) Au/substrate mode at 901 nm, the near-field effects are predominantly concentrated at the interface between the gold and quartz substrate. The (1,0) Au/substrate mode has a lesser influence on the biomolecular recognition reactions and surface binding events. This distinction underlines the importance of the spatial distribution of electromagnetic fields in determining the effectiveness of the sensing mechanism.

As the hole depth (HD) was reduced, a corresponding decrease was observed in the intensity of the Au/substrate mode. Importantly, when the HD was set to 80 nm, a continuous 20 nm gold layer remained on top of the 10 nm Ti layer. At this depth, the electric field associated with the Au/substrate mode became almost negligible, indicating its effective suppression. Meanwhile, the intensity of the Au/medium mode remained relatively unchanged, aligning with the expectations. Additional transmittance spectra simulations were conducted for dielectric media with varying refractive indices, such as air (refractive index of 1.0) and water (refractive index of 1.33). These results are presented in Figure 4.6, Figure 4.2a, and Figure 4.2b. In these simulations, the (1,0) Au/medium mode was more pronounced, especially when compared to the fully penetrating hole configuration.

For an HD of 100 nm, faint Au/substrate mode peaks were still observable at a wavelength of 1000 nm. Although there was a slight reduction in transmittance, the refractive index sensitivity of the wavelength shift sensor improved as the HD decreased from 100 nm to 80 nm, as detailed in Table 4.2. It's important to note that while the sensitivity change due to varying HD is relatively minor, the FWHM of the peaks exhibited significant difference.

Considering these findings, a hole depth of either 90 nm or 80 nm appears to be an optimal balance between achieving satisfactory transmittance and minimizing FWHM. This balance

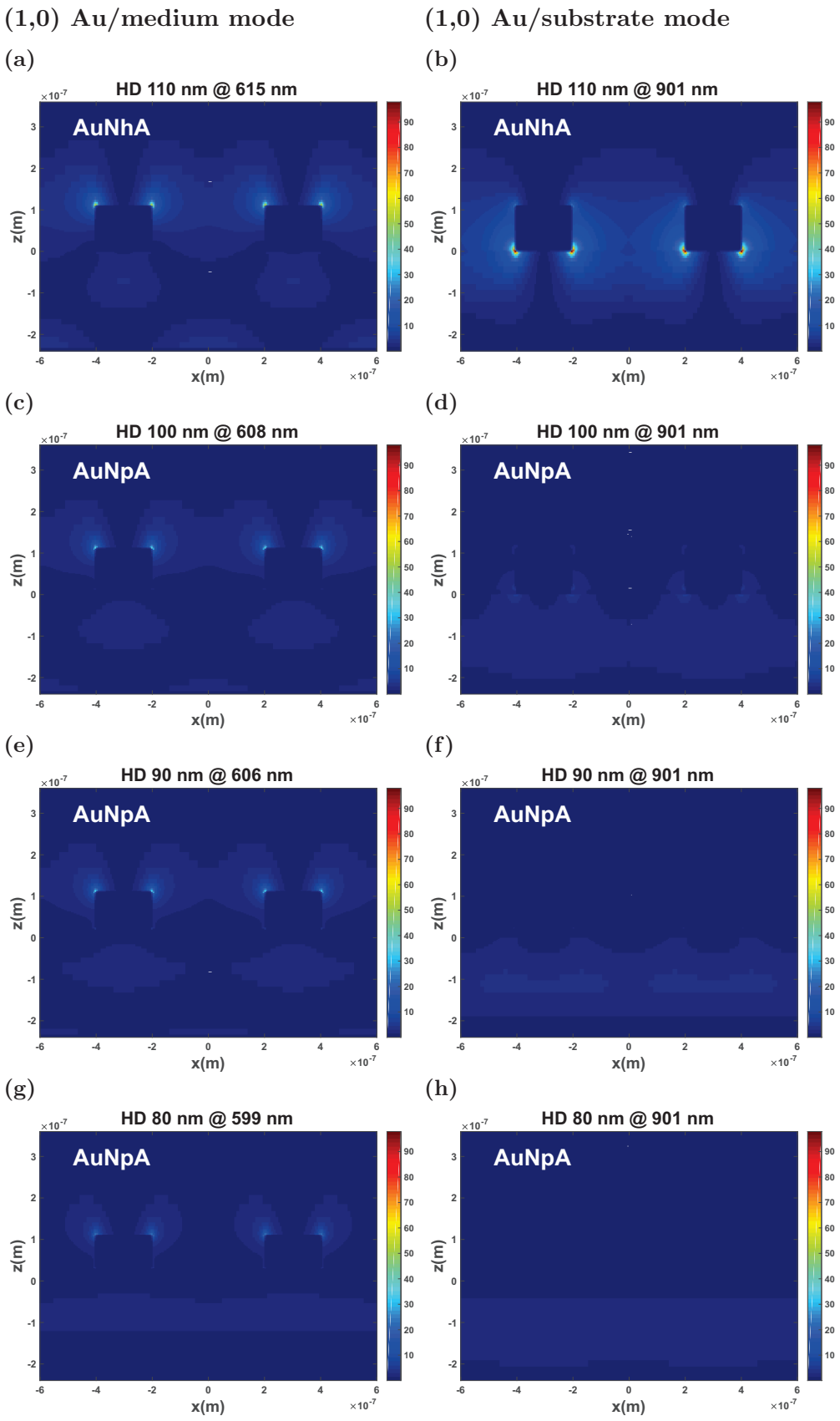

Figure 4.5: Cross-sectional electric field distribution of (1,0) Au/medium mode (a,c,e,g) and (1,0) Au/substrate mode (b,d,f,h), when hole depth varies from 110 nm to 80 nm.

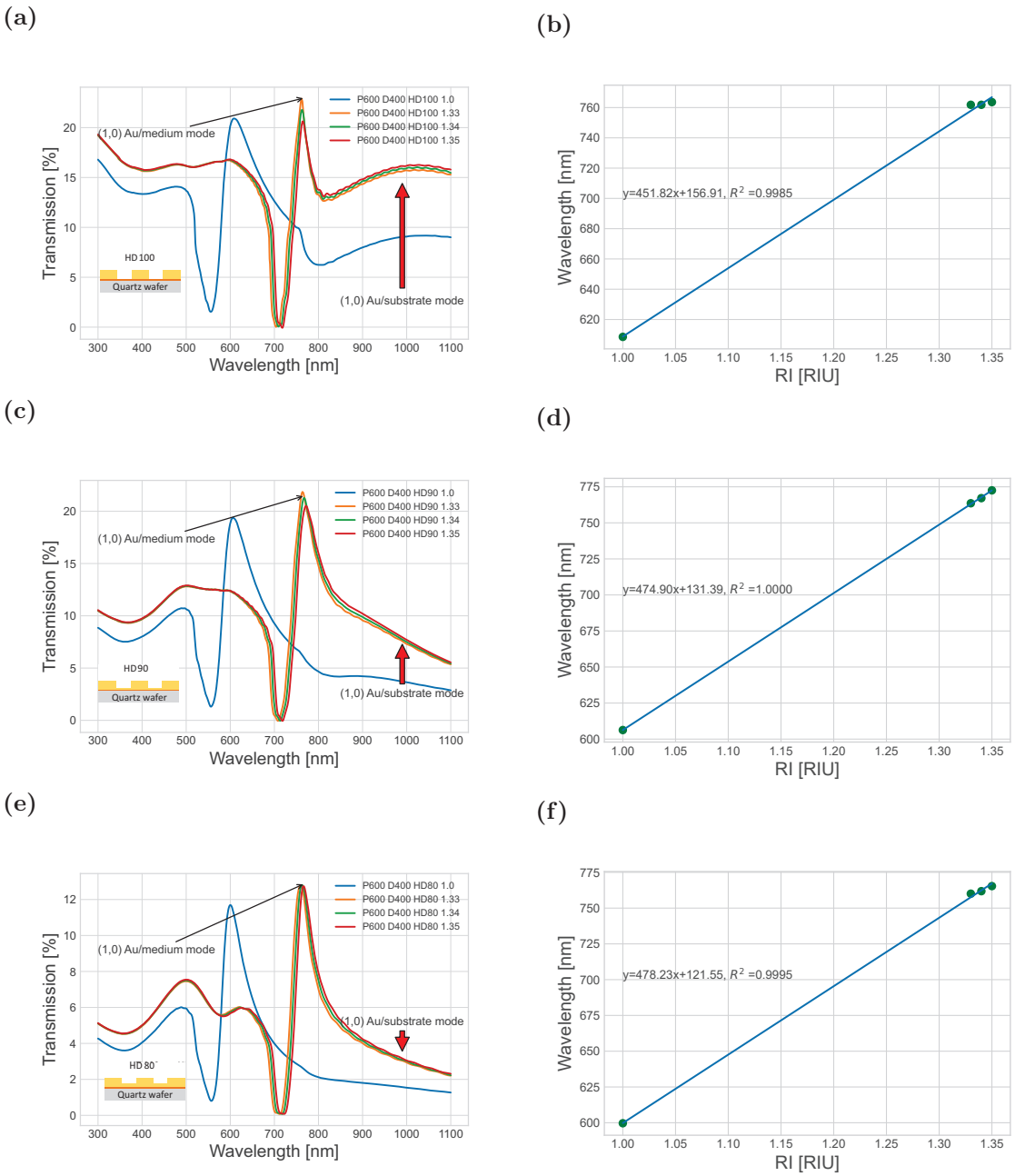

Figure 4.6: FDTD simulation spectrum of AuNpA (with periodicity of 600 nm and diameter of 400 nm) with different hole depth from 100 nm, 90 nm, and 80 nm (a, c, e), respectively and corresponding refractive index sensitivity of the (1,0) Au/medium mode (b, d, f).

Table 4.2: Sensitivity, transmittance, FWHM, and FOM of the (1,0) Au/medium mode changing with hole depths between 80, 90, and 100 nm.

Hole depth nm	Sensitivity nm/RIU	Transmittance % (RI = 1.0/1.33)	FWHM nm (RI = 1.0/1.33)	FOM (RI = 1.33)
100	451.82	20.9/22.9	161.0/71.5	6.32
90	474.90	19.4/21.9	113.2/95.1	4.99
80	478.23	11.7/12.8	79.8/71.1	6.73

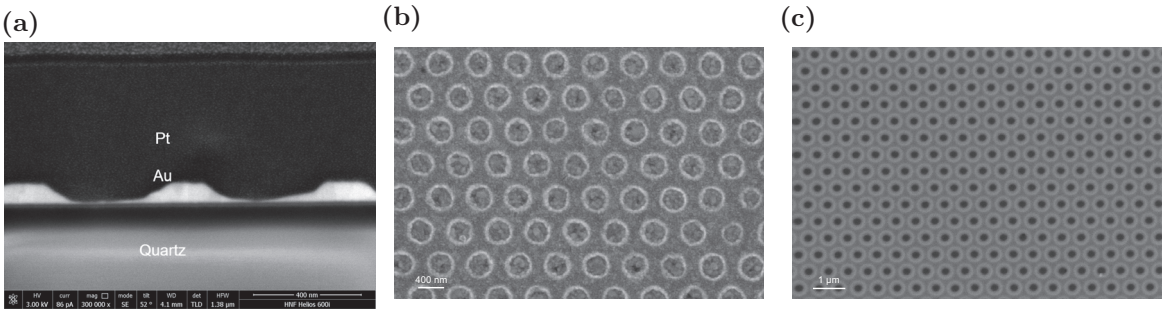

Figure 4.7: FIB cross-section image (a, title angle = 52°) and SEM image (b) of the fabricated AuNpA, SEM image of the Si/SiO_2 master mold (c).

is crucial since low transmittance can lead to high noise levels and complicate peak fitting, impacting the overall performance of the sensor system.

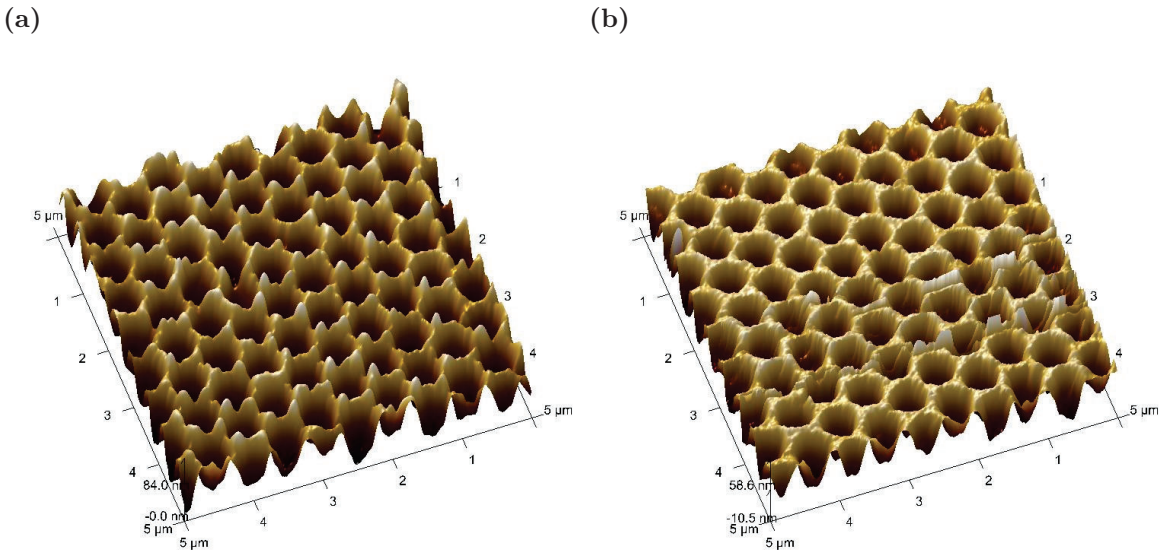

Figure 4.8: AFM images of the AuNpA with Cr residue before (a) and after wet etching (b).

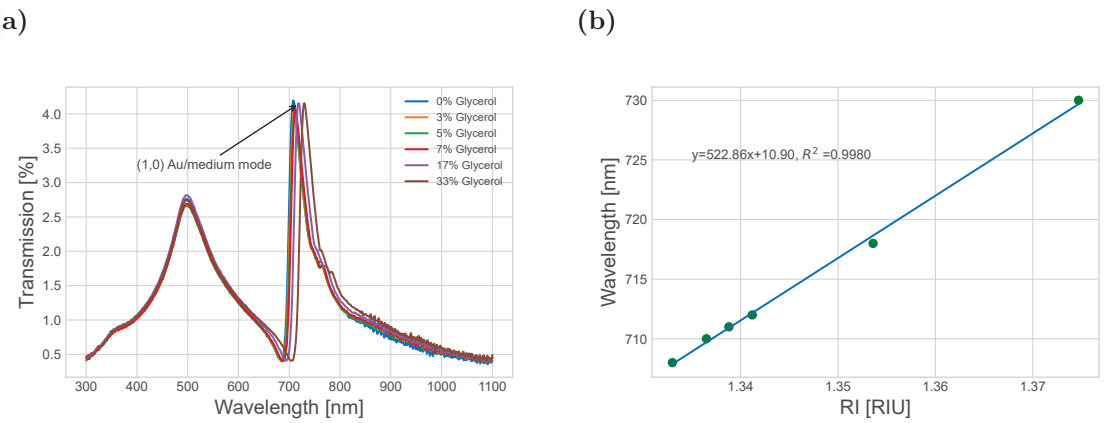

Figure 4.9: Experimental refractive index sensing over a wide concentration range of glycerol aqueous solutions (a, mass percentage), peak wavelength regression fitting as a function over refractive index (b).

4.1.4 AuNpA characterization

The surface morphology of the AuNpA fabricated by NIL, was characterized through SEM/FIB and AFM analyses. The FIB cross-section image (Figure 4.7a) revealed that the gold film was not entirely etched through, leaving a residual continuous metal layer. Additionally, the isotropic nature of the dry etching process led to the formation of curved sidewalls. The average periodicity and diameter of the nanopit arrays were measured to be 600 ± 20 nm and 397 ± 18 nm, respectively, as depicted in Figure 4.7b. The isotropic chemical etching process is responsible for the larger hole diameter compared to that of the master mold, as shown in Figure 4.7c. Prior to wet etching, the hole thickness was measured at 98 ± 2 nm (Figure 4.8a), whereas after wet etching, it was reduced to 87.9 ± 8.7 nm, as shown in Figure 4.8b.

The transmission spectra of the AuNpA, immersed in a series of water and glycerol mixtures with varying refractive indices (ranging from 1.333 for pure water to 1.375 for a 33% glycerol solution), are presented in Figures 4.9a and 4.9b. A significant red shift was observed in the peak corresponding to the (1,0) Au/medium mode as the refractive index of the surrounding solution increased, with the (1,0) Au/medium mode sensitivity reaching 522.86 nm/RIU. As expected, the (1,0) Au/substrate mode was almost entirely suppressed, aligning well with the objectives of the targeted optical sensing application. Compared with recent publications on the bulk sensitivity of nanohole arrays, this work demonstrates comparable performance. For instance, Cetin et al. reported that nanohole arrays on a hybrid substrate exhibit a refractive index sensitivity as high as 671 nm/RIU [155]. Similarly, Zhang et al. achieved a notable refractive index sensitivity in gold nanohole arrays through scalable colloidal lithography [159]. Furthermore, Du et al. monitored two resonance modes around 750 and 810 nm, observing that both modes shift proportionally to longer wavelengths with refractive

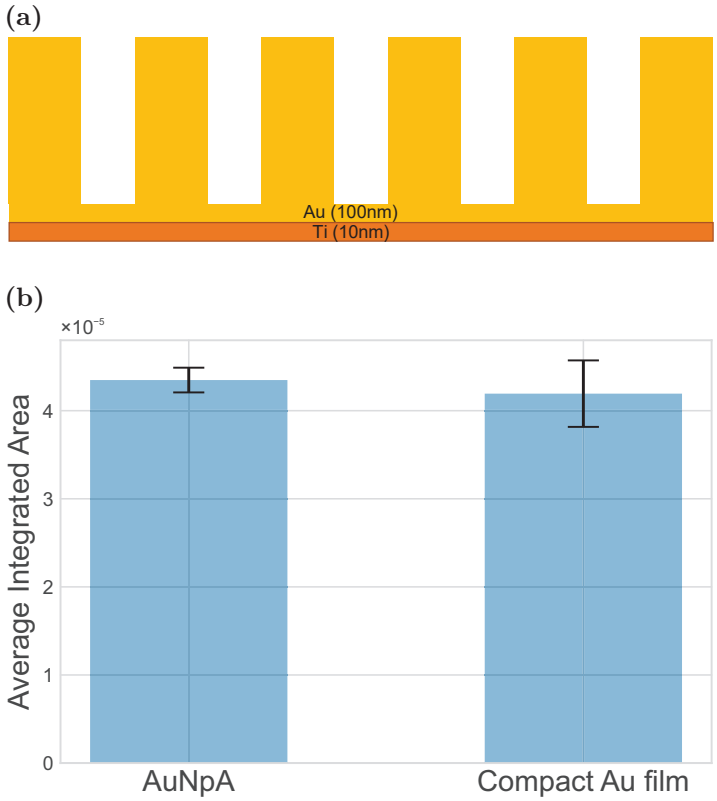

Figure 4.10: Schematic illustration of the ideal nanopit arrays (a), and experimental ESA comparison of the AuNpA and the compact AuFilm (b).

index sensitivities of 472 nm/RIU and 436 nm/RIU, respectively [151]. The sensitivity measurements in this work are comparable with these reported values, while the novel aspect of this work lies in the unique optimization of hole depth, which is being reported for the first time.

The incorporation of nanopit arrays into the design offered considerable advantages for electrochemical sensing by increasing the electrochemical surface area (ESA). When considering the ideal sidewall area of the nanopit arrays (as depicted in Figure 4.10a), the calculations showed that the ESA can increase by 32% or 36%, assuming pit depths of 80 nm or 90 nm, respectively, with a lattice constant of 600 nm and a hole diameter of 400 nm. This expansion from a 2D planar gold film to a 3D AuNpA structure not only enlarged the surface area but also raised the number of available receptor binding sites, thereby enhancing the likelihood of target molecule capture [160].

The ESA of the AuNpA and Compact AuFilm were determined by electrochemical treatment in 0.5 M fresh prepared H_2SO_4 from 0 to 1.3 V at a scan rate of 1 V/s until stable CV was recorded. The surface area of both samples was determined by integrating the current peak of

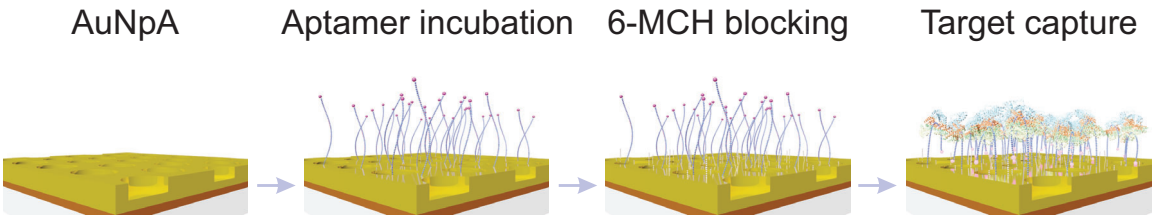

Figure 4.11: Schematic illustration of the working principle for HSA detection based on non-fully penetrating AuNpA.

the gold oxide reduction from the obtained CV curves. The ratio between the AuNpA and AuFilm was utilized for both theoretical and measured ESA to eliminate potential deviations. However, the experimental findings (presented in Figure 4.10b) suggest a more modest increase in the ESA of AuNpA, only about 1.04 times greater than that of a compact Au films (AuFilm). This disparity between theoretical calculations and experimental results could be ascribed to deviations from the idealized sidewall structure. This is supported by the cross-sectional FIB image of the AuNpA (Figure 4.7a), which indicates variations from the expected geometry. Given these observations, it's critical to recognize that the actual increase in ESA achieved by the 3D AuNpA might be considered marginal in many practical scenarios. Although the nanoscale architecture of AuNpA presents clear benefits for specific applications, the relatively minor enhancement in ESA should be carefully taken into account when evaluating the overall effectiveness and potential advantages of this configuration in electrochemical sensing applications.

4.1.5 Aptasensors performance for HSA

Human serum albumin (HSA) is a crucial biomarker for early disease diagnosis. Developing a accurate and quantitative method for HSA detection is very important. HSA aptamer was employed for detecting HSA due to its high specificity and affinity, robust chemical stability, and ease of synthesis and modification. The individual steps for constructing the developed aptasensor are depicted in Figure 4.11. The HSA aptamer was tethered onto the AuNpA through typical Au-S bonding forming a mixed SAM together with the 6-MCH, which severed as a blocking agent, and ferrocene (Fc) as a redox tag was employed for signal reporting after the conformation change.

The performance of the developed aptasensor fundamentally depended on the assembly of the receptor layer on the nanostructured electrode surface. Electrochemical impedance spectroscopy (EIS) was employed to monitor the biosensor fabrication process and the subsequent self-assembly steps, using 5 mM $[Fe(CN)_6]^{3-/4-}$ as an electrochemical redox probe, as depicted in Figure 4.12a. The impedance spectra obtained were analyzed by fitting them to a Randles

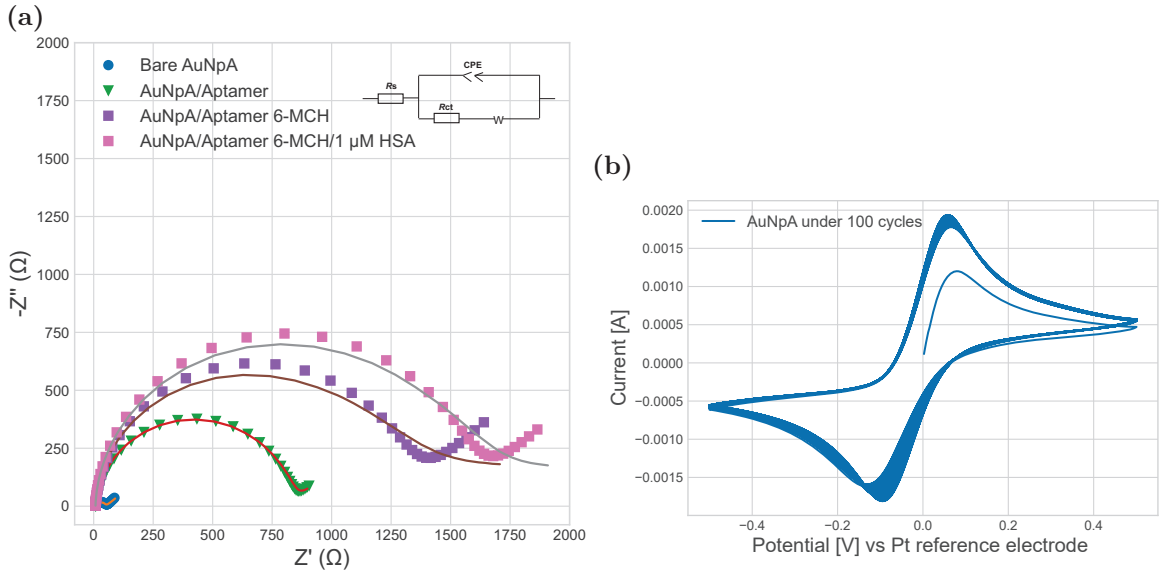

Figure 4.12: EIS recorded in 5 mM $[Fe(CN)_6]^{3-/4-}$ Tris buffer at bare AuNpA, AuNpA/Aptamer 6-MCH and adding 1 μM HSA. Solid lines are fitting results obtained with the model of the top right illustration. The electrical equivalent circuit elements used to fit the impedance measurements are shown in the equivalent Randles circuit and the equivalent circuit model used here comprises a resistor for the intrinsic electrolyte resistance (Rs) in series with a parallel constant phase element (CPE), a charge transfer resistance (Rct), and Warburg impedance (W) (a). Cyclic voltammetry (100 continuous cycles with scan rate 100 mV/s) in 5 mM $[Fe(CN)_6]^{3-/4-}$ Tris buffer using the bare AuNpA as working electrode (b).

equivalent circuit model. This model encompasses a series electrolyte resistance (Rs), a charge transfer resistance (Rct), and a constant phase element (CPE) to account for surface inhomogeneities of the electrode. Additionally, a Warburg impedance (W) was incorporated to represent the diffusion of the redox probes to the electrode surface. Initially, the bare AuNpA electrode exhibited a low charge transfer resistance of 43 Ω. This value significantly increased to 818 Ω and 1290 Ω following the immobilization of the aptamer and subsequent blocking with 6-MCH, respectively. This increase in impedance can be attributed to the blocking effect of the self-assembled monolayer (SAM) of the aptamer and 6-MCH on charge transfer processes. A further increase in Rct to 1550 Ω was observed after the introduction of 1 μM HSA, indicating effective binding between the aptamer and the target protein, which created steric hindrances that impeded charge transfer.

In addition, CV was conducted to study the redox behavior of 5 mM $[Fe(CN)_6]^{3-/4-}$ in Tris buffer solution, utilizing the bare AuNpA as the working electrode over 100 continuous cycles (Figure 4.12b). Notably, the current response displayed minimal variation across the cyclic voltammograms, underscoring the high stability of the electrode-electrolyte interface. This observation suggests that the bare AuNpA electrode proficiently supported electron transfer reactions while maintaining a consistent current response. For a detailed examination of the aptamer incubation concentration, incubation time, blocking molecule immobilization,

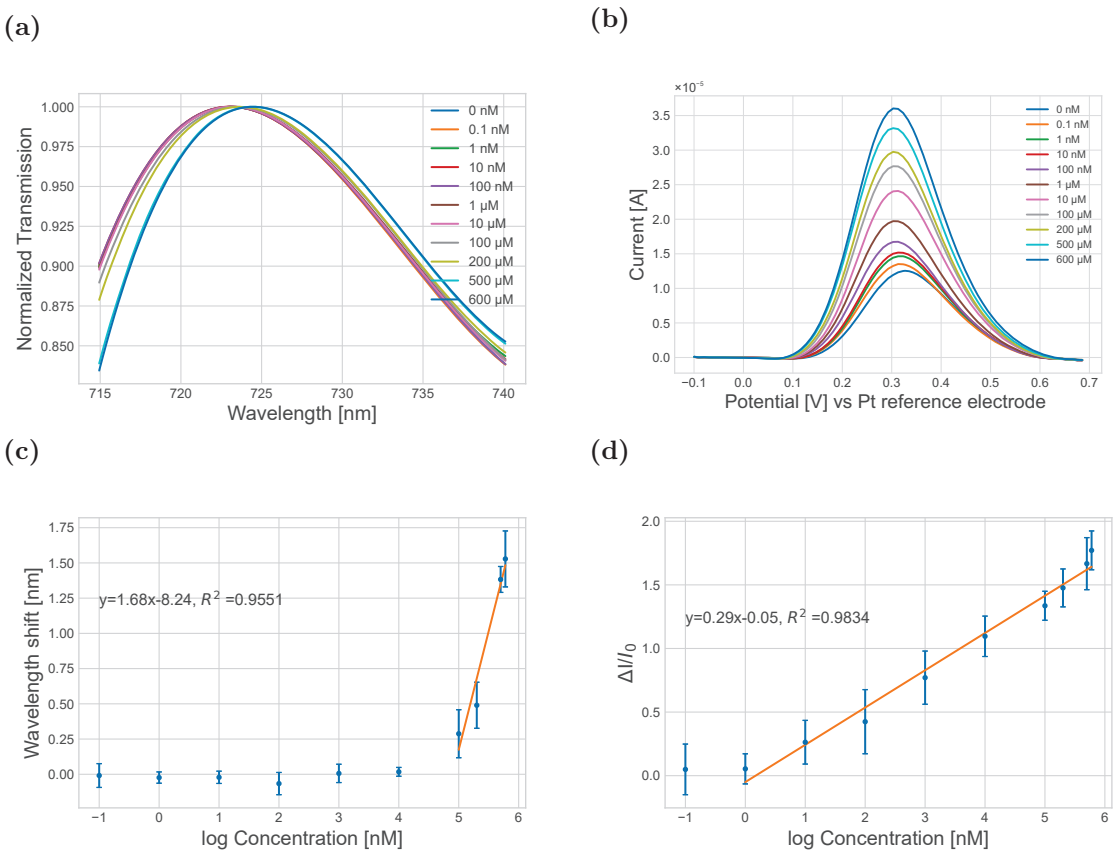

Figure 4.13: The binding of the HSA analyte caused a change in the aptamer conformation by which the Fc redox probe approaches the electrode surface and enhanced the charge transfer, fitting normalized transmission spectrum (a) and ACV current responses (b) of the aptasensor with different HSA concentrations from 0 to 600 μM, calibration curve of the sensor by plotting the optical shift (c) and current change (d) versus the logarithm of HSA concentration using 0 nM as a reference.

selectivity tests, and experiments in biological samples, readers are directed to Lei's earlier publication [122].

The binding of the aptamer receptor and the subsequent blocking with 6-MCH on the gold surface resulted in a red shift in the SPP peak, addition of the analyte to the prepared aptasensor led to a further shift in the SPP peak towards longer wavelengths as the concentration of HSA increased (Figure 4.13a), indicating the formation of aptamer-target protein complexes on the nanopit arrays. It is noteworthy that a relatively high concentration of the analyte is necessary to produce a substantial peak shift. A semi-logarithmic relationship between the peak position and the analyte concentration was observed within a range of 100 to 600 μM (Figure 4.13c). However, concentrations above 600 μM were not examined due to the solubility limit of the target in the used solvent. The limit of detection (LOD) was determined to be 95.22 μM, determined according to the International Union of Pure and Applied Chemistry definition (IUPAC, 1997) as $X_L = X_B + 3S_B$, where X_B is the average value of blank measurement, and

Table 4.3: Performance comparison of various strategies for HSA detection.

Method	Dynamic range of detection	Limit of detection	Reference
FET biosensors	1 fg/mL - 10 pg/mL	0.47 fg/mL	[162]
Fluorescence	6 μM - 338 μM	4 μM	[163]
Photoluminescence	75 nM - 100 μM	48 nM	[164]
Amperometric method	1 - 40 μM	0.6 μM	[165]
Naked eye / Smartphone camera by optical sensing	10 - 300 μM / 25 - 400 μM	5 μM / 5 μM	[166]
Plasmonic / Electrochemical aptasensor	100 - 600 μM / 0.1 nM - 600 μM	95.22 μM / 0.08 nM	This work

S_B is the standard deviation of the blank sample signal, and 3 is the numerical factor chosen according to the confidence level desired (95%) [161].

Additionally, ACV was employed for electrochemical characterization of the analyte binding at the same time. ACV helps in differentiating signals from the charging of the EDL and the Faradaic currents related to the redox probes. The conditions for signal recording were optimized to minimize charging currents. Upon addition of HSA, the aptamer/HSA binding complex formation triggered a conformational change, reducing the distance between the electro active Fc units and the AuNpA surface, thus enhancing electron transfer. An observable increase in the current peak was correspondingly observed with increasing HSA concentrations (Figure 4.13b). The signal gains in ACV measurements were calculated from the ratio of the current signal drop ($\Delta I = I - I_0$) to the background signal (I_0) as: signal gain (%) = $100 \times (I - I_0)/I_0$. The sensor displayed a semi-logarithmic concentration dependency over a broad range from 0.1 nM to 600 μM for the ACV signals (Figure 4.13d), with a LOD of 0.08 nM.

A comparative analysis with previous studies on quantitative HSA analysis is presented in Table 4.3. Relative to these detection methods, the dual signal-based AuNpA demonstrates broader dynamic detection ranges. Interestingly, the signals from both transducers exhibited distinct sensitivities. While the electrochemical transducer offers detection over a wide concentration range (approximately four orders of magnitude) with a lower sensitivity of 0.3/log C, the optical transducer provides higher sensitivity of 1.5/log C but is limited to high concentrations. Importantly, the physiological HSA concentration in healthy individuals' blood, which falls in the range of several hundred μM, can be effectively detected with our dual signal aptasensor [19].

The evaluation of the aptasensor's performance in complex matrices, such as human serum, is crucial for its practical application. The recovery experiments were performed here using a 100-fold dilution of human serum in Tris buffer (pH 7.4) by the standard addition method. The summary of both plasmonic and ACV signal responses in Table 4.4 showed recoveries of 95.30% and 83.07%, respectively, for 100 μM HSA concentrations. These high recovery rates suggested that the aptasensor was quite effective at detecting HSA in diluted human serum, a complex biological matrix. However, at 200 μM HSA concentration, the recoveries dropped to

Table 4.4: Results of the detection of HSA in human serum by standard addition method.

1% Human Serum	Spiked	Measured		Recovery		RSD	
Sample	uM	Plasmonic	Electrochemical	Plasmonic	Electrochemical	Plasmonic	Electrochemical
1	0	-	5.54	-	-	-	12.54%
2	100	100.58	87.67	95.30%	83.07%	12.76%	4.12%
3	200	177.15	163.95	86.19%	79.77%	28.38%	5.68%

86.19% and 79.7%. This decrease in recovery rate could be attributed to the limitations of 6-MCH as a blocking agent in preventing electrode fouling in such complex samples. Fouling can interfere with the sensor's ability to accurately detect and quantify the target molecule, leading to lower recovery rates. This issue is particularly relevant in blood samples, which contains a wide variety of substances that can adsorb onto the electrode surface and impede its performance [167].

Despite these challenges at higher concentrations, the overall high recovery rates at 100 μM HSA concentration suggested that the aptasensor maintains accuracy and reproducibility in complex biological matrices. This indicated its potential for practical applications, such as in medical diagnostics or biological research, where detecting and quantifying proteins in blood samples is often necessary. However, further optimization, particularly in improving the blocking efficiency of 6-MCH or exploring alternative blocking strategies, might enhance the sensor's performance at higher analyte concentrations in complex samples.

The re-usability of biosensors is indeed a critical factor in assessing their practicality and cost-effectiveness for widespread application. In this regard, the study by Hohertz et al. (2014) [168] offers valuable insights into the impact of different cleaning methods on the integrity and performance of nanohole arrays, which are integral components of many biosensor designs. The findings highlight that aggressive cleaning methods, such as using sulfochromic acid, piranha solution, and dry oxygen plasma, can cause irreversible modifications to the nanohole arrays. Such alterations include detrimental changes in the optical properties, diminished sensitivity, and shifts in the shape and position of the SPR peak. In contrast, a gentler approach using RCA1 (Radio Corporation of America Clean 1) etch followed by a brief immersion in dilute nitric acid (HNO_3(aq)) appears to be more effective. This method efficiently removes surface-bound alkanethiols while causing minimal harm to the gold nanostructures. This finding is crucial for biosensor design, as it suggests a viable method for cleaning and reusing nanohole array-based sensors without compromising their performance. The re-usability studies is one crucial aspect in advancing biosensor technology, aiming not only for high sensitivity and specificity but also for sustainability and cost-effectiveness. By addressing these aspects, significant contributions to the field of biosensing are anticipated, offering solutions that are both technically advanced and practically viable.

4.2 PEF-EC aptasensor based on AuNpA for the detection of S protein

Building on the findings from the initial study, a SPP wavelength shift detection was observed, while valuable, could not match the dynamic range offered by electrochemical methods. Nevertheless, to fully exploit the advantages of the EOT configuration and to further amplify the capabilities of plasmonic sensing, a strategy was adopted that take advantage of the intense electric fields generated at the interface between noble metals and the surrounding media during SPP excitation. This approach could significantly enhance the fluorescence of fluorophores located near the sample surface. The highly confined fields of surface plasmons (SP), which are collective oscillations of charge density and associated electromagnetic field on metallic surface, can be engineered to increase emitted fluorescence intensity and mitigate photo-bleaching to activate the plasmon-enhanced fluorescence (PEF). Such capabilities are desirable for detecting minute amounts of analytes with an improved detection limit.

Therefore, a novel approach of combining PEF-EC method was introduced to monitor the binding event between the SARS-CoV-2 S protein and the C7 aptamer receptor. This transition from HSA to the S protein is driven by the necessity to detect low concentrations of analytes, which is crucial in the context of COVID-19 but not as critical for HSA. Furthermore, the urgent need for COVID-19 research has underscored the importance of developing sensitive and specific detection methods. The COVID-19 outbreak has prompted a shift in research focus to address the immediate need for effective diagnostic tools capable of early and accurate detection of the virus. The sensing process was based on an EOT configuration using AuNpA, where plasmonic properties were exploited to enhance the fluorescence signal of methylene blue (MB), which was attached to the C7 aptamer. The MB was tagged to the C7 S protein aptamer (referred to as S2_20T_MB) which was tethered to the gold surface decorated with nanopit arrays. These AuNpA were designed such that the SPP peak overlapped with the excitation wavelength of the MB to enable strong coupling effects. In addition, AuNpA exhibited fringe structures fabricated through direct NIL processes. Surprisingly, these fringe structures can lead to even stronger PEF processes. To enable unambiguous sensor responses, the aptamer was immobilized to the gold surface via thiolated, partially complementary single stranded DNA (ssDNA) molecules (S1). S1 was capable of forming a stem-loop structure following the dissociation of the S2_20T_MB aptamer due to S protein binding and its release from the AuNpA surface. The monitoring surface-associated binding processes by two independent transducer systems may enhances the sensor performance and can provide a better understanding of physicochemical processes at the solid-liquid interface.

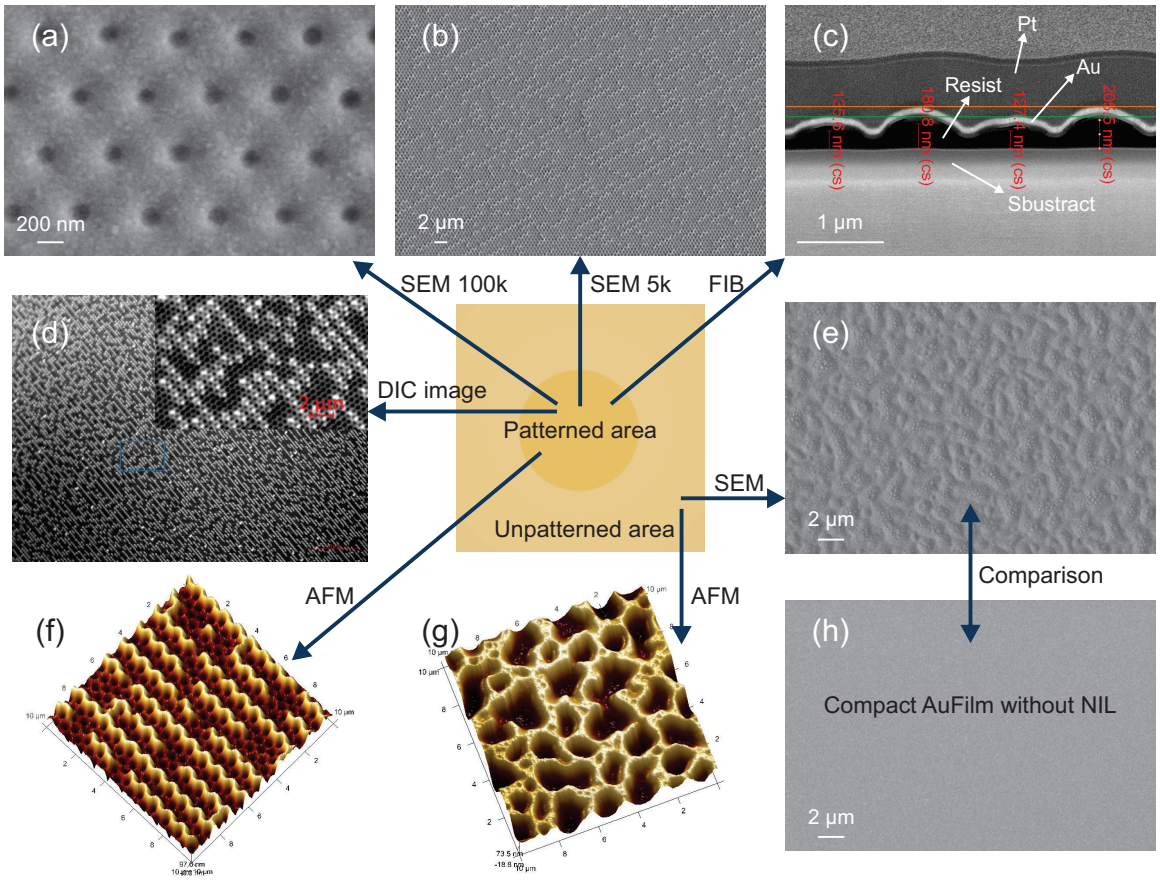

Figure 4.14: SEM images of the fabricated AuNpA at 100k magnification with scale bar of 200 nm (a) and at 5k magnification with scale bar of 2 μm (b), FIB cross-section image (c) and DIC image (d) of the AuNpA with fringe structure, SEM image of unpatterned area after NIL (e), AFM image of the AuNpA on patterned area (f) and unpatterned area (g), SEM image of AuFilm without NIL for comparison (h). The central sketch of AuNpA is placed for illustrative purpose.

4.2.1 AuNpA with fringe structures characterization

Similar to the SPP-EC system, the PEF-EC method also benefits the increased electrochemical surface area (ESA), not only enhances electrochemical performance but also supports the plasmonic effects, thereby improving the overall sensitivity and specificity of the biosensor. Therefore, the 3D AuNpA was selected as the substrate for both plasmon-enhanced fluorescence (PEF) and electrochemical (EC) transduction. The fabrication of AuNpA was improved by implementing a direct NIL process on the resist, as depicted in Figure 3.4. This approach serves as a more efficient alternative to the labor-intensive, Cr-based hard mask method. The nanoimprinted AuNpA sample demonstrated a hexagonal pit structure with an average diameter of 177 nm and a lattice constant of 501 nm, as observed in the SEM image (100k magnification, Figure 4.14a).

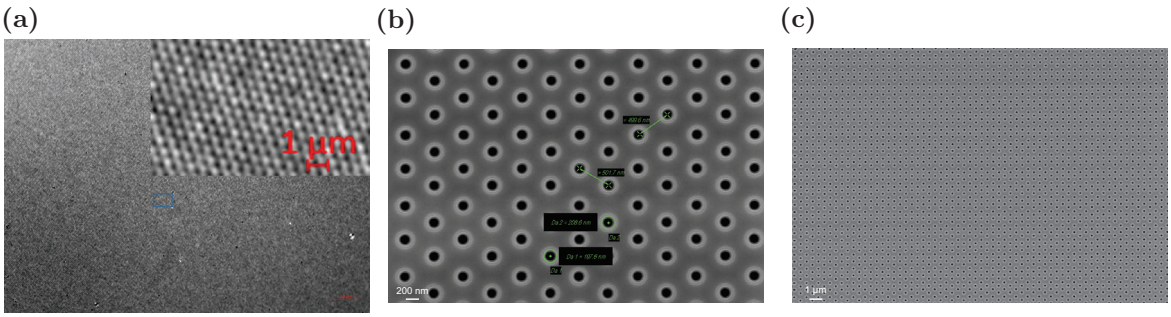

Figure 4.15: DIC image of AuNpA without fringe structures (lattice constant = 600 nm, a), SEM images of the master mold with high (b) and low (c) magnification.

Moreover, these unexpected fringe structures with distinct directionality were superimposed on the nanopit arrays at a larger scale (5k magnification, Figure 4.14b). To acquire a more detailed understanding of the morphology and characteristics of these fringe structures, AFM and FIB sectioning were employed (Figures 4.14f and 4.14c). The AFM analysis revealed fringe structures with an approximate height of 80 nm, while the pit arrays had a depth of about 50 nm. Cross-sectional views obtained through FIB imaging showed that these fringe structures were associated with variations in the thickness of the mr-NIL200 resist.

Differential interference contrast (DIC) images conducted from fluorescence microscopy also displayed these fringe structures, as shown in Figure 4.14d. In contrast, the DIC surface image of a sample from our previous work [12], featuring pit arrays with a lattice constant of 600 nm, appeared as uniform surface (Figure 4.15a). Interestingly, AFM and SEM investigations revealed that even the unpatterned regions of the AuNpA samples exhibited irregular surface corrugations (Figures 4.14g and 4.14e).

To find the origins of these unexpected fringe structures, a comparative analysis was undertaken using Au films (AuFilm) composed of the same layers (Quartz/mr-NIL200/Ti/Au) but without the application of the NIL process. The imprint-free resist/AuFilm, as shown in Figure 4.14h, displayed a markedly smoother surface compared to the area of nanoimprinted sample (Figure 4.14e). This observation indicates that the fringe structures observed did nor arise from the periodic distribution of stresses and strains [169].

Further examinations, including SEM images of the master mold (Figures 4.15 b and c) and AFM images of the Ormostamp working mold (Figure 4.16), were conducted. These investigation results revealed that, while the surface of the master mold was homogenous, the Ormostamp mold, utilized for the actual imprinting, exhibited some irregular structures that likely contributed to the fringe formation. This finding suggests that the fringe structures observed are a direct consequence of the NIL process. It is hypothesized that the additional fringe structure may arise from the intrinsic material characteristics of the Ormostamp resist

during the replica molding, in conjunction with the imprinting procedure, given the regularity of the pattern observed. Nevertheless, further research is essential to fully comprehend the underlying mechanisms and to develop approaches for either mitigating these fringe structures or utilizing them for potential technological applications.

4.2.2 Feasibility analysis of PEF

Based on the discussion in Equations 2.13 and 2.15, a critical inference can be made: the introduced new radiative decay rate, denoted as Γ_{m}, interacts competitively with the non-radiative decay rate Γ_{nr}. This interaction can result in either the enhancement or quenching of fluorescence. In the context of PEF, the proximity of the fluorophore to the metal surface is a critical factor. Optimal PEF distance is important when fluorophores are placed in close proximity to the metal surface, typically within the range of 5 to 20 nm. This proximity leads to an enhancement in quantum yield, a reduction in fluorescence lifetime, and an increase in photo-stability. This phenomenon can be conceptualized as the metallic nanostructure acting as an optical antenna, which effectively translates propagating electromagnetic radiation into near-field energy. It is essential to recognize that direct contact or extremely close proximity (less than 5 nm) to the metallic surface may lead to the quenching of the fluorophores [43, 59].

For the study, an important observation was that the peak of SPP was located around 666 nm, closely aligning with the excitation wavelength of the methylene blue (MB) fluorophore at 668 nm, as shown in Figure 4.17. The considerable overlap between the SPP peak and the MB excitation peak potentially leads to an amplified excitation rate of the fluorophore compared to its rate in free space.

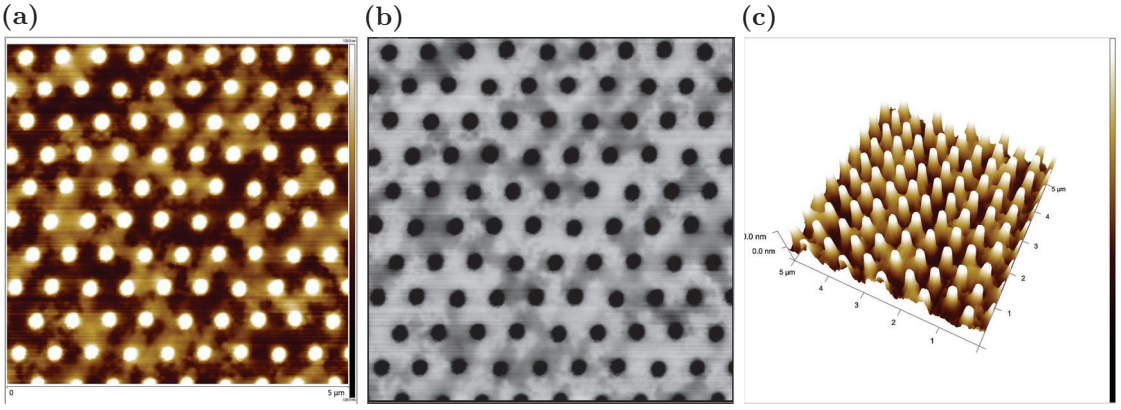

Figure 4.16: AFM measurement images of the flattened mode (a), binary mode (b), and 3D mode (c) for the Ormostamp working mold.

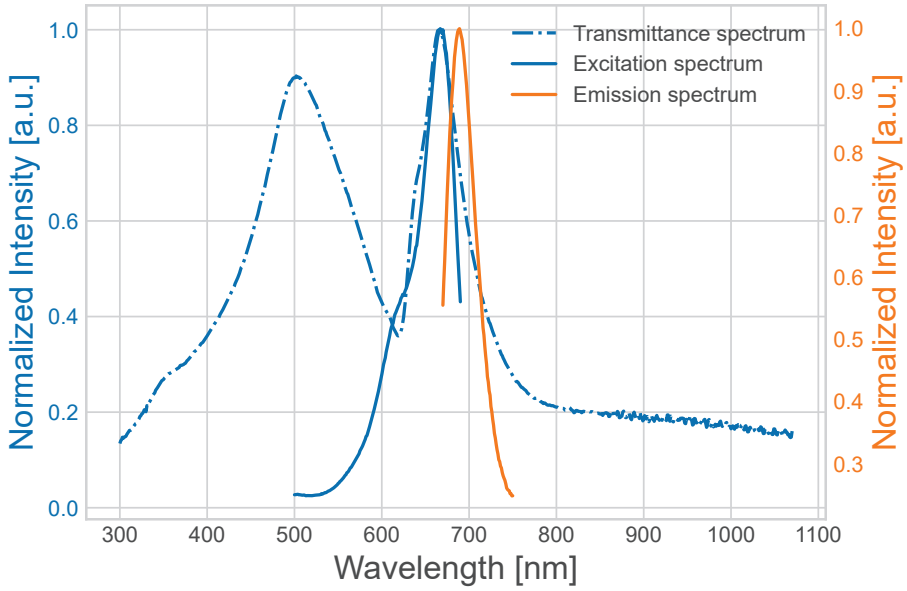

Figure 4.17: SPP transmittance (dashed blue line) spectrum of AuNpA, excitation (blue line), and emission spectrum (yellow line) of 1 μM S1/S2_20T_MB in Tris buffer.

This enhancement is attributed to the Förster Resonance Energy Transfer (FRET) at short distances (typically within about 5 nm) between the nanostructure and the fluorophore, and to the Purcell effect at greater distances (ranging from 10 to 50 nm). However, the Purcell effect related to plasmon radiation is generally of limited significance, as the local density of optical states (LDOS) at greater distances from the fluorophore is minimal.

Given the interplay between FRET and the Purcell effect, even minor distance variations within the length of surface-tethered aptamers (less than 15 nm) can significantly impact the enhancement of excitation. This characteristic offers a promising avenue for developing highly sensitive sensors capable of detecting subtle changes in the local environment near the electrode surface, a concept that is gaining attention in recent research [43,63,65].

Therefore, the determination of the optimal distance between metallic surfaces and fluorophores is important for effective sensor operation. The aptasensor from this work incorporates a two-strand oligonucleotide system. The first strand, S1, comprising 20 nucleotides, is engineered to form a stem-loop structure and is equipped with a dithiol group containing two thiol units, enhancing its binding affinity to the gold surface. The second strand, S2_MB, is complementary to S1, featuring a C7 S protein aptamer and a MB molecule serving as a fluorescence/redox probe, and spans 39 nucleotides in length. Additionally, a third strand was designed, akin to S2_MB, but extended with 20 thymine spacer, thus increasing its length to 59 nucleotides and denoted as S2_20T_MB. The integration of 20 thymine nucleotides aims to lengthen the

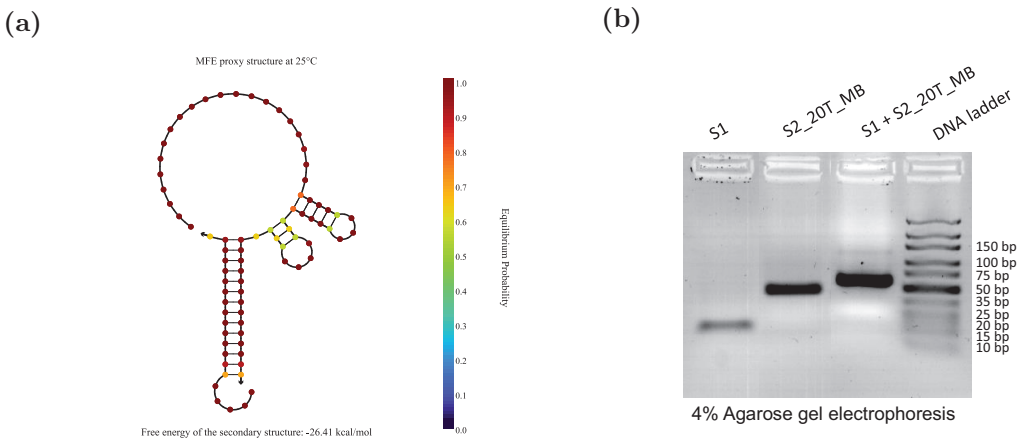

Figure 4.18: NUPACK simulation based on the S1 and S2_20T (a), gel electrophoresis with 3 lanes, represent S1, S2_20T_MB, and S1 + S2_20T_MB, respectively.

distance between the gold surface and the fluorophore. The thymine was chosen as spacer based on its relatively low affinity for gold surfaces compared to other nucleotides, following the order: $A > G \approx C \gg T$ [170, 171].

According to Lev et al., who employed spectral self-interference fluorescence microscopy to evaluate the conformation of coiled ssDNA and the average tilt of double-stranded DNA strands of different lengths, a 50-mer double-stranded DNA exhibited an estimated height of about 10.5 nm [172]. In the model, the maximal surface distance of the label was determined by the length of the double helix, roughly 20 nm for a 59-base pair structure, excluding DNA tilt considerations. However, factoring in the average tilt, the effective height is likely to be different. It is hypothesized that in a simplified model where the short stem-loop S1 strand acts as a rigid rod hinged to the surface, the average height of the distal label, assuming free rotation for half of its length, would exhibit an average tilt angle of 60° from the normal. It is noteworthy that free rotation might be limited due to steric hindrance from adjacent DNA molecules and surface interactions. Consequently, the distance between the fluorophore and the gold surface for the S1/S2_20T_MB configuration was estimated to be approximately 13 nm, a distance crucial to avoid quenching effects. For comparative purposes, the shorter S1/S2_MB configuration without the additional 20 thymines was estimated to have a proximity of around 9 nm to the gold surface.

The validation of the hybridization between the two oligonucleotide strands, S1 and S2_20T, was approached using both simulation and experimental techniques. NUPACK simulation (Figure 4.18a), a tool for analyzing nucleic acid secondary structures, thermodynamics, and kinetics, was employed to predict the hybridization efficiency of the S1 and S2_20T complex. The simulation results, exhibiting a calculated free energy of -26 kcal/mol, suggested a highly

favorable hybridization process. Additionally, the results detailed in Table 4.5 indicated a near-complete hybridization yield of 99.9%, highlighting the effectiveness and stability of the hybridization between these specific strands.

To corroborate these NUPACK simulation findings, experimental validation was performed using gel electrophoresis, a technique widely employed in molecular biology for the separation and analysis of macromolecules such as DNA and RNA. As depicted in Figure 4.18b, three distinct lanes were analyzed. Lane 1 contained only the S1 strand, serving as a control, while lane 2 included S2_20T_MB. Most importantly, lane 3 presented the mixture of S1 and S2_20T_MB, which had been allowed to incubate at room temperature for 2 hours in Tris buffer solution, promoting hybridization. The gel electrophoresis results were visually documented using the Bio-Rad ChemiDoc Imaging System. This system provided clear evidence of the hybridization process due to its precision and sensitivity in capturing images of gels. The distinct band observed in lane 3, characterized by its lower migration mobility compared to the individual strands in lanes 1 and 2, is indicative of the formation of long duplex structures. This band corresponds to the hybridized product of S1 and S2_20T_MB. The appearance of this band and its migration behavior relative to the unhybridized components confirmed the successful hybridization of the S1 and S2_20T strands.

Thus, the combination of NUPACK simulation and gel electrophoresis provided a robust approach to validate the hybridization efficiency and stability of the designed oligonucleotide strands, essential for the functionality of the aptasensor. In a coupled system involving plasmons, the fluorescence lifetime of a fluorophore is significantly altered due to the interaction with the plasmonic structure. The original lifetime τ_0 undergoes a change to τ, which can be mathematically described from Equation 2.14 to Equation 2.16 [58].

Herein, fluorescence lifetime imaging microscopy (FLIM) measurements were conducted to assess the kinetics of excited-state decay processes utilizing two-photon excitation at 925 nm. FLIM images and representative fluorescence decay curves with histograms of fluorescence lifetime were displayed in Figure 4.19. A detailed examination of the faint fluorescence signal from S1/S2_20T_MB in solution was estimated using a bi-exponential fitting approach. The fluorescence lifetime was determined to be 1530 ps (Figure 4.19a), markedly prolonged in comparison to the fluorescence lifetime of methylene blue (MB) in aqueous solutions

Table 4.5: Statistics of the complex and corresponding concentration from NUPACK simulation.

Complex name	Concentration (M)
S2_20T + S2_20T	1.34×10^{-14}
S1 + S2_20T	9.99×10^{-7}
S1 + S1	2.23×10^{-16}
S2_20T	8.17×10^{-10}
S1	8.17×10^{-10}

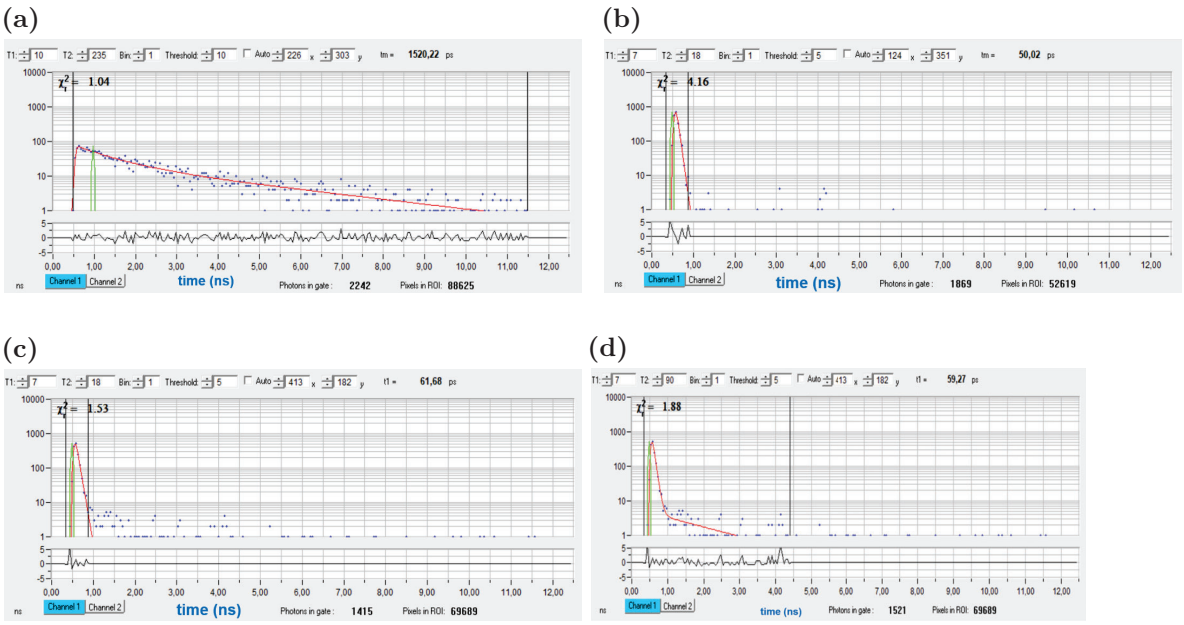

Figure 4.19: Fluorescence decay curve from a representative pixel of S1/S2_20T_MB in aqueous solution (λex = 925 nm) (a), S1/S2_20T_MB on AuNpA (λex = 925 nm) (b), S1/S2_20T_MB on Au film (λex = 925 nm) (c), and S1/S2_20T_MB on Au film with biexponential fit with dominating fast decay around 60 ps and a second slow decay of ca. 1500 ps (d, similar to S1/S2_20T_MB in aqueous solution).

(350 ps [173]) and within micelles (650 ps [174]). This prolongation suggested a notable interaction between MB and the aptamer. In contrast, the fluorescence characteristics of S1/S2_20T_MB on AuNpA were distinctly different (Figure 4.19b): Primarily, there was a substantial reduction in fluorescence lifetime, shortened to merely 53 ps, roughly 30-fold less than in solution. The potential contribution of any scattering components to this rapid fluorescence decay can be confidently excluded due to the minimal excitation intensity and the efficacy of the dichroic mirror in separating 925 nm excitation from MB fluorescence. Additionally, the fluorescence intensity was significantly enhanced (approximately 70-fold higher in Figure 4.19a compared to Figure 4.19b). The enhancement factor can be calculated due to variations in excitation power between the two images, indicated a substantial increase. The power adjustments were made to ensure roughly equivalent total photon counts in both measurements. Assuming an ideal two-photon absorption process, the enhancement would be considerably greater (approximately 5000 times, considering the quadratic dependence on excitation power).

However, due to the different experimental conditions (homogeneous solution versus a thin layer on AuNpA), precise quantification is challenging. Nonetheless, it was inferred that the enhancement of fluorescence intensity on AuNpA is within the range of 100 to 1000 times compared to in solution. Evidently, in the system, the parameter τ plays a critical role in reducing the fluorescence lifetime and enhancing fluorescence intensity. A comparative analysis

with FLIM experiments of S1/S2_20T_MB on an Au film revealed an "intermediate" behavior (Figure 4.19c). Here, the fluorescence lifetime was moderately increased compared to AuNpA as substrate, and the fluorescence intensity was significantly lower (61 ps, a 25-fold reduction in fluorescence lifetime; a fluorescence intensity enhancement of only 25 times). This lower enhancement in fluorescence intensity on the Au film was also evident in the fluorescence decay of S1/S2_20T_MB (Figure 4.19d), where a prolonged tail, indicative of a secondary decay component with a characteristic lifetime of approximately 1500 ps, was observed. This lifetime aligned closely with that of S1/S2_20T_MB in solution (Figure 4.19a), whereas such a tail was absent in the case of S1/S2_20T_MB on AuNpA (Figure 4.19b). The presence of this tail in the Au film case can be explained that the fluorescence intensity enhancement of S1/S2_20T_MB on the Au film is lower compared to AuNpA support, resulting in a minor detection of fluorescence (0.5%) from S1/S2_20T_MB in solution. Conversely, on AuNpA, the fluorescence intensity enhancement was so pronounced that fluorescence from S1/S2_20T_MB in solution became negligible.

4.2.3 Enhancement investigation by fluorescence microscopy

To further verify the PEF effect, a series of direct fluorescence microscopy experiments were conducted, systematically varying both the spatial locations and the substrates used. The fluorescence microscopy images, complemented by corresponding intensity histograms, provided a thorough elucidation of the optical properties. This analysis was specifically focused on areas of interest, including the interface between patterned AuNpA with adjacent unpatterned gold area, the pure plasmonic AuNpA region, and the AuFilm. The enhancement factor was determined in accordance with Equation 4.4 [175, 176]:

$$EF = \frac{I_{\mathrm{MB@AuNpA}} - I_{\mathrm{AuNpA}}}{I_{\mathrm{MB@AuFilm}} - I_{\mathrm{AuFilm}}} \tag{4.4}$$

Where $I_{\mathrm{MB@AuNpA}}$ is the measured fluorescence intensity of MB on the AuNpA substrate, and $I_{\mathrm{MB@AuFilm}}$ is the fluorescence intensity of MB on the reference substrate of the AuFilm. Additionally, I_{AuNpA} and I_{AuFilm} refer to the intrinsic background intensity of the respective substrates, AuNpA and AuFilm, in the absence of the fluorophore.

In the analysis of the edge region, the AuNpA and the adjacent gold areas exhibited distinctly different fluorescence characteristics. The surrounding gold areas demonstrated low fluorescence intensity, while the nanopatterned area, modified with S1/S2_20T_MB, showed higher intensity with pronounced local variations, as illustrated in Figure 4.20a. The corresponding intensity distribution plot, depicted in Figure 4.20b, revealed three distinct peaks.

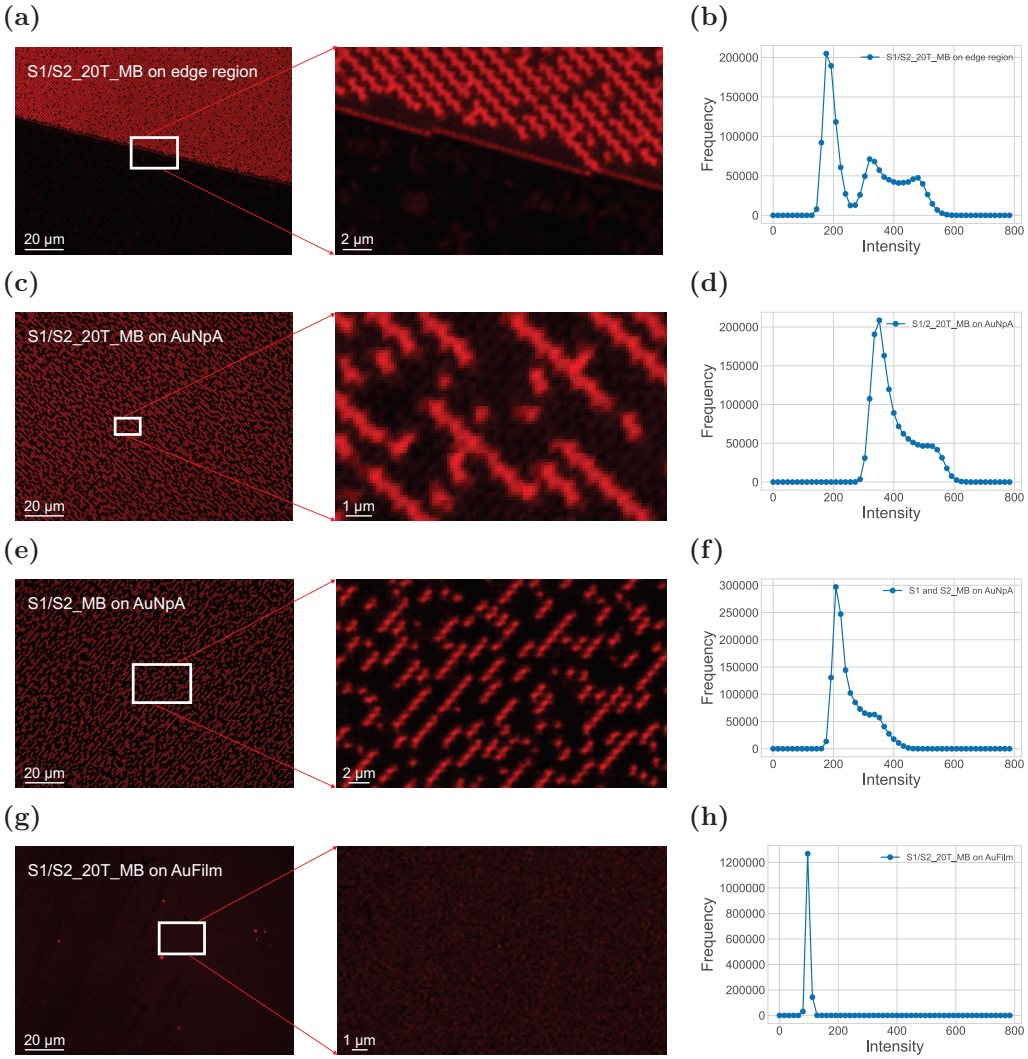

Figure 4.20: Fluorescence microscopy images (All the images are adjusted using best fit to optimize display ranges) and intensity histogram of AuNpA edge region with long S1/S2_20T_MB (a, b), AuNpA plasmonic area with long S1/S2_20T_MB (c, d), AuNpA plasmonic area with short S1/S2_MB (e, f), AuFilm with long S1/S2_MB (g, h).

These peaks were attributed to the unpatterned area, nanopit arrays, and fringe area, progressing from left to right, and each was characterized by different fluorescence intensity levels.

This interpretation was confirmed by Figures 4.20c and 4.20d, which presented a central surface treated with the same S1/S2_20T_MB modification, but excluding the unpatterned area. In the intensity distribution plot of this configuration, the peak corresponding to the low-intensity area was absent, whereas the peaks indicating higher intensity remained prominent.

Further investigation of the plasmonic fringe region, following modification with the shorter

DNA construct S1/S2_MB as shown in Figures 4.20e and 4.20f, revealed a comparable optical response, albeit with a reduced overall intensity in comparison to the longer S1/S2_20T_MB hybrid. This finding suggested that the distance of MB-Au between the fluorophore in the longer dsDNA construct and metal surface may position closer to the optimal PEF enhancement distance.

Lastly, the fluorescence microscopy study of the AuFilm following treatment with S1/S2_MB served as a reference, where only one background peak was observed in Figures 4.20g and 4.20h.

This fluorescence microscopy examination clearly indicated that a significant PEF effect was predominantly observed within the plasmonic area. Compared to the AuFilm without nanostructure, the average enhancement factor for MB in the S1/S2_20T_MB hybrid was determined to be 5.33 on the AuNpA and 7.60 for the fringe structures. In contrast, the intensity for the shorter S1/S2_MB configuration is only 61.9% of that observed for the S1/S2_20T_MB configuration.

However, various substrates have been used for PEF, each with different enhancement factors. For example, using a nanocrystal substrate can enhance Cy3/Cy5 fluorescence by 2 times [177], while AlexaFluor-647 on a gold nanohole array can achieve a 12-14 times enhancement [178], and a nanostructured silver film can provide a 300-fold enhancement for AlexaFluor 680 [179]. Determining the actual enhancement factor is challenging due to the lack of a reference substrate with the same architecture but without enhancement. Additionally, different fluorophores have different quantum yields, and there is evidence that fluorophores with lower quantum yields benefit the most from enhancement [32]. Nonetheless, it is intriguing to employ MB as a fluorophore and observe two different enhancements on one substrate. However, achieving a larger enhancement factor for MB will require further exploration of new nanostructures in future work.

In addition to the use of MB as a dual transduction probe, a separate combination of cyanine5.5 (Cy5.5) and ferrocene (Fc) was also experimented serving as the fluorescence and redox labels, respectively. These labels were conjugated to the S2_20T and S1 strands. Cyanine dyes, recognized as near-infrared (NIR) fluorophores (650-900 nm), are prevalently employed in bioimaging due to their expansive dynamic range, reduced background fluorescence, and enhanced sensitivity [180].

Upon examining the excitation (λ_{ex} = 687 nm) and emission (λ_{em} = 708 nm) spectra of S2_20T Cy5.5, an enhancement factor of 53 was observed, surpassing that of the AuFilm substrate, as depicted in Figure 4.21a. This enhancement significantly exceeds the one noted for MB.

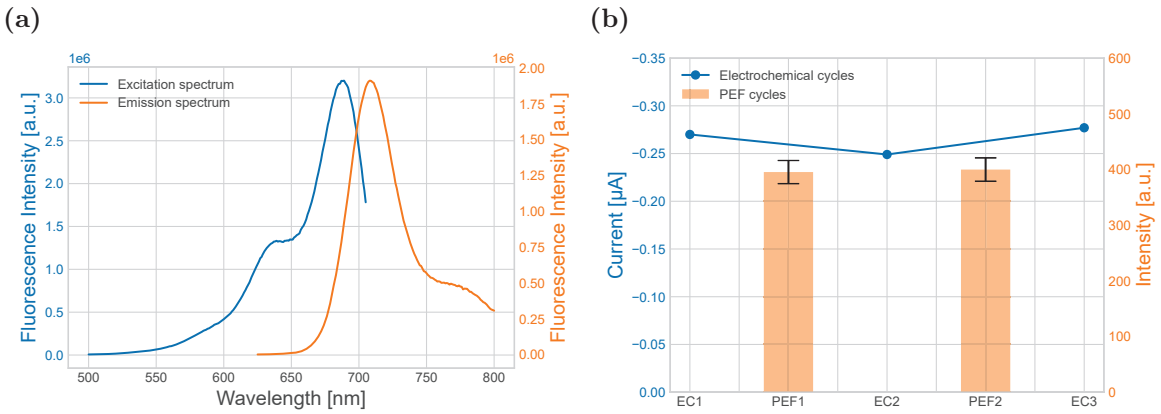

Figure 4.21: Excitation (blue line) and emission spectrum (yellow line) of 1 μM S1/S2_20T_Cy5.5 in Tris buffer (a), current and fluorescent signal change during the cycles between electrochemical scanning and PEF recording (b).

Nevertheless, a pronounced quenching in fluorescence intensity was detected during electrochemical scanning. In contrast, the use of MB as the dual transduction label, coupled with the potential cycling process illustrated in Figure 4.21b, did not exhibit any electrochemically induced quenching. Therefore, it becomes evident that employing MB as a singular dual transduction probe is more advantageous for the integrated PEF-EC sensing approach, rather than dividing the functionalities between two distinct probes: Cy5.5 for PEF sensing and Fc for electrochemical detection. The novel phenomenon of electrochemical quenching, which reported for the first time, was awaiting for further detailed exploration.

4.2.4 FDTD simulation of AFM and ideal models

Transmittance spectra were analyzed utilizing FDTD simulation, based on two distinct models: an idealized representation of nanopit arrays without distinct fringe features derived from software's geometric patterns, and a more realistic model imported from AFM measurement of actual sample containing these fringe structures, as illustrated in Figure 4.22. While there was a lack of perfect alignment between experimental and simulated spectra, the overall peak patterns demonstrated fundamental similarities. It is important to note that the AFM images are subject to imaging artifacts, particularly those arising from the superposition of feature topography and the tip shape. This can be discerned when contrasting FIB-SEM with AFM images, as shown in Figures 4.14c and f.

The simulation that incorporated AFM data were more accurately similar with the real experimental transmission curve compared to the idealized geometric model without fringe structures. This enhanced alignment can be ascribed to the incorporation of fringe struc-

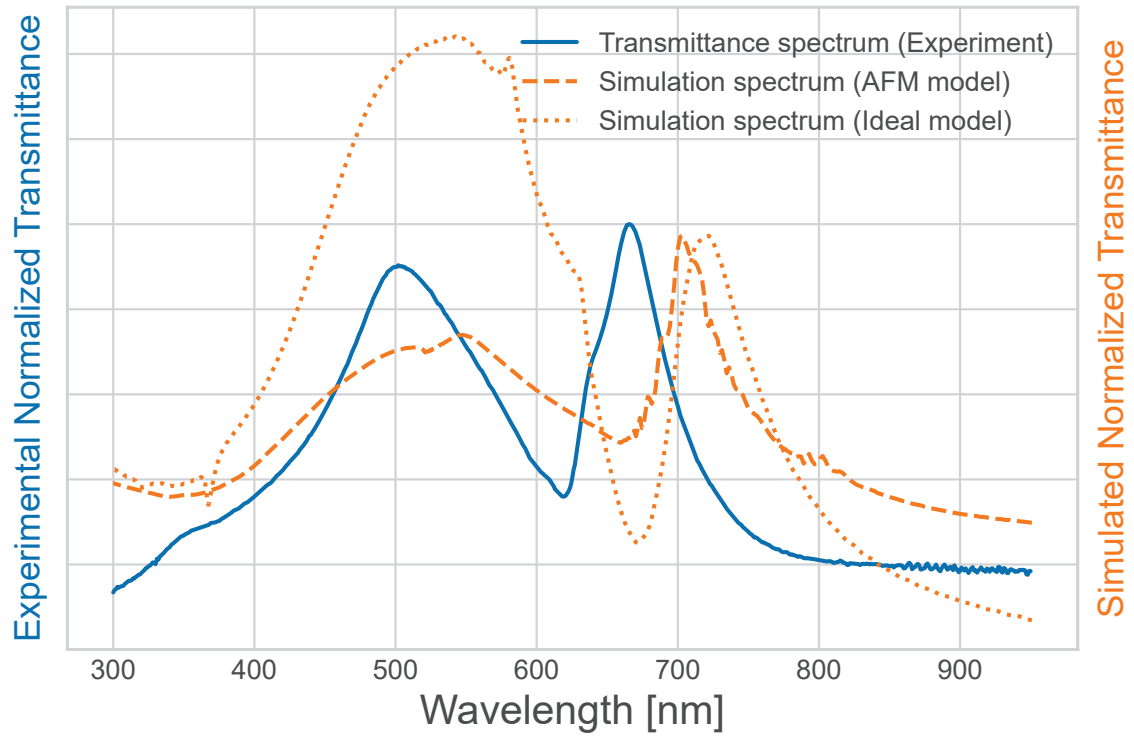

Figure 4.22: Real transmittance spectra of AuNpA and simulated transmittance from AFM and ideal models.

tures and associated surface roughness, offering a more realistic depiction of experimental conditions.

Differences in the enhancement factor between nanopit arrays and fringe structures may associated with the different amplification of the electric field. Further FDTD simulation investigation, based on the AFM model, were employed to examine the cross-sectional distribution of the electric field, as depicted in Figures 4.23a and 4.23b. The model revealed noticeable disparities in electric field distribution between higher fringe structures and pit arrays. Particularly, the cross-sectional asymmetry led to four distinct electric field decay channels, labeled as fringe 1, fringe 2, pit 1, and pit 2 (Figure 4.23a). Analysis of the z-component of the electric field distribution (Figure 4.23b) identified the maximum electric field enhancement (E/E_0) values as 5.3, 6.1, 4.6, and 5.4, with corresponding decay lengths of 177 nm, 176 nm, 252 nm, and 205 nm, respectively. The observed variations and asymmetries in both fringe and hole regions regarding electric field enhancement and decay length are crucial features of the PEF effect.

To explain the fluorescence enhancement at the fringe structures, two hypotheses are proposed. First, the pronounced fringe structures may serve as focusing elements, attributed to their greater distance from the surface relative to the overall pit arrays, similar to how plasmons

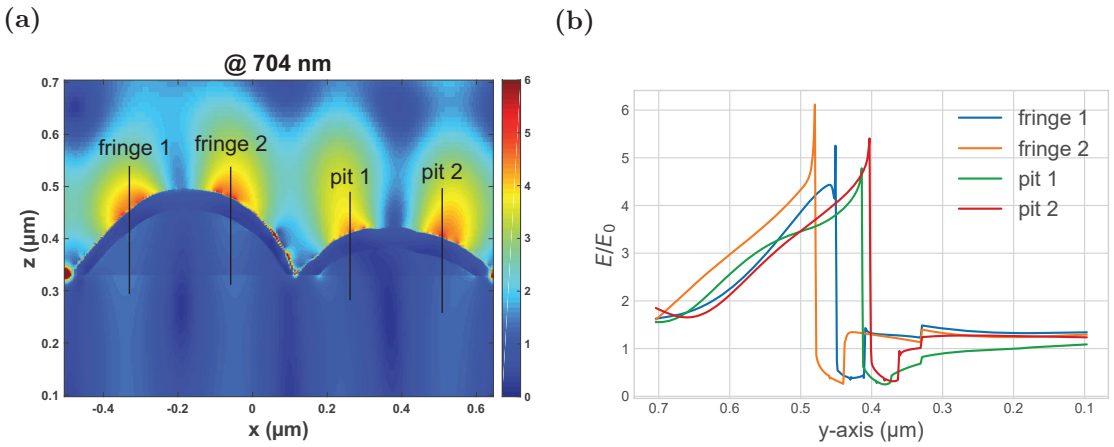

Figure 4.23: Cross-sectional electric field distribution for AFM imported surface model (a), and z-component of the electric field with four decay channels (b).

from two different zones "meet" each other [181,182]. Second, the variation in decay lengths, as determined through FDTD simulation, could lead to different optimal enhancement distances. It is conjectured that the S1/S2_20T MB constructs were positioned closer to the optimal optical enhancement distance within the fringe structures, thereby contributing significantly to the observed fluorescence enhancement phenomena.

4.2.5 QCM and SPR-M characterization

A comprehensive characterization of the sensor assembly process was conducted using a QCM equipped with a fluidics system including the stepwise immobilization of biomolecules on the electrode surface. This analytical approach facilitated the precise quantification of mass variations and energy dissipation dynamics occurring during the formation of a mixed SAM. This process involved the sequential immobilization of aptamer receptors, followed by backfilling with PEG molecules, serving as an alternative to 6-MCH. The mass alterations observed during this process were quantitatively analyzed employing the Sauerbrey equation [183]:

$$\Delta f = \frac{2f_0^2}{\mathrm{A}\sqrt{\rho_q \mu_q}} \Delta m \tag{4.5}$$

Where Δf is the frequency change, f_0^2 is the resonant frequency of the fundamental mode (Hz), A is the area of the piezoelectrically active crystal, ρ_q is the density of quartz (ρ_q = 2.648 g/cm^3), μ_q is the shear modulus of the quartz for AT-cut crystal ($\mu_q = 2.947{\times}10^{11}$ g/cm s^2), and Δm is the mass change.

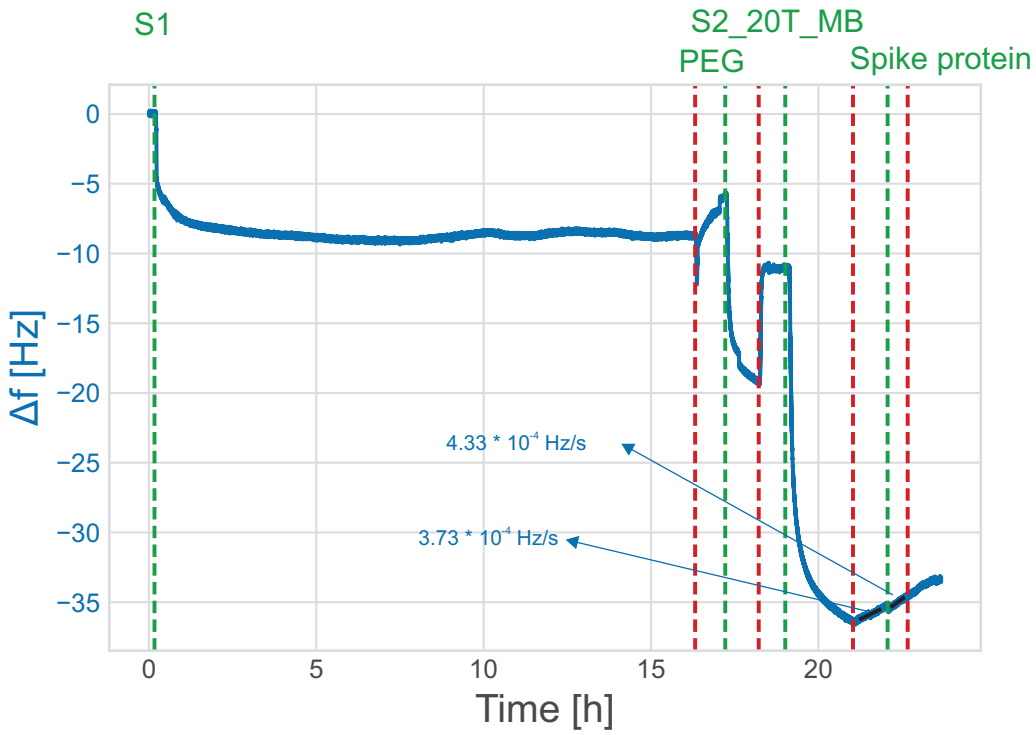

Figure 4.24: QCM plot for S1, PEG, S1/S2_20T_MB immobilization and S protein detection with frequency change. The incubation of molecule is denoted by the green dashed line, while the red dashed line indicates the rinsing process.

The QCM analysis revealed a direct correlation between the sensor's frequency shift and the mass increment resulting from molecular binding on the sensor surface, as illustrated in Figure 4.24. Initially, the introduction of a 1 μM solution of the S1 over the bare Au sensor, followed by rinsing with Tris buffer, led to a decrease in frequency (Δf) of 5.7 Hz. This frequency shift corresponded to the successful immobilization of the S1 onto the sensor surface. Subsequent incubation of the sensor with PEG molecules, aimed at blocking unoccupied sites, and a further rinse with Tris buffer resulted in an additional frequency shift of 5.2 Hz, indicating the binding of these molecules to the regions of the surface not previously occupied by the S1 receptors. The sensor's exposure to the S2_20T_MB and subsequent rinsing produced a more pronounced frequency shift of 25.6 Hz. This observation was critical, as it proved the successful hybridization of the S2_20T_MB with S1 on the Au sensor surface. Furthermore, the introduction of a 100 pg/mL concentration of the S protein, followed by rinsing, caused an increased frequency shift of 1.9 Hz. Additionally, a comparative analysis of the frequency slope before and after the introduction of the S protein exhibited a significant change. After the addition of S protein, the slope was measured at 4.33×10^{-4} Hz/s, a clear increase from the pre-addition slope of 3.73×10^{-4} Hz/s.

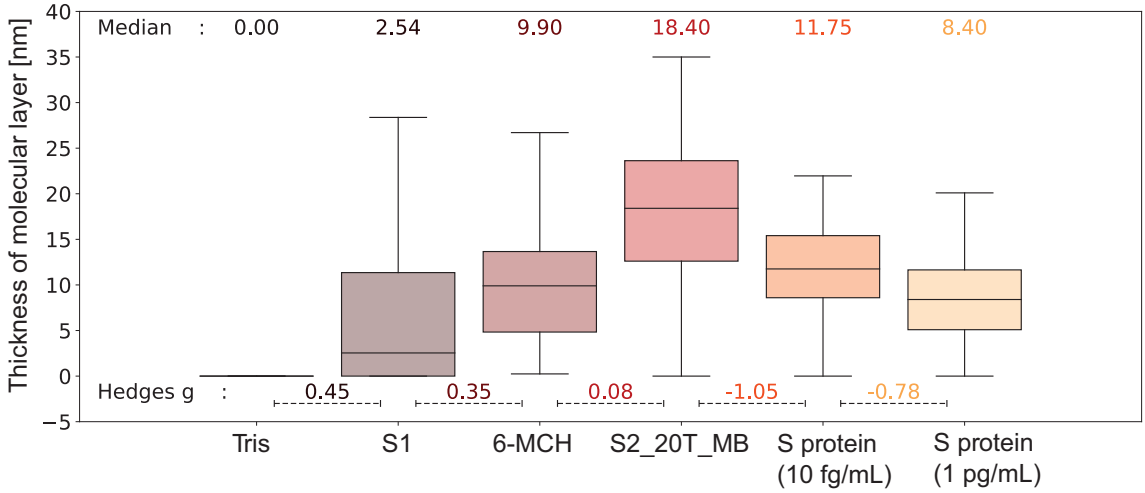

Figure 4.25: Thickness of molecular layer change in pixels by monitoring stepwise during various modifications including the bare Au surface as reference point, the S1 covered Au surface, the S1/6-MCH covered Au surface, the S1/6-MCH/S2_20T_MB aptasensor and finally with targets (10 fg/mL and 1 pg/mL S protein) were scanned in Tris buffer across five 20 × 20 μm^2 areas.

The observed increment in the frequency shift and frequency slope following the S protein introduction, indicating the occurrence of specific binding interactions between the S2_20T_MB and the S protein, leading to their detachment from the gold surface, thus validating the sensor's functionality in detecting the S protein.

To independently evaluate the mechanics of the aptasensor, surface plasmon resonance microscopy (SPR-M) was employed to characterize the recognition process of the target on bare Au surfaces. SPR-M, a localized variant of traditional SPR, allows for the detailed analysis of lateral structures and variations on a sample surface [144]. The SPR-M measurements encompassed several stages: a bare Au surface as the reference, the Au surface covered with S1, the Au surface modified with both S1 and 6-MCH, and finally exposed to two different concentrations of the S protein target (10 fg/mL and 1 pg/mL). Each stage was scanned in Tris buffer across five 20 × 20 μm^2 areas, using a 2 μm step width in both directions. Consistent with the AuNpA sample protocol, rinsing and incubation were performed between each step.

At every scanning point, the SPR angle was determined as the position of minimum reflectivity in the angle-reflectivity spectrum. Assuming normal distributions, mean values and standard deviations were calculated for each of the five sub-measurements in every step. These values are represented as individual data points in Figure 4.25. The box plot in the figure illustrated the thickness of the molecular layer across all scanning points for each measurement step. Hedges' g was employed to quantify the effect size of each modification between steps. As illustrated in Figure 4.25, an expected increase in molecular layer thickness was observed

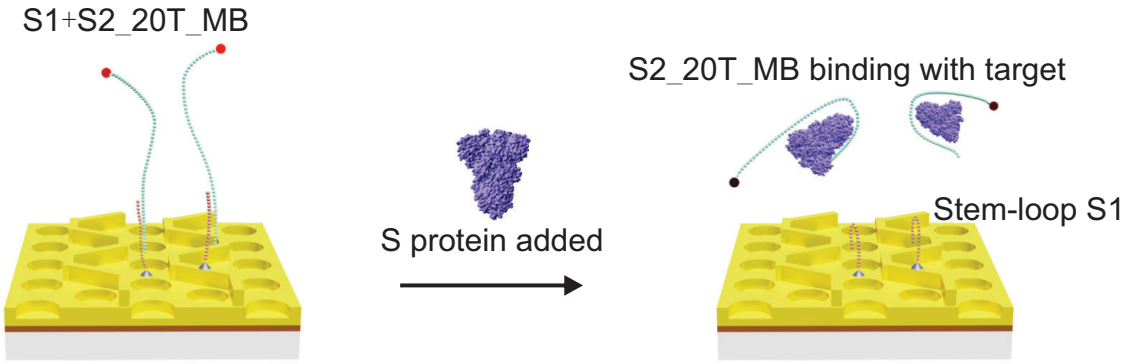

Figure 4.26: Schematic illustration of the working principle for SARS-CoV-2 S protein detection based on AuNpA as substrate.

following the addition of S1, 6-MCH, and S2_20T_MB. Notably, the median molecular layer thickness decreased significantly upon the addition of 10 fg/mL of S protein, dropping from 18.40 nm to 11.75 nm. A further decrease to 8.40 nm was observed with a higher S protein concentration (1 pg/mL). SPR-M has been widely used in single-virus and single-bacteria imaging, and live cell studies. The interaction between the aptamer and target is rarely reported [184, 185]. Here, the layer thickness of molecular layer was reported, providing compelling evidence for the interaction between the aptamer and the S protein. However, there are large distribution of data points, which may attribute to an area scan while the molecular layer in the scanned area is not perfectly homogeneous. This issue needs to be addressed in future research.

4.2.6 Aptasensor performance for SARS-CoV-2 S protein

To demonstrate the practical application of the S1/S2_20T_MB probe, the AuNpA substrate was employed for both PEF and EC signal monitoring of the S protein. This hybridized structure facilitates the detection of the target protein through a unique mechanism. Unlike donorâ€“quencher pairs such as fluorescent dyes, quantum dots, carbon-based materials, and metallic nanoparticles commonly employed in the design of molecular aptamer beacons, the approach leverages structure switching and specific recognition to yield an optical on/off switch in the presence of the target [186]. In this work, a simple hybridized molecular beacon was designed, and the optical signal is based on the distance change upon binding with the target, as depicted in Figure 4.26.

Upon binding with the S protein, the S2_20T_MB strand dissociated from its hybridization with S1 and detached from the gold surface. This detachment was supported by the conformational change in S1, which forms a stem-loop structure, further promoting the dissociation of the S2_20T_MB. The release of the MB labeled S2-strand into the bulk medium results in a

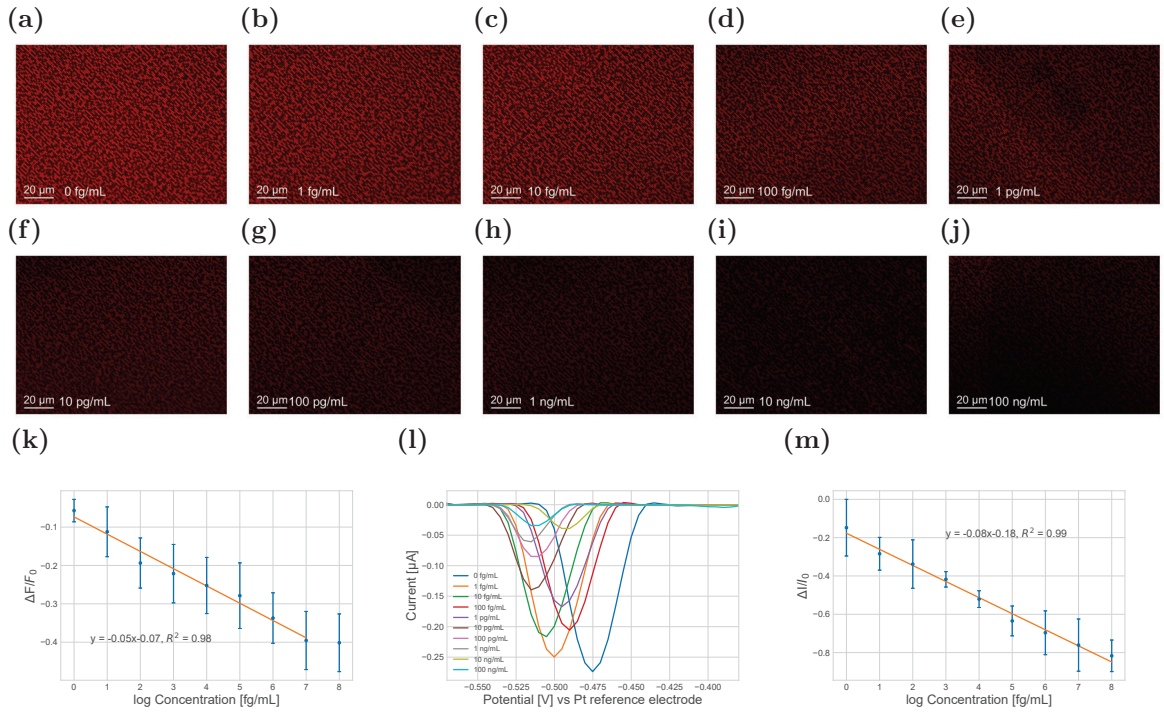

Figure 4.27: Fluorescence microscopy images of the aptasensor with different S protein concentrations from 0 to 100 ng/mL (a-j) and corresponding calibration curve (k), the SWV current responses (l) and current change calibration curve (m) versus the logarithm of different S protein concentrations from 0 to 100 ng/mL.

measurable decrease in both the redox current and the enhanced fluorescence, enabling the use of these changes as dual transducer sensor signals.

In the PEF transducer, a notable decrease was observed in the fluorescence signal, as shown in Figure 4.27a-j. The corresponding DIC images to these fluorescence changes were presented in Figure 4.28. The relationship between the overall fluorescence intensity and the S protein

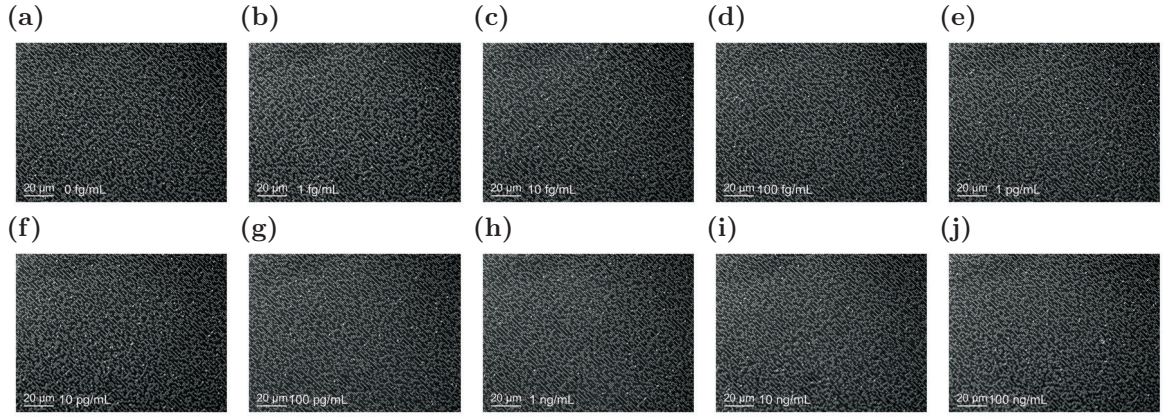

Figure 4.28: DIC images of the aptasensor with different S protein concentrations from 0 to 100 ng/mL

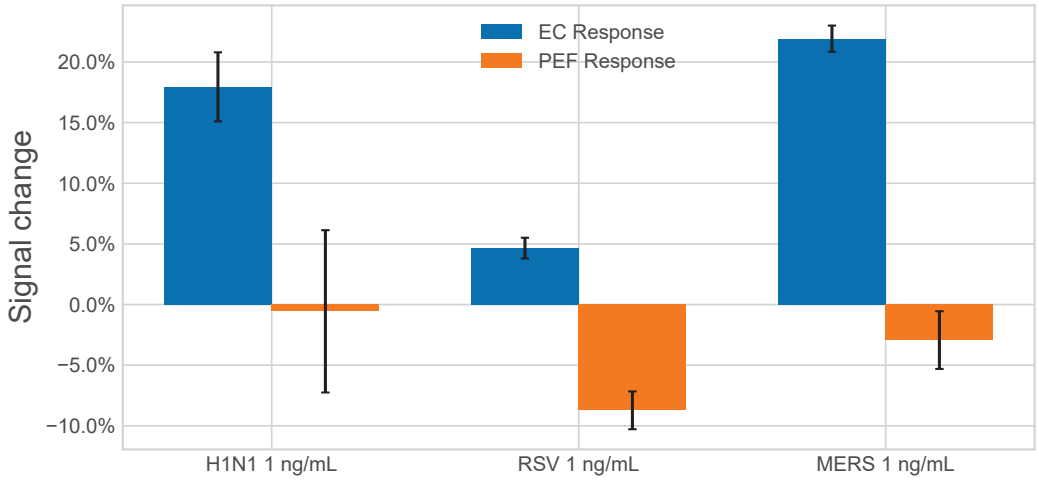

Figure 4.29: Selective experiments showing the detection using the analogous proteins, 1 ng/mL H1N1, 1 ng/mL RSV, and 1 ng/mL MERS in both EC and PEF measurements.

concentration was depicted in a semi-logarithmic calibration curve (Figure 4.27k), spanning a concentration range from 1 fg/mL to 10 ng/mL. The calibration formula derived is $\Delta F/F_0 =$ 0.05 lgC - 0.07, with a high correlation coefficient of 0.98 and a limit of detection (LOD) of 0.07 fg/mL.

For the electrochemical detection, SWV current responses decreased with the addition of the S protein (Figure 4.27l). Notably, there is stochastic potential shift, a phenomenon attributed to the use of a Pt-wire pseudo reference electrode in the combined PEF and EC setup as presented in Figure 4.27l. The $\Delta I/I_0$ response exhibited a semi-logarithmic dependence on the S protein concentration, with a broader range from 1 fg/mL to 100 ng/mL. The corresponding calibration curve, represented by $\Delta I/I_0 = 0.08$ lgC - 0.18, showed an correlation coefficient of 0.99 (Figure 4.27m), and a LOD of 0.15 fg/mL.

In summary, both the PEF and EC transducers, although reporting the same binding event and using the same MB-signal probe, displayed unique sensor characteristics. The PEF sensor demonstrated a lower detection threshold, whereas the EC sensor was characterized by a wider concentration range and higher sensitivity. The aptasensor characteristics in this work for PEF and EC transducers suggest promising avenues for future combination methods.

The selectivity of the aptasensors was rigorously evaluated by testing their response to biomarkers of various respiratory viruses, as depicted in Figure 4.29. The biomarkers tested alongside the SARS-CoV-2 S protein included the Hemagglutinin/HA1 protein of Influenza A H1N1, the glycoprotein G/RSV-G protein of human respiratory syncytial virus (RSV), and

the Spike protein of the Middle Eastern respiratory coronavirus (MERS). Each biomarker was tested at a concentration of 1 ng/mL. As a baseline for comparison, responses to the SARS-CoV-2 S protein at 1 ng/mL were -33.71% and -69.65% for the PEF and EC transducers, respectively. In contrast, the response to the Influenza A biomarker was significantly lower, at -0.56% and 17.95% for PEF and EC, respectively. Similarly, responses to the RSV biomarker were -8.72% and 4.65%, and for the MERS biomarker, they were -2.93% and 21.92%. These results clearly demonstrate that the PEF responses for all non-SARS-CoV-2 biomarkers were considerably weaker compared to the SARS-CoV-2 S protein.

Interestingly, the EC responses showed an inverse signal change, with increasing EC signals for non-target proteins. This phenomenon could be attributed to non-specific associations of these proteins with the aptamer, potentially altering the S1/S2_20T_MB hybrid conformation. Such interactions might reduce the distance between the redox probe and the electrode, leading to enhanced redox currents. Despite these interfering interactions, the distinction between non-specific, positive signal changes and specific, negative signal alterations due to S protein binding remains clear and unambiguous.

To evaluate the aptasensor's robustness in biological fluids, control experiments were conducted using a 10% human saliva matrix, following the standard addition method (Table 4.6). The recovery rates for the PEF transducer ranged from 102.3% to 128.3%, with relative standard deviations (RSD) between 2.0% and 17.7%. For the EC transducer, signal recovery varied from 100.2% to 110.7%, with RSD values ranging from 2.5% to 6.8%. These results indicate that the PEF-EC aptasensor maintains robust performance even in complex biological matrices.

The reproducibility was evaluated by freshly preparing three samples modified with the same S1/S2_20T_MB. All electrodes exhibited similar PEF and electrochemical responses, with RSD values of 8.43% and 15.81%, respectively, demonstrating satisfactory reproducibility of the proposed biosensor.

The stability of the biosensor was evaluated over a period of 3 days. Figure 4.30 illustrated the storage stability of the aptasensor after seating in Tris buffer at 4 °C. After 3 days, the PEF intensity remained largely unchanged, and the current intensity retained approximately 75% of its initial value. These results suggest taht the aptasensor is sufficiently stable for a single use detection. However, further optimization of the storing conditions need to be considered for long term storage.

The performance of the PEF-EC aptasensor in quantitatively analyzing the S protein is compared with previous studies, as detailed in Table 4.7. This comparison focuses on key analytical parameters, particularly the LOD and the linear range of the assay. The findings

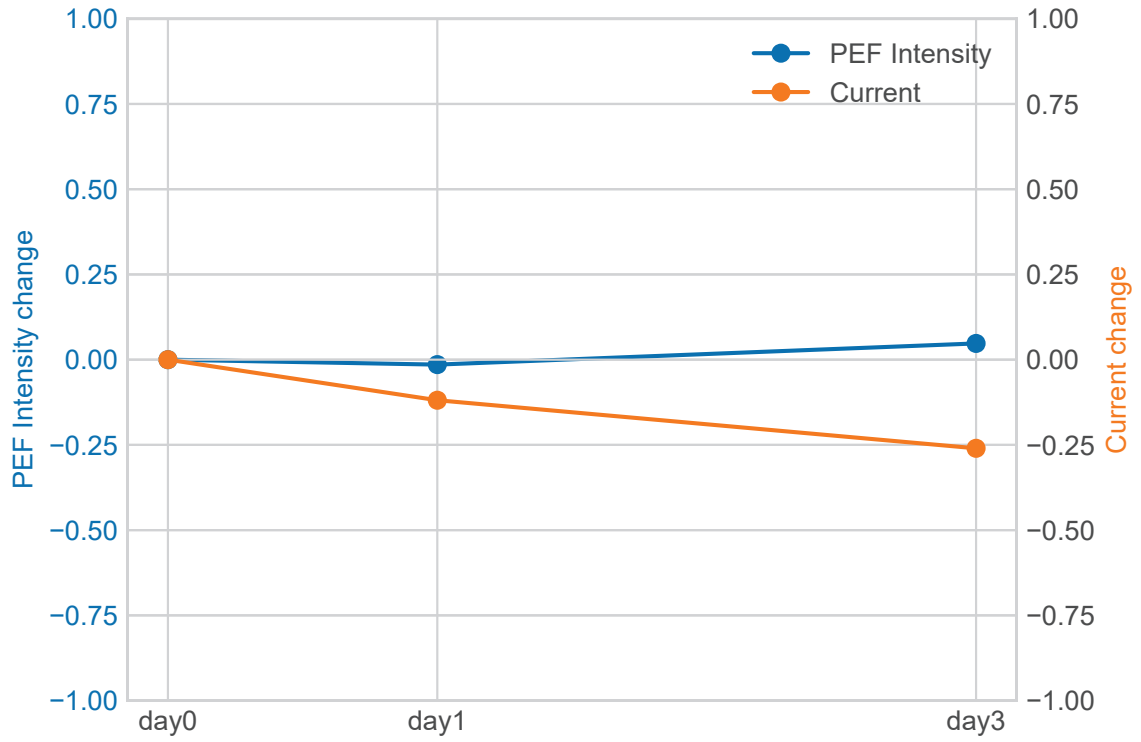

Figure 4.30: Stability of the biosensor. The fabricated biosensor was stored in Tris buffer at 4 °C for up to 3 days.

Table 4.6: Results of the detection of S protein in 10% saliva by standard addition method.

10% saliva	Spiked	Measured		Recovery		RSD	
Sample	fg/mL	PEF	Electrochemical	PEF	Electrochemical	PEF	Electrochemical
1	0	0.028	0.001	-	-	2.0%	6.8%
2	1	1.283	1.023	128.3%	102.3%	12.5%	6.4%
3	100	110.713	100.219	110.7%	100.2%	17.7%	2.5%

reveal that the aptasensor either matches or surpasses the performance of most existing methods reported in the literature.

The optical PEF transducer exhibited a similar LOD as the EC transducer, indicating that the utilization of the plasmons to enhance the fluorescence leads to improved sensor performances with lower LOD and wider concentration ranges than SPP wavelength shift. This difference may be attributed to the surface confinement of the PEF, which is sensitive to minute changes of the fluorophore/substrate distance as a trade-off between FRET/quenching/Purcell effects with an optimal distance from the surface in the range of 10-15 nm [192]. Presumably, for the longer S1/S2_20T_MB conjugate, which is approximately 13 nm in length, the fluorophore is located at an optimal enhancement distance, while the shorter S1/S2_MB configuration (around 9 nm) without the additional 20 thymines, remains slightly below this optimal enhancement

Table 4.7: Performance comparison of various strategies for S protein detection.

Method	Dynamic range of detection	Limit of detection	Reference
Electrochemical immunosensor	0.25 fg/mL - 1 μg/mL	0.04 fg/mL	[187]
FET biosensor	0.1 fg/mL - 100 ng/mL	0.025 fg/mL	[188]
OFET biosensor	0.1 fg/mL - 1 μg/mL	0.36 fg/mL	[189]
Surface plasmon resonance biosensor	5 fg/mL - 150 ng/mL	13.25 fg/mL	[190]
Surface-enhanced raman scattering-based biosensor	1 fg/mL - 1 ng/mL	0.77 fg/mL	[191]
PEF / EC aptasensor	1 fg/mL - 10 ng/mL / 1 fg/mL - 100 ng/mL	0.07 fg/mL / 0.15 fg/mL	This work

range. In contrast, the SPP wavelength shift based sensor probes the entire attenuation length of the surface plasmon at the metal/liquid interface based on the overall refractive index change. As the refractive index of the DNA (n = 1.58 [193]) is similar with that of the proteins (e.g., bovine serum albumin with n = 1.60 [194]), the resultant signal generally may be less pronounced. Consequently, the EOT of periodic nanostructure arrays can be harnessed either by implementing easy to construct and operate but less sensitive sensor concepts, recording the peak shift of the transmitted light or by utilizing PEF, which facilitates low detection limits and wide detection ranges. In either case, the nanopit array facilitates complementary electrochemical and optical recordings to achieve reliable and redundant sensor signals.

5 Summary and Outlook

In conclusion, the research work of this thesis presents an advancement in the field of biosensing through the development and optimization of dual-transducer aptasensors for the detection of the HSA and SARS-CoV-2 S protein. By combining the surface plasmon resonance (SPR) and the electrochemical (EC) based transducers, the study utilize their complementary abilities to monitor processes at the solid-liquid interface with different information depths. The employment of AuNpA as substrate further enhances the dual-mode sensing capabilities, contributing to improved sensitivity and specificity in biosensing applications.

The first aspect of this study focuses on optimizing the grating Au nanostructures by utilizing FDTD simulations and later compared the simulation results with real experimental data. It was found that optical sensing with conventional fully penetrating hole geometries often suffers from the overlap of two EOT resonances originating from the Au/substrate and the Au/medium interfaces, which impairs the unambiguous determination of the analyte-associated peak shifts. Hence, nanohole arrays are not ideal for biosensor applications requiring reliable and accurate identification of spectral shifts. In response, eliminating the resonance of the (1,0) Au/substrate mode was proposed by introducing nanopit arrays with depressions that do not fully penetrate the metal film and leave a continuous Au film at the Au/substrate interface. The resulting AuNpA not only demonstrates sharper plasmonic spectral width and improved refractive index sensitivity but also expands the electrochemical surface area (ESA), enabling a wide concentration range (1 nM to 600 μM) for electrochemical detection. The plasmonic detection, ranging from 100 to 600 μM with high sensitivity, complements the electrochemical measurements, providing redundancy and enhancing the reliability of the aptasensor.

On the other hand, following up the initial investigation, which a SPP wavelength shift detection could not match the dynamic range offered by electrochemical methods, the second section of the study concentrates on simple and direct NIL fabrication of AuNpA with fringe structures and taking the advantages of the EOT configuration and PEF effect, which is sensitive to minute changes of the fluorophore/substrate distance to further amplify the capabilities of plasmonic sensing. This innovative approach leads to a enhancement factor of 5.33 and 7.60 for pit arrays and fringe structures in the PEF effect, respectively. As

demonstrated by a strong overlap between SPP peaks and the excitation peak of methylene blue (MB). The resulting aptasensor, specifically designed for the detection of the SARS-CoV-2 S protein, exhibits a low LOD (0.07 fg/mL for PEF and 0.15 fg/mL for EC). The aptasensor's robustness in real-world applications, particularly in saliva matrices, emphasizes its potential for widespread diagnostic use.

In summary, this dual-mode aptasensors present a multifaceted and sensitive approach to biosensing using AuNpA as substrate. The studies not only contributes to the advancement of combination biosensing detection technology but also opens new possibilities for broader applications in clinical and point-of-care testing scenarios. Specifically, the integration of plasmonic and electrochemical transduction methods, coupled with the unique EOT configuration, minimizes the experimental setup, and permits plasmonic (SPP wavelength shift and PEF effect) together with electrochemical detection. This achievement addresses the core objectives defined at the outset of this work, which aimed to develop a versatile biosensing platform capable of detecting a wide dynamic range of analytes with high sensitivity and accuracy. The integration of plasmonic and electrochemical transduction methods, coupled with the versatility of the proposed fabrication techniques, positions this aptasensor as a promising tool for early and accurate diagnosis, heralding a new era in biosensor development.

In the future, the field of biosensing is expected to experience even more remarkable advancements. The dual-transducer aptasensor will serve as a pioneering foundation by combining of plasmonic and electrochemical transduction methods, and researchers are likely to explore and expand upon this synergy in various applications. One avenue for exploration is plasmon-enhanced electrochemical detection, where the coupling of plasmonic effects with electrochemical processes could lead to improved sensitivity and selectivity, particularly in the context of hydrogen peroxide reduction reactions with enzymes, holds promise for applications ranging from medical diagnostics to environmental monitoring. The synergistic effects of plasmons and electrochemistry may also find utility in plasmon-enhanced photoelectrochemical biosensors, offering enhanced performance in terms of both intensity and sensitivity. Furthermore, the combining method can also be extended to plasmon-enhanced electrochemiluminescence (ECL) through the improvement of electrocatalytic activity, electromagnetic field enhancement, presenting a novel avenue for ultrasensitive detection. The investigation of new nanostructures, such as nanoslit arrays, is likely to be a focal point. These structures can be easily fabricated as nanoscopic multielectrode arrays (MEA), which could offer unique plasmonic and electrochemical properties, paving the way for aptasensors with even greater versatility and specificity.

6 Appendix

Python example script using a third-order polynomial function to fit the SPP peak

```
import matplotlib.pyplot as plt
import numpy as np
import pandas as pd
import os
from sklearn.linear_model import LinearRegression
from sklearn.preprocessing import PolynomialFeatures
from matplotlib.backends.backend_pdf import PdfPages
from matplotlib import rc
rc("pdf", fonttype=42)

# Set seaborn-whitegrid theme style
plt.style.use("seaborn-whitegrid")
resolution_value = 800

# Get working directory
scriptname = ("Wavelegth_shift_polynomial_regression.py")
abspath = os.path.abspath(scriptname)
dirname = os.path.dirname(abspath)
os.chdir(dirname)
print(os.getcwd())

# Define the Result directory to be created
path = abspath
try:
    os.makedirs("Results")
except:
    pass

# Define concentration & fitting wavelength range
concentration = ["0nM", "0.1nM", "1nM", "10nM", "100nM", "1000nM", "
    10000nM", "100000nM", "200000nM", "500000nM", "600000nM"]
```

```
Mconcentration = np.array([0.1, 1, 10, 100, 1000, 10000, 100000,
    200000, 500000, 600000])
Wmin = 714.9368896
Wmax = 740.1022339

# Get Quartz Tris Transmission
os.chdir("./Quartz Tris")
datalist = os.listdir()
for i in datalist:
    eachdata = pd.read_csv(i, header=None, sep=";", skiprows=1235,
    nrows=2433)
    tdataframe = pd.DataFrame(eachdata)
    if i == datalist[0]:
        tsum_secondcolumn = tdataframe[1]
    else:
        tsum_secondcolumn = tsum_secondcolumn + tdataframe[1]
    os.chdir("..")
qtdataframe = pd.DataFrame({"Waveleghth": eachdata[0], "Intensity":
    tsum_secondcolumn/len(datalist)})
qtdataframe.plot(x="Waveleghth", y="Intensity", xlabel="Wavelength [nm
    ]", ylabel="Transmission",
style=".-", figsize=(6, 4))
os.chdir("./Results/")
plt.legend(["Quartz Tris Transmission"], framealpha=0)
plt.savefig("Quartz Tris Transmission.png", dpi=resolution_value,
    bbox_inches="tight")
plt.show()
os.chdir("..")

# Get and plot average dataframe list data of different concentration
mdataframe = []
count = 0
for i in range(0, len(concentration)):
    alldatalist = []
    os.chdir(f"./{concentration[i]}")
    alldatalist = os.listdir()
    for j in alldatalist:
        meachdata = pd.read_csv(j, header=None, sep=";", skiprows
    =1235, nrows=2433)
        tedataframe = pd.DataFrame(meachdata)
        if j == alldatalist[0]:
            tesum_secondcolumn = tedataframe[1]
        else:
            tesum_secondcolumn = tesum_secondcolumn + tedataframe[1]
```

```
69          os.chdir("..")
70      t_df = pd.DataFrame({"Waveleghth": eachdata[0], "Intensity":
    tesum_secondcolumn/len(alldatalist)/qtdataframe["Intensity"]})
71      t_df.plot(x=0, y=1, xlabel="Wavelength [nm]", ylabel="Transmission
    ", style=".-", figsize=(6, 4))
72      plt.legend([f"{concentration[count]}"], framealpha=0)
73      os.chdir("./Results/")
74      plt.savefig(f"{concentration[count]}.png", dpi=resolution_value,
    bbox_inches="tight")
75      plt.show()
76      count += 1
77      mdataframe.append(t_df)
78      os.chdir("..")
79
80  # Polynomial regression of SPP peak of each concentration
81  count = 0
82  fitdflist = []
83  MaxWlist = []
84  MaxTlist = []
85  for i in range(0, len(mdataframe)):
86      xydf = mdataframe[i].loc[(mdataframe[0]["Waveleghth"] >= Wmin) & (
    mdataframe[0]["Waveleghth"] <= Wmax)]
87      x = xydf["Waveleghth"]
88      y = xydf["Intensity"]
89      train_x = x
90      train_y = y
91      plt.plot(train_x, train_y, "o")
92      polyModel = PolynomialFeatures(degree=3)
93      xpol = polyModel.fit_transform(train_x.values.reshape(-1, 1))
94      preg = polyModel.fit(xpol, train_y)
95      liniearModel = LinearRegression(fit_intercept=True)
96      liniearModel.fit(xpol, train_y[:, np.newaxis])
97      polyfit = liniearModel.predict(preg.fit_transform(train_x.values.
    reshape(-1, 1)))
98      xfit = train_x.reset_index(drop=True)
99      yfit = pd.Series(np.ndarray.flatten(polyfit))
100     fitdflist.append(pd.DataFrame({"xfit": xfit, "yfit": yfit}))
101     MaxWlist.append(xfit[yfit.idxmax()])
102     MaxTlist.append(max(yfit))
103     os.chdir("./Results/")
104     plt.scatter(train_x, train_y)
105     plt.plot(train_x, polyfit)
106     plt.legend([f"{concentration[count]}"], framealpha=0)
107     plt.xlabel("Wavelength [nm]")
```

```
108     plt.ylabel("Transmission")
109     plt.savefig(f"{concentration[count]}_fit.png", dpi=
    resolution_value, bbox_inches="tight")
110     count += 1
111     plt.show()
112     os.chdir("..")
113 
114 # Plot combined fitted Wavelength Shift-Transmission images
115 normalize_concentration = ["0 nM", "0.1 nM", "1 nM", "10 nM", "100 nM"
    , "1 \u03BCM", "10 \u03BCM", "100 \u03BCM", "200 \u03BCM", "500 \
    u03BCM", "600 \u03BCM"]
116 fig, ax = plt.subplots(figsize=(6, 4))
117 count = 0
118 for i in range(0, len(fitdflist)):
119     ax.plot(fitdflist[i]["xfit"], fitdflist[i]["yfit"]*1/max(fitdflist
    [i]["yfit"]), label=f"{normalize_concentration[count]}")
120     leg = ax.legend(framealpha=0, fontsize="small")
121     count += 1
122 plt.xlabel("Wavelength [nm]", fontsize=15)
123 plt.ylabel("Normalized Transmission", fontsize=15)
124 plt.legend(loc="upper right")
125 os.chdir("./Results/")
126 plt.savefig("W_S.png", dpi=800)
127 
128 pdf = PdfPages("W_S.pdf")
129 pdf.savefig()
130 pdf.close()
131 plt.show()
132 
133 plt.show()
134 os.chdir("..")
135 
136 # Plot Wavelength Shift/Transmission change-concentration images
137 WSlist = MaxWlist - MaxWlist[0]
138 Slist = WSlist.tolist()
139 Slist.pop(0)
140 Tlist = []
141 for i in MaxTlist:
142     Tlist.append(i - MaxTlist[0])
143 Tlist.pop(0)
144 fig, ax1 = plt.subplots()
145 ax2 = ax1.twinx()
146 ax1.plot(Mconcentration, Slist, "g-o")
147 ax2.plot(Mconcentration, Tlist, "b-o")
```

```
148 ax1.set_xlabel("Concentration [nM]", fontsize=15)
149 ax1.set_ylabel("Wavelength Shift [nm]", fontsize=15)
150 ax2.set_ylabel("Transmission change", fontsize=15)
151 os.chdir("./Results/")
152 plt.savefig("WS_T_C.png", dpi=resolution_value, bbox_inches="tight")
153 plt.show()
154 os.chdir("..")
```

List of abbreviations

AC Alternating current

ACV Alternating current voltammetry

AFM Atomic force microscopy

AuFilm Au films

AuNhA Gold nanohole arrays

AuNpA Gold nanopit arrays

Aptasensors Aptamer-based sensors

CV Cyclic voltammetry

Cy5.5 Cyanine5.5

DC Direct current

DIC Differential interference contrast

EC Electrochemical

EDL Electrical double layer

EIS Electrochemical impedance spectroscopy

ESA Electrochemical surface area

EOT Extraordinary optical transmission

Fc Ferrocene

FDTD Finite-difference time-domain

FLIM Fluorescence lifetime imaging

FOM Figure of merit

FRET Förster resonance energy transfer

FWHM Full width at half maximum

HD Hole depth

HL Helmholtz layer

HSA Human serum albumin

LDOS Local density of optical states

LOD Limit of detection

LSPR Localized surface plasmon resonance

MB Methylene blue

MEF metal-enhanced fluorescence

NIL Nanoimprint lithography

NSL Nanosphere lithography

PCR Polymerase chain reaction

PEF Plasmon-enhanced fluorescence

PML Perfectly matched layer

POC Point-of-care

QCM Quartz crystal microbalance

RIE Reactive ion etching

RSD Relative standard deviation

SAM Self-assembled monolayer

SELEX Systematic evolution of ligands by exponential enrichment

SEM Scanning electron microscopy

S protein Spike protein

SP Surface plasmons

SPR Surface plasmon resonance

SPR-M Surface plasmon resonance microscopy

SPP Surface plasmon polaritons

ssDNA Single-stranded DNA

SW Square wave

SWV Square wave voltammetry

UV-Vis ultraviolet-visible

Bibliography

[1] Deniz Sadighbayan and Ebrahim Ghafar-Zadeh. Portable sensing devices for detection of covid-19: A review. *IEEE Sensors Journal*, 21(9):10219–10230, 2021.

[2] Ziheng Hu, Yaqi Li, Gabriela Figueroa-Miranda, Simon Musal, Hangyu Li, Mateo Alejandro Martínez-Roque, Qinyu Hu, Lingyan Feng, Dirk Mayer, and Andreas Offenhäusser. Aptamer based biosensor platforms for neurotransmitters analysis. *TrAC Trends in Analytical Chemistry*, page 117021, 2023.

[3] Shiping Song, Lihua Wang, Jiang Li, Chunhai Fan, and Jianlong Zhao. Aptamer-based biosensors. *TrAC Trends in Analytical Chemistry*, 27(2):108–117, 2008.

[4] Yeon Seok Kim, Nurul Hanun Ahmad Raston, and Man Bock Gu. Aptamer-based nanobiosensors. *Biosensors and Bioelectronics*, 76:2–19, 2016.

[5] Mateusz Śmietana, Marcin Koba, Petr Sezemsky, Katarzyna Szot-Karpińska, Dariusz Burnat, Vitezslav Stranák, Joanna Niedziółka-Jönsson, and Robert Bogdanowicz. Simultaneous optical and electrochemical label-free biosensing with ito-coated lossy-mode resonance sensor. *Biosensors and Bioelectronics*, 154:112050, 2020.

[6] Suhad Abbas Abid, Ahmed Ahmed Muneer, Israa M.S. Al-Kadmy, Anas A. Sattar, Amany Magdy Beshbishy, Gaber El-Saber Batiha, and Helal F. Hetta. Biosensors as a future diagnostic approach for covid-19. *Life Sciences*, 273:119117, 2021.

[7] Li Wu, Haiwei Ji, Hanjun Sun, Chao Ding, Jinsong Ren, and Xiaogang Qu. Label-free ratiometric electrochemical detection of the mutated apolipoprotein e gene associated with alzheimer's disease. *Chemical Communications*, 52(81):12080–12083, 2016.

[8] Jiafu Chang, Wenxin Lv, Qian Li, Haiyin Li, and Feng Li. One-step synthesis of methylene blue-encapsulated zeolitic imidazolate framework for dual-signal fluorescent and homogeneous electrochemical biosensing. *Analytical Chemistry*, 92(13):8959–8964, 2020.

[9] Chutiparn Lertvachirapaiboon, Akira Baba, Sanong Ekgasit, Kazunari Shinbo, Keizo Kato, and Futao Kaneko. Transmission surface plasmon resonance techniques and their potential biosensor applications. *Biosensors and Bioelectronics*, 99:399–415, 2018.

[10] Shaopeng Wang, Xinping Huang, Xiaonan Shan, Kyle J. Foley, and Nongjian Tao. Electrochemical surface plasmon resonance: Basic formalism and experimental validation. *Analytical Chemistry*, 82(3):935–941, 2010. PMID: 20047281.

[11] Bohdan Lenyk, Gabriela Figueroa-Miranda, Ivan Pavlushko, Young Lo, Julian A Tanner, Andreas Offenhäusser, and Dirk Mayer. Dual-transducer malaria aptasensor combining electrochemical impedance and surface plasmon polariton detection on gold nanohole arrays. *ChemElectroChem*, 7(22):4594–4600, 2020.

[12] Ruifeng Zhu, Gabriela Figueroa-Miranda, Lei Zhou, Ziheng Hu, Bohdan Lenyk, Sven Ingebrandt, Andreas Offenhäusser, and Dirk Mayer. A combined plasmonic and electrochemical aptasensor based on gold nanopit arrays for the detection of human serum albumin. *Nanomaterials*, 13(16):2374, 2023.

[13] Maxime Couture, Ludovic S. Live, Anuj Dhawan, and Jean-Francois Masson. Eot or kretschmann configuration? comparative study of the plasmonic modes in gold nanohole arrays. *Analyst*, 137:4162–4170, 2012.

[14] Alisha Prasad, Junseo Choi, Zheng Jia, Sunggook Park, and Manas Ranjan Gartia. Nanohole array plasmonic biosensors: Emerging point-of-care applications. *Biosensors and Bioelectronics*, 130:185–203, 2019.

[15] Si Hoon Lee, Kyle C. Bantz, Nathan C. Lindquist, Sang-Hyun Oh, and Christy L. Haynes. Self-assembled plasmonic nanohole arrays. *Langmuir*, 25(23):13685–13693, 2009.

[16] Abdennour Abbas, Matthew J. Linman, and Quan Cheng. New trends in instrumental design for surface plasmon resonance-based biosensors. *Biosensors and Bioelectronics*, 26(5):1815–1824, 2011.

[17] Jamie Ghuman, Patricia A. Zunszain, Isabelle Petitpas, Ananyo A. Bhattacharya, Masaki Otagiri, and Stephen Curry. Structural basis of the drug-binding specificity of human serum albumin. *Journal of Molecular Biology*, 353(1):38–52, 2005.

[18] Maciej Cieplak, Katarzyna Szwabinska, Marta Sosnowska, Bikram K. C. Chandra, Pawel Borowicz, Krzysztof Noworyta, Francis D'Souza, and Wlodzimierz Kutner. Selective electrochemical sensing of human serum albumin by semi-covalent molecular imprinting. *Biosensors and Bioelectronics*, 74:960–966, 2015.

[19] Jeanethe Anguizola, Ryan Matsuda, Omar S Barnaby, KS Hoy, Chunling Wa, Erin DeBolt, Michelle Koke, and David S Hage. Glycation of human serum albumin. *Clinica chimica acta*, 425:64–76, 2013.

[20] Jian-Fei Xu, Yu-Shun Yang, Ai-Qin Jiang, and Hai-Liang Zhu. Detection methods and research progress of human serum albumin. *Critical Reviews in Analytical Chemistry*, 52(1):72–92, 2022.

[21] Xiao-Tong Ma, Xi-Wen He, Wen-You Li, and Yu-Kui Zhang. Epitope molecularly imprinted polymer coated quartz crystal microbalance sensor for the determination of human serum albumin. *Sensors and Actuators B: Chemical*, 246:879–886, 2017.

[22] Hangping Yao, Yutong Song, Yong Chen, Nanping Wu, Jialu Xu, Chujie Sun, Jiaxing Zhang, Tianhao Weng, Zheyuan Zhang, Zhigang Wu, Linfang Cheng, Danrong Shi, Xiangyun Lu, Jianlin Lei, Max Crispin, Yigong Shi, Lanjuan Li, and Sai Li. Molecular architecture of the sars-cov-2 virus. *Cell*, 183(3):730–738.e13, 2020.

[23] Mateo Alejandro Martínez-Roque, Pablo Alberto Franco-Urquijo, VÃctor Miguel García-Velásquez, Moujab Choukeife, Günther Mayer, Sergio Roberto Molina-Ramírez, Gabriela Figueroa-Miranda, Dirk Mayer, and Luis M. Alvarez-Salas. Dna aptamer selection for sars-cov-2 spike glycoprotein detection. *Analytical Biochemistry*, 645:114633, 2022.

[24] Evair D Nascimento, Wilson T Fonseca, Tássia R de Oliveira, Camila RSTB de Correia, Vitor M Faça, Beatriz P de Morais, Virginia C Silvestrini, Henrique Pott-Junior, Felipe R Teixeira, and Ronaldo C Faria. Covid-19 diagnosis by sars-cov-2 spike protein detection in saliva using an ultrasensitive magneto-assay based on disposable electrochemical sensor. *Sensors and Actuators B: Chemical*, 353:131128, 2022.

[25] Qi Song, Xindi Sun, Ziyi Dai, Yibo Gao, Xiuqing Gong, Bingpu Zhou, Jinbo Wu, and Weijia Wen. Point-of-care testing detection methods for covid-19. *Lab Chip*, 21:1634–1660, 2021.

[26] Yaofeng Zhou, Yuhao Wu, Lu Ding, Xiaolin Huang, and Yonghua Xiong. Point-of-care covid-19 diagnostics powered by lateral flow assay. *TrAC Trends in Analytical Chemistry*, 145:116452, 2021.

[27] Pablo Alberto Franco-Urquijo, Mónica Sierra-Martínez, Mariana Jarquín-Martínez, Mateo Alejandro Martínez-Roque, Victor Miguel García-Velásquez, Gustavo Acosta-Altamirano, Nancy Jannet Ruiz-Pérez, Julia Dolores Toscano-Garibay, and Luis Marat Alvarez-Salas. Fluorescence-linked aptamer assay for sars-cov-2 spike-protein: A step-by-step performance analysis in clinical samples. *Diagnostics*, 12(11):2829, 2022.

[28] William L. Barnes, Alain Dereux, and Thomas W. Ebbesen. Surface plasmon subwavelength optics. *Nature*, 424(6950):824–830, 2003.

[29] Yasa Ekşioğlu, Arif E Cetin, and Jiří Petráček. Optical response of plasmonic nanohole arrays: comparison of square and hexagonal lattices. *Plasmonics*, 11:851–856, 2016.

[30] Jonathan Calderón, Jesús Álvarez, Juan Martinez-Pastor, and Daniel Hill. Bowtie plasmonic nanoantenna arrays for polarimetric optical biosensing. In *Frontiers in Biological Detection: From Nanosensors to Systems VI*, volume 8933, pages 84–92. SPIE, 2014.

[31] Martin Bauch, Koji Toma, Mana Toma, Qingwen Zhang, and Jakub Dostalek. Plasmon-enhanced fluorescence biosensors: a review. *Plasmonics*, 9:781–799, 2014.

[32] Jian-Feng Li, Chao-Yu Li, and Ricardo F. Aroca. Plasmon-enhanced fluorescence spectroscopy. *Chem. Soc. Rev.*, 46:3962–3979, 2017.

[33] Ting Guo, Changtong Wu, Andreas Offenhäusser, and Dirk Mayer. A novel ratiometric electrochemical biosensor based on a split aptamer for the detection of dopamine with logic gate operations. *physica status solidi (a)*, 217(13):1900924, 2020.

[34] Tomasz Cwalinski, Wojciech Polom, Luigi Marano, Giandomenico Roviello, Alberto D'Angelo, Natalia Cwalina, Marcin Matuszewski, Franco Roviello, Janusz Jaskiewicz, and Karol Polom. Methylene blue-current knowledge, fluorescent properties, and its future use. *Journal of Clinical Medicine*, 9(11):3538, 2020.

[35] Y Wang, EW Plummer, and K Kempa. Foundations of plasmonics. *Advances in Physics*, 60(5):799–898, 2011.

[36] W Andrew Murray and William L Barnes. Plasmonic materials. *Advanced materials*, 19(22):3771–3782, 2007.

[37] AE Rider, Ken Ostrikov, and SA Furman. Plasmas meet plasmonics: Everything old is new again. *The European Physical Journal D*, 66:1–19, 2012.

[38] Stefan A Maier et al. *Plasmonics: fundamentals and applications*, volume 1. Springer, 2007.

[39] Anatoly V Zayats and Igor I Smolyaninov. Near-field photonics: surface plasmon polaritons and localized surface plasmons. *Journal of Optics A: Pure and Applied Optics*, 5(4):S16, 2003.

[40] Jason M Montgomery, Tae-Woo Lee, and Stephen K Gray. Theory and modeling of light interactions with metallic nanostructures. *Journal of Physics: Condensed Matter*, 20(32):323201, 2008.

[41] Hao Zhang, Mohsin Ijaz, and Richard J Blaikie. Recent review of surface plasmons and plasmonic hot electron effects in metallic nanostructures. *Frontiers of Physics*, 18(6):63602, 2023.

[42] Katherine A Willets and Richard P Van Duyne. Localized surface plasmon resonance spectroscopy and sensing. *Annu. Rev. Phys. Chem.*, 58:267–297, 2007.

[43] Ming Li, Scott K Cushing, and Nianqiang Wu. Plasmon-enhanced optical sensors: a review. *Analyst*, 140(2):386–406, 2015.

[44] Chandreyee Manas Das, Fan Yang, Zhenxu Yang, Xiaochen Liu, Quang Thien Hoang, Zhejun Xu, Shabana Neermunda, Kien Voon Kong, Ho-Pui Ho, Lining Arnold Ju, et al. Computational modeling for intelligent surface plasmon resonance sensor design and experimental schemes for real-time plasmonic biosensing: A review. *Advanced Theory and Simulations*, 6(9):2200886, 2023.

[45] William L Barnes. Surface plasmon–polariton length scales: a route to sub-wavelength optics. *Journal of optics A: pure and applied optics*, 8(4):S87, 2006.

[46] William O F. Carvalho and J Ricardo Mejía-Salazar. Plasmonics for telecommunications applications. *Sensors*, 20(9):2488, 2020.

[47] Gaurav Pal Singh and Neha Sardana. Smartphone-based surface plasmon resonance sensors: a review. *Plasmonics*, 17(5):1869–1888, 2022.

[48] Nishant Shukla, Pawan Chetri, Ratan Boruah, Ankur Gogoi, and Gazi A Ahmed. Surface plasmon resonance biosensors based on kretschmann configuration: basic instrumentation and applications. In *Recent Advances in Plasmonic Probes: Theory and Practice*, pages 191–222. Springer, 2022.

[49] Gaoling Liang, Zewei Luo, Kunping Liu, Yimin Wang, Jianxiong Dai, and Yixiang Duan. Fiber optic surface plasmon resonance–based biosensor technique: fabrication, advancement, and application. *Critical reviews in analytical chemistry*, 46(3):213–223, 2016.

[50] Edy Wijaya, Cédric Lenaerts, Sophie Maricot, Juriy Hastanin, Serge Habraken, Jean-Pierre Vilcot, Rabah Boukherroub, and Sabine Szunerits. Surface plasmon resonance-based biosensors: From the development of different spr structures to novel surface functionalization strategies. *Current Opinion in Solid State and Materials Science*, 15(5):208–224, 2011.

[51] Jules L Hammond, Nikhil Bhalla, Sarah D Rafiee, and Pedro Estrela. Localized surface plasmon resonance as a biosensing platform for developing countries. *Biosensors*, 4(2):172–188, 2014.

[52] Eleonora Petryayeva and Ulrich J Krull. Localized surface plasmon resonance: Nanostructures, bioassays and biosensing-a review. *Analytica chimica acta*, 706(1):8–24, 2011.

[53] Maya Chauhan and Vinod Kumar Singh. Review on recent experimental spr/lspr based fiber optic analyte sensors. *Optical Fiber Technology*, 64:102580, 2021.

[54] Ofer Kedem, Alexander Vaskevich, and Israel Rubinstein. Critical issues in localized plasmon sensing. *The Journal of Physical Chemistry C*, 118(16):8227–8244, 2014.

[55] KH Drexhage. Influence of a dielectric interface on fluorescence decay time. *Journal of luminescence*, 1:693–701, 1970.

[56] Chris D Geddes and Joseph R Lakowicz. Metal-enhanced fluorescence. *Journal of fluorescence*, 12:121–129, 2002.

[57] Wei Deng, Fang Xie, Henrique TMCM Baltar, and Ewa M Goldys. Metal-enhanced fluorescence in the life sciences: here, now and beyond. *Physical Chemistry Chemical Physics*, 15(38):15695–15708, 2013.

[58] Sarah Madeline Fothergill, Caoimhe Joyce, and Fang Xie. Metal enhanced fluorescence biosensing: From ultra-violet towards second near-infrared window. *Nanoscale*, 10(45):20914–20929, 2018.

[59] Seungah Lee and Seong Ho Kang. Wavelength-dependent metal-enhanced fluorescence biosensors via resonance energy transfer modulation. *Biosensors*, 13(3):376, 2023.

[60] C Joyce, SM Fothergill, and F Xie. Recent advances in gold-based metal enhanced fluorescence platforms for diagnosis and imaging in the near-infrared. *Materials Today Advances*, 7:100073, 2020.

[61] Kadir Aslan, Ignacy Gryczynski, Joanna Malicka, Evgenia Matveeva, Joseph R Lakowicz, and Chris D Geddes. Metal-enhanced fluorescence: an emerging tool in biotechnology. *Current opinion in biotechnology*, 16(1):55–62, 2005.

[62] Qiang Su, Cheng Jiang, Deming Gou, and Yi Long. Surface plasmon-assisted fluorescence enhancing and quenching: from theory to application. *ACS Applied Bio Materials*, 4(6):4684–4705, 2021.

[63] Mohsin Ali Badshah, Na Yoon Koh, Abdul Wasy Zia, Naseem Abbas, Zahra Zahra, and Muhammad Wajid Saleem. Recent developments in plasmonic nanostructures for metal enhanced fluorescence-based biosensing. *Nanomaterials*, 10(9):1749, 2020.

[64] Haiyan Liu, Chenyu Li, Jing Li, Yuqing Cheng, Junfang Zhao, Jianing Chen, and Mengtao Sun. Plasmon-enhanced fluorescence resonance energy transfer in different nanostructures and nanomaterials. *Applied Materials Today*, 30:101731, 2023.

[65] Siqi Gao, Renbin Zhou, Soham Samanta, Junle Qu, and Tymish Y Ohulchanskyy. Recent advances in plasmon-enhanced luminescence for biosensing and bioimaging. *Analytica Chimica Acta*, 1254:341086, 2023.

[66] Veeradasan Perumal and Uda Hashim. Advances in biosensors: Principle, architecture and applications. *Journal of applied biomedicine*, 12(1):1–15, 2014.

[67] Dorothee Grieshaber, Robert MacKenzie, Janos Vörös, and Erik Reimhult. Electrochemical biosensors-sensor principles and architectures. *Sensors*, 8(3):1400–1458, 2008.

[68] Vladimir Kesler, Boris Murmann, and H Tom Soh. Going beyond the debye length: Overcoming charge screening limitations in next-generation bioelectronic sensors. *Acs Nano*, 14(12):16194–16201, 2020.

[69] Fritz Scholz et al. *Electroanalytical methods*, volume 1. Springer, 2010.

[70] Haiwei Du, Xi Lin, Zhemi Xu, and Dewei Chu. Electric double-layer transistors: a review of recent progress. *Journal of Materials Science*, 50:5641–5673, 2015.

[71] André HB Dourado. Electric double layer: The good, the bad, and the beauty. *Electrochem*, 3(4):789–808, 2022.

[72] Jason Giamberardino. *Two-Electrode Measurements Of Electrostatic Double Layer Potentials With Atomic Force Microscopy*. PhD thesis, University of South Carolina, 2018.

[73] Hend S Magar, Rabeay YA Hassan, and Ashok Mulchandani. Electrochemical impedance spectroscopy (eis): Principles, construction, and biosensing applications. *Sensors*, 21(19):6578, 2021.

[74] Fred Lisdat and D Schäfer. The use of electrochemical impedance spectroscopy for biosensing. *Analytical and bioanalytical chemistry*, 391:1555–1567, 2008.

[75] Alexandros Ch Lazanas and Mamas I Prodromidis. Electrochemical impedance spectroscopy-a tutorial. *ACS Measurement Science Au*, 2023.

[76] Marwa El-Azazy, Mart Min, and Paul Annus. *Electrochemical Impedance Spectroscopy*. BoD–Books on Demand, 2020.

[77] Nurul Akmaliah Dzulkurnain, Marliyana Mokhtar, Jahwarhar Izuan Abdul Rashid, Victor Feizal Knight, Wan Md Zin Wan Yunus, Keat Khim Ong, Noor Azilah Mohd Kasim, and Siti Aminah Mohd Noor. A review on impedimetric and voltammetric analysis based on polypyrrole conducting polymers for electrochemical sensing applications. *Polymers*, 13(16):2728, 2021.

[78] Noémie Elgrishi, Kelley J Rountree, Brian D McCarthy, Eric S Rountree, Thomas T Eisenhart, and Jillian L Dempsey. A practical beginner's guide to cyclic voltammetry. *Journal of chemical education*, 95(2):197–206, 2018.

[79] Sulagna Parhi, Nilakantha Dash, Swetapadma Praharaj, and Dibyaranjan Rout. An overview of voltammetric techniques to the present era. *Electrochemical Sensors Based on Carbon Composite Materials: Fabrication, properties and applications*, pages 1–1, 2022.

[80] Richard Guy Compton and Craig E Banks. *Understanding voltammetry*. World Scientific, 2018.

[81] James F Rusling and Steven L Suib. Characterizing materials with cyclic voltammetry. *Advanced Materials*, 6(12):922–930, 1994.

[82] Shlomit Chevion, Matthew A Roberts, and Mordechai Chevion. The use of cyclic voltammetry for the evaluation of antioxidant capacity. *Free radical biology and medicine*, 28(6):860–870, 2000.

[83] Samuel P Kounaves. Voltammetric techniques. *Handbook of instrumental techniques for analytical chemistry*, pages 709–726, 1997.

[84] Jihun Han, Sukman Jang, Byung-Kwon Kim, and Kyungsoon Park. Electrochemical study of agarose hydrogels for natural convection on macroelectrodes and ultramicroelectrodes. *Journal of Analytical Science and Technology*, 14(1):10, 2023.

[85] David L Langhus. Analytical electrochemistry, (wang, joseph), 2001.

[86] Amanda L Eckermann, Daniel J Feld, Justine A Shaw, and Thomas J Meade. Electrochemistry of redox-active self-assembled monolayers. *Coordination chemistry reviews*, 254(15-16):1769–1802, 2010.

[87] SS Ermakov, DV Navolotskaya, and EA Semenova. New electrode materials and measurement technologies in voltammetry, amperometry, and coulometry. *Journal of analytical chemistry*, 74:982–992, 2019.

[88] Valentin Mirčeski, Leon Stojanov, and Sławomira Skrzypek. Recent advances and prospects of square-wave voltammetry. *Contributions, Section of Natural, Mathematical and Biotechnical Sciences*, 39(2):103–121, 2018.

[89] Valentin Mirceski, Rubin Gulaboski, Milivoj Lovric, Ivan Bogeski, Reinhard Kappl, and Markus Hoth. Square-wave voltammetry: a review on the recent progress. *Electroanalysis*, 25(11):2411–2422, 2013.

[90] Valentin Mirceski, Sławomira Skrzypek, and Leon Stojanov. Square-wave voltammetry. *ChemTexts*, 4:1–14, 2018.

[91] Maria C DeRosa, Amy Lin, Prabodhika Mallikaratchy, Erin M McConnell, Maureen McKeague, Rutika Patel, and Sarah Shigdar. In vitro selection of aptamers and their applications. *Nature Reviews Methods Primers*, 3(1):54, 2023.

[92] Bang Hyun Lee, Sang Hoon Kim, and Man Bock Gu. Biosensors: Aptamer sensors. In Roger Narayan, editor, *Encyclopedia of Sensors and Biosensors (First Edition)*, pages 363–376. Elsevier, Oxford, first edition edition, 2023.

[93] Darius Riziki Martin, Nicole Remaliah Sibuyi, Phumuzile Dube, Adewale Oluwaseun Fadaka, Ruben Cloete, Martin Onani, Abram Madimabe Madiehe, and Mervin Meyer. Aptamer-based diagnostic systems for the rapid screening of tb at the point-of-care. *Diagnostics*, 11(8):1352, 2021.

[94] C Kubiczek, Nicholas Bodenberger, and Frank Rosenau. Aptamers as promising agents in diagnostic and therapeutic applications. In *Antimicrobial Research: Novel bioknowledge and educational programs*, pages 368–378. Formatex Research Center, 2017.

[95] Michael Kohlberger and Gabriele Gadermaier. Selex: Critical factors and optimization strategies for successful aptamer selection. *Biotechnology and applied biochemistry*, 69(5):1771–1792, 2022.

[96] YC Lim, AZ Kouzani, and Wei Duan. Aptasensors: a review. *Journal of biomedical nanotechnology*, 6(2):93–105, 2010.

[97] Varnakavi Naresh and Nohyun Lee. A review on biosensors and recent development of nanostructured materials-enabled biosensors. *Sensors*, 21(4):1109, 2021.

[98] Laleh Hosseinzadeh and Mohammad Mazloum-Ardakani. Advances in aptasensor technology. *Advances in Clinical Chemistry*, 99:237–279, 2020.

[99] Marimuthu Citartan and Thean-Hock Tang. Recent developments of aptasensors expedient for point-of-care (poc) diagnostics. *Talanta*, 199:556–566, 2019.

[100] R Rajeswari and R Jothilakshmi. Modeling and simulation of plasmonic nanoparticles using finite-difference time-domain method: A review. In *Materials Science Forum*, volume 781, pages 33–44. Trans Tech Publ, 2014.

[101] Katherine Han and Chih-Hung Chang. Numerical modeling of sub-wavelength anti-reflective structures for solar module applications. *Nanomaterials*, 4(1):87–128, 2014.

[102] FL Teixeira, C Sarris, Y Zhang, D-Y Na, J-P Berenger, Y Su, M Okoniewski, WC Chew, V Backman, and JJ Simpson. Finite-difference time-domain methods. *Nature Reviews Methods Primers*, 3(1):75, 2023.

[103] Kane Yee. Numerical solution of initial boundary value problems involving maxwell's equations in isotropic media. *IEEE Transactions on antennas and propagation*, 14(3):302–307, 1966.

[104] Allen Taflove, Susan C Hagness, and Melinda Piket-May. Computational electromagnetics: the finite-difference time-domain method. *The Electrical Engineering Handbook*, 3(629-670):15, 2005.

[105] Amirmostafa Amirjani and Sayed Khatiboleslam Sadrnezhaad. Computational electromagnetics in plasmonic nanostructures. *Journal of Materials Chemistry C*, 9(31):9791–9819, 2021.

[106] Yang Hao and Raj Mittra. *FDTD modeling of metamaterials: Theory and applications*. Artech house, 2008.

[107] Zheng Zeng, Yiyang Liu, and Jianjun Wei. Recent advances in surface-enhanced raman spectroscopy (sers): Finite-difference time-domain (fdtd) method for sers and sensing applications. *TrAC Trends in Analytical Chemistry*, 75:162–173, 2016.

[108] ZhiLin Yang, QianHong Li, FangXiong Ruan, ZhiPeng Li, Bin Ren, HongXing Xu, and ZhongQun Tian. Fdtd for plasmonics: Applications in enhanced raman spectroscopy. *Chinese Science Bulletin*, 55:2635–2642, 2010.

[109] Dakota E McCoy, Anna V Shneidman, Alexander L Davis, and Joanna Aizenberg. Finite-difference time-domain (fdtd) optical simulations: a primer for the life sciences and bio-inspired engineering. *Micron*, 151:103160, 2021.

[110] José A Ribeiro, M Goreti F Sales, and Carlos M Pereira. Electrochemistry combined-surface plasmon resonance biosensors: A review. *TrAC Trends in Analytical Chemistry*, page 116766, 2022.

[111] Zohreh Hirbodvash and Pierre Berini. Surface plasmon electrochemistry: Tutorial and review. *Chemosensors*, 11(3):196, 2023.

[112] José Juan-Colás, Steven Johnson, and Thomas F Krauss. Dual-mode electro-optical techniques for biosensing applications: a review. *Sensors*, 17(9):2047, 2017.

[113] Hasan Kurt, Parsa Pishva, Zeki Semih Pehlivan, Elif Gül Arsoy, Qandeel Saleem, Mustafa Kemal Bayazıt, and Meral Yüce. Nanoplasmonic biosensors: Theory, structure, design, and review of recent applications. *Analytica Chimica Acta*, 1185:338842, 2021.

[114] Yuting Zhao, Xiaoli Cai, Chengzhou Zhu, Haipeng Yang, and Dan Du. A novel fluorescent and electrochemical dual-responsive immunosensor for sensitive and reliable detection of biomarkers based on cation-exchange reaction. *Analytica Chimica Acta*, 1096:61–68, 2020.

[115] Thorsten Liebermann and Wolfgang Knoll. Surface-plasmon field-enhanced fluorescence spectroscopy. *Colloids and Surfaces A: Physicochemical and Engineering Aspects*, 171(1-3):115–130, 2000.

[116] Thomas Neumann, M-L Johansson, Dev Kambhampati, and Wolfgang Knoll. Surface–plasmon fluorescence spectroscopy. *Advanced Functional Materials*, 12(9):575–586, 2002.

[117] Thorsten Liebermann and Wolfgang Knoll. Parallel multispot detection of target hybridization to surface-bound probe oligonucleotides of different base mismatch by surface-plasmon field-enhanced fluorescence microscopy. *Langmuir*, 19(5):1567–1572, 2003.

[118] Tianyi Chen, Jialin Xin, Shwu Jen Chang, Ching-Jung Chen, and Jen-Tsai Liu. Surface plasmon resonance (spr) combined technology: A powerful tool for investigating interface phenomena. *Advanced Materials Interfaces*, 10(8):2202202, 2023.

[119] Bin Wang and Bosoon Park. Immunoassay biosensing of foodborne pathogens with surface plasmon resonance imaging: a review. *Journal of Agricultural and Food Chemistry*, 68(46):12927–12939, 2020.

[120] Andreas B Dahlin, Bernd Dielacher, Prayanka Rajendran, Kaori Sugihara, Takumi Sannomiya, Marcy Zenobi-Wong, and Janos Vörös. Electrochemical plasmonic sensors. *Analytical and bioanalytical chemistry*, 402:1773–1784, 2012.

[121] Musashi Takenaka, Yuzo Okumura, Tomokazu Amino, Yusuke Miyachi, Chiaki Ogino, and Akihiko Kondo. Dna-duplex linker for afm-selex of dna aptamer against human serum albumin. *Bioorganic and Medicinal Chemistry Letters*, 27(4):954–957, 2017.

[122] Lei Zhou, Gabriela Figueroa-Miranda, Song Chen, Marc Neis, Ziheng Hu, Ruifeng Zhu, Yaqi Li, Michael Prömpers, Andreas Offenhäusser, and Dirk Mayer. Flexible multi-electrode arrays based electrochemical aptasensor for glycated human serum albumin detection. *Sensors and Actuators B: Chemical*, 386:133730, 2023.

[123] Walid-Madhat Munief, Florian Heib, Felix Hempel, Xiaoling Lu, Miriam Schwartz, Vivek Pachauri, Rolf Hempelmann, Michael Schmitt, and Sven Ingebrandt. Silane deposition via gas-phase evaporation and high-resolution surface characterization of the ultrathin siloxane coatings. *Langmuir*, 34(35):10217–10229, 2018.

[124] Sandra Gilles, Silke Winter, Kristin E Michael, Simone H Meffert, Pinggui Li, Kyrylo Greben, Ulrich Simon, Andreas Offenhäusser, and Dirk Mayer. Control of cell adhesion and neurite outgrowth by patterned gold nanoparticles with tunable attractive or repulsive surface properties. *Small*, 8(21):3357–3367, 2012.

[125] Ruifeng Zhu, Michael Proempers, Andreas Offenhäusser, and Dirk Mayer. Non-fully gold nanohole array fabricated by nanoimprint lithography. In *Mikro-Nano-Integration; 9. GMM-Workshop*, pages 1–4, 2022.

[126] Ferhat Aydinoglu, Faycal Saffih, Ripon Kumar Dey, and Bo Cui. Chromium oxide as a hard mask material better than metallic chromium. *Journal of Vacuum Science & Technology B*, 35(6):06GB01, 2017.

[127] T. A. Green. Gold etching for microfabrication. *Gold Bulletin*, 47(3):205–216, 2014.

[128] Caoimhe Robinson, John Justice, Jarno Petäjä, Mikko Karppinen, Brian Corbett, Alan O'Riordan, and Pierre Lovera. Nanoimprint lithography-based fabrication of plasmonic array of elliptical nanoholes for dual-wavelength, dual-polarisation refractive index sensing. *Plasmonics*, 14(4):951–959, 2019.

[129] V. Schops, B. Lenyk, T. Huhn, J. Boneberg, E. Scheer, A. Offenhäusser, and D. Mayer. Facile, non-destructive characterization of 2d photonic crystals using uv-vis-spectroscopy. *Phys Chem Chem Phys*, 20(6):4340–4346, 2018.

[130] B. Lenyk, V. Schops, J. Boneberg, M. Kabdulov, T. Huhn, E. Scheer, A. Offenhäusser, and D. Mayer. Surface plasmon-enhanced switching kinetics of molecular photochromic films on gold nanohole arrays. *Nano Lett*, 20(7):5243–5250, 2020.

[131] T. J. J. Hondrich, B. Lenyk, P. Shokoohimehr, D. Kireev, V. Maybeck, D. Mayer, and A. Offenhäusser. Mea recordings and cell-substrate investigations with plasmonic and transparent, tunable holey gold. *ACS Appl Mater Interfaces*, 11(50):46451–46461, 2019.

[132] Anshida Mayeen, Leyana K Shaji, Anju K Nair, and Nandakumar Kalarikkal. Morphological characterization of nanomaterials. In *Characterization of Nanomaterials*, pages 335–364. Elsevier, 2018.

[133] Yuxiao Zhou and Jing Du. Atomic force microscopy (afm) and its applications to bone-related research. *Progress in Biophysics and Molecular Biology*, 176:52–66, 2022.

[134] Kalsoom Akhtar, Shahid Ali Khan, Sher Bahadar Khan, and Abdullah M Asiri. Scanning electron microscopy: Principle and applications in nanomaterials characterization. *Handbook of materials characterization*, pages 113–145, 2018.

[135] Euth Ortiz Ortega, Hamed Hosseinian, María José Rosales López, Andrea Rodríguez Vera, and Samira Hosseini. Characterization techniques for morphology analysis. In *Material Characterization Techniques and Applications*, pages 1–45. Springer, 2022.

[136] Francesco Mura, Flavio Cognigni, Matteo Ferroni, Vittorio Morandi, and Marco Rossi. Advances in focused ion beam tomography for three-dimensional characterization in materials science. *Materials*, 16(17):5808, 2023.

[137] Vladka Lešer, Marziale Milani, Francesco Tatti, Živa Pipan Tkalec, Jasna Štrus, and Damjana Drobne. Focused ion beam (fib)/scanning electron microscopy (sem) in tissue structural research. *Protoplasma*, 246:41–48, 2010.

[138] Alex Peroff. What is a potentiostat and how does it work? https://pineresearch.com/dev/shop/kb/theory/instrumentation/what-potentiostat-does/, 2021.

[139] By Kasem K Kasem and Stephanie Jones. Platinum as a reference electrode in electrochemical measurements. *Platinum metals review*, 52(2):100–106, 2008.

[140] Hiroshi Kaneko, Ilva Putzier, Stephan Frings, U Benjamin Kaupp, and Thomas Gensch. Chloride accumulation in mammalian olfactory sensory neurons. *Journal of Neuroscience*, 24(36):7931–7938, 2004.

[141] Apilaasha Tharmasothirajan, Josef Melcr, John Linney, Thomas Gensch, Karin Krumbach, Karla Marlen Ernst, Christopher Brasnett, Paola Poggi, Andrew R Pitt, Alan D Goddard, et al. Membrane manipulation by free fatty acids improves microbial plant polyphenol synthesis. *Nature Communications*, 14(1):5619, 2023.

[142] Eva Kreysing, Hossein Hassani, Nico Hampe, and Andreas Offenhäusser. Nanometer-resolved mapping of cell–substrate distances of contracting cardiomyocytes using surface plasmon resonance microscopy. *ACS nano*, 12(9):8934–8942, 2018.

[143] Eva Kreysing, Silke Seyock, Hossein Hassani, Elke Brauweiler-Reuters, Elmar Neumann, and Andreas Offenhäusser. Correlating surface plasmon resonance microscopy of living and fixated cells with electron microscopy allows for investigation of potential preparation artifacts. *Advanced Materials Interfaces*, 7(6):1901991, 2020.

[144] Koji Toma, Hiroshi Kano, and Andreas Offenhäusser. Label-free measurement of cell–electrode cleft gap distance with high spatial resolution surface plasmon microscopy. *ACS nano*, 8(12):12612–12619, 2014.

[145] Koyo Watanabe, Miyazaki Ryosuke, Goro Terakado, Takashi Okazaki, Kenichi Morigaki, and Hiroshi Kano. High resolution imaging of patterned model biological membranes by localized surface plasmon microscopy. *Applied Optics*, 49(5):887–891, 2010.

[146] Jin Lu, Wei Wang, Shaopeng Wang, Xiaonan Shan, Jinghong Li, and Nongjian Tao. Plasmonic-based electrochemical impedance spectroscopy: Application to molecular binding. *Analytical chemistry*, 84(1):327–333, 2012.

[147] S Ehsan Salamifar and Rebecca Y Lai. Application of electrochemical surface plasmon resonance spectroscopy for characterization of electrochemical dna sensors. *Colloids and Surfaces B: Biointerfaces*, 122:835–839, 2014.

[148] Ricardo A Marques Lameirinhas, João Paulo N Torres, António Baptista, and Maria João M Martins. A novel analysis for light patterns in nano structures. *IEEE Photonics Journal*, 14(6):1–6, 2022.

[149] Yueyang Liu, Jiukai Fang, Yuwen Lin, Shengnan Shi, Chengzhe Di, Shan Zhang, Mingqi Sun, Yanpeng Shi, and Yifei Zhang. Enhanced optical transmission through a hybrid bull's eye structure integrated with a silicon hemisphere. *Nanomaterials*, 13(13), 2023.

[150] T. W. Ebbesen, H. J. Lezec, H. F. Ghaemi, T. Thio, and P. A. Wolff. Extraordinary optical transmission through sub-wavelength hole arrays. *Nature*, 391(6668):667–669, 1998.

[151] Bobo Du, Yinlan Ruan, Dexing Yang, Peipei Jia, Shoufei Gao, Yingying Wang, Pu Wang, and Heike Ebendorff-Heidepriem. Freestanding metal nanohole array for high-performance applications. *Photonics Research*, 8(11):1749, 2020.

[152] H. F. Ghaemi, Tineke Thio, D. E. Grupp, T. W. Ebbesen, and H. J. Lezec. Surface plasmons enhance optical transmission through subwavelength holes. *Physical Review B*, 58(11):6779–6782, 1998.

[153] Elba Mauriz and Laura M. Lechuga. Plasmonic biosensors for single-molecule biomedical analysis. *Biosensors*, 11(4), 2021.

[154] C. Zhan, B. W. Liu, Z. Q. Tian, and B. Ren. Determining the interfacial refractive index via ultrasensitive plasmonic sensors. *J Am Chem Soc*, 142(25):10905–10909, 2020.

[155] Arif E. Cetin, Dordaneh Etezadi, Betty C. Galarreta, Mickael P. Busson, Yasa Eksioglu, and Hatice Altug. Plasmonic nanohole arrays on a robust hybrid substrate for highly sensitive label-free biosensing. *ACS Photonics*, 2(8):1167–1174, 2015.

[156] Johny P. Monteiro, Leandro B. Carneiro, Mohammad M. Rahman, Alexandre G. Brolo, Marcos J. L. Santos, Jacqueline Ferreira, and Emerson M. Girotto. Effect of periodicity on the performance of surface plasmon resonance sensors based on subwavelength nanohole arrays. *Sensors and Actuators B: Chemical*, 178:366–370, 2013.

[157] Jing Jiang, Xinhao Wang, Shuang Li, Fei Ding, Nantao Li, Shaoyu Meng, Ruifan Li, Jia Qi, Qingjun Liu, and Gang Logan Liu. Plasmonic nano-arrays for ultrasensitive bio-sensing. *Nanophotonics*, 7(9):1517–1531, 2018.

[158] Zhiliang Zhang, Feng Zhao, Renxian Gao, Chih-Yu Jao, Churong Ma, Jie Li, Xiangping Li, Bai-Ou Guan, Arif E. Cetin, and Kai Chen. Rayleigh anomaly-enabled mode hybridization in gold nanohole arrays by scalable colloidal lithography for highly-sensitive biosensing. *Nanophotonics*, 11(3):507–517, 2022.

[159] Zhiliang Zhang, Feng Zhao, Renxian Gao, Chih-Yu Jao, Churong Ma, Jie Li, Xiangping Li, Bai-Ou Guan, Arif E Cetin, and Kai Chen. Rayleigh anomaly-enabled mode hybridization in gold nanohole arrays by scalable colloidal lithography for highly-sensitive biosensing. *Nanophotonics*, 11(3):507–517, 2022.

[160] Jovana Veselinovic, Suzan AlMashtoub, Sachit Nagella, and Erkin Seker. Interplay of effective surface area, mass transport, and electrochemical features in nanoporous nucleic acid sensors. *Analytical Chemistry*, 92(15):10751–10758, 2020.

[161] Changtong Wu, Andreas Offenhäusser, and Dirk Mayer. A highly sensitive amperometric aptamer biosensor for adenosine triphosphate detection on a 64 channel gold multielectrode array. *physica status solidi (a)*, 217(13):1900925, 2020.

[162] Iskandar Yahya, Muhamad Azuddin Hassan, Nur Nasyifa Mohd Maidin, and Mohd Ambri Mohamed. Swcnt network-fet device for human serum albumin detection. *Sensors*, 22(21), 2022.

[163] Wenxiang Xiao, Yaoxin Li, Yinan Xiong, ZhenCheng Chen, and Hua Li. Fluorescence turn-on detection of human serum albumin based on the assembly of gold nanoclusters and bromocresol green. *Analytical and Bioanalytical Chemistry*, 415(17):3363–3374, 2023.

[164] Wenying Gui, Xueqian Chen, and Qiang Ma. A novel detection method of human serum albumin based on cuinzns quantum dots-co2+ sensing system. *Analytical and Bioanalytical Chemistry*, 409(15):3871–3876, 2017.

[165] Ali R. Jalalvand, Sirous Ghobadi, Vali Akbari, Hector C. Goicoechea, Elahe Faramarzi, and Majid Mahmoudi. Mathematical modeling of interactions of cabergoline with human serum albumin for biosensing of human serum albumin. *Sensing and Bio-Sensing Research*, 25:100297, 2019.

[166] Tina Naghdi, Hamed Golmohammadi, Maryam Vosough, Mojgan Atashi, Iman Saeedi, and Mohammad Taghi Maghsoudi. Lab-on-nanopaper: An optical sensing bioplatform

based on curcumin embedded in bacterial nanocellulose as an albumin assay kit. *Analytica Chimica Acta*, 1070:104–111, 2019.

[167] Florian Schröper, Dorothea Brüggemann, Yulia Mourzina, Bernhard Wolfrum, Andreas Offenhäusser, and Dirk Mayer. Analyzing the electroactive surface of gold nanopillars by electrochemical methods for electrode miniaturization. *Electrochimica acta*, 53(21):6265–6272, 2008.

[168] Donna Hohertz, Sean F Romanuik, Bonnie L Gray, and Karen L Kavanagh. Recycling gold nanohole arrays. *Journal of Vacuum Science & Technology A*, 32(3), 2014.

[169] AR Shugurov, AI Kozelskaya, and AV Panin. Wrinkling of the metal–polymer bilayer: the effect of periodical distribution of stresses and strains. *RSC Advances*, 4(15):7389–7395, 2014.

[170] Hao Pei, Fan Li, Ying Wan, Min Wei, Huajie Liu, Yan Su, Nan Chen, Qing Huang, and Chunhai Fan. Designed diblock oligonucleotide for the synthesis of spatially isolated and highly hybridizable functionalization of dna–gold nanoparticle nanoconjugates. *Journal of the American Chemical Society*, 134(29):11876–11879, 2012.

[171] Sarah M Schreiner, David F Shudy, Anna L Hatch, Aric Opdahl, Lloyd J Whitman, and Dmitri Y Petrovykh. Controlled and efficient hybridization achieved with dna probes immobilized solely through preferential dna-substrate interactions. *Analytical chemistry*, 82(7):2803–2810, 2010.

[172] Lev Moiseev, M Selim Ünlü, Anna K Swan, Bennett B Goldberg, and Charles R Cantor. Dna conformation on surfaces measured by fluorescence self-interference. *Proceedings of the National Academy of Sciences*, 103(8):2623–2628, 2006.

[173] Luiza RR Santin, Sandra C dos Santos, Diogo La Rosa Novo, Daniela Bianchini, Adriana P Gerola, Gustavo Braga, Wilker Caetano, Leonardo M Moreira, Erick Leite Bastos, Ana Paula Romani, et al. Study between solvatochromism and steady-state and time-resolved fluorescence measurements of the methylene blue in binary mixtures. *Dyes and Pigments*, 119:12–21, 2015.

[174] Mary K Carroll, Marc A Unger, Andrew M Leach, Melissa J Morris, Christine M Ingersoll, and Frank V Bright. Interactions between methylene blue and sodium dodecyl sulfate in aqueous solution studied by molecular spectroscopy. *Applied spectroscopy*, 53(7):780–784, 1999.

[175] Zhenglong Zhang, Yanni Wu, Jun Dong, Wei Gao, Qingyan Han, and Hairong Zheng. Controlled plasmon enhanced fluorescence by silver nanoparticles deposited onto nanotube arrays. *Journal of Physics: Condensed Matter*, 28(36):364004, 2016.

[176] Faheng Zang, Zhijuan Su, Liangcheng Zhou, Krishnamurthy Konduru, Gerardo Kaplan, and Stephen Y Chou. Ultrasensitive ebola virus antigen sensing via 3d nanoantenna arrays. *Advanced Materials*, 31(30):1902331, 2019.

[177] Shuai Hou, Yonghao Chen, Derong Lu, Qirong Xiong, Yun Lim, and Hongwei Duan. A self-assembled plasmonic substrate for enhanced fluorescence resonance energy transfer. *Advanced Materials*, 32(8):1906475, 2020.

[178] Yi Wang, Lin Wu, Xiaodong Zhou, Ten It Wong, Jinling Zhang, Ping Bai, Er Ping Li, and Bo Liedberg. Incident-angle dependence of fluorescence enhancement and biomarker immunoassay on gold nanohole array. *Sensors and Actuators B: Chemical*, 186:205–211, 2013.

[179] G Hawa, Linda Sonnleitner, A Missbichler, A Prinz, G Bauer, and CJAB Mauracher. Single step, direct fluorescence immunoassays based on metal enhanced fluorescence (meffia) applicable as micro plate-, array-, multiplexing-or point of care-format. *Analytical biochemistry*, 549:39–44, 2018.

[180] Ying Cheng, Na Wang, Zhenxing Ren, and Chenggang Xu. Development of fluorescence-based nucleic acid blot hybridization method using cy5. 5 labeled dna probes. *Journal of Microbiological Methods*, 197:106479, 2022.

[181] Brendan Dyett, Qiming Zhang, Qiwei Xu, Xihua Wang, and Xuehua Zhang. Extraordinary focusing effect of surface nanolenses in total internal reflection mode. *ACS central science*, 4(11):1511–1519, 2018.

[182] Antonio Minopoli, Adriano Acunzo, Bartolomeo Della Ventura, and Raffaele Velotta. Nanostructured surfaces as plasmonic biosensors: A review. *Advanced Materials Interfaces*, 9(2):2101133, 2022.

[183] Ziheng Hu, Ruifeng Zhu, Gabriela Figueroa-Miranda, Lei Zhou, Lingyan Feng, Andreas Offenhäusser, and Dirk Mayer. Truncated electrochemical aptasensor with enhanced antifouling capability for highly sensitive serotonin detection. *Biosensors*, 13(9):881, 2023.

[184] Songfeng Huang, Jiajie Chen, Teliang Zhang, Xiaoqi Dai, Xueliang Wang, Jianxing Zhou, Weifu Kong, Qian Liu, Junle Qu, and Yonghong Shao. Recent advances in surface plasmon resonance microscopy. *Chemosensors*, 10(12):509, 2022.

[185] Jiying Xu, Pengfei Zhang, and Yi Chen. Surface plasmon resonance biosensors: A review of molecular imaging with high spatial resolution. *Biosensors*, 14(2):84, 2024.

[186] Angeliki Moutsiopoulou, David Broyles, Emre Dikici, Sylvia Daunert, and Sapna K Deo. Molecular aptamer beacons and their applications in sensing, imaging, and diagnostics. *Small*, 15(35):1902248, 2019.

[187] Zeinab Rahmati, Mahmoud Roushani, Hadi Hosseini, and Hamzeh Choobin. Electrochemical immunosensor with cu 2 o nanocube coating for detection of sars-cov-2 spike protein. *Microchimica Acta*, 188:1–9, 2021.

[188] Yuqi Liang, Mengmeng Xiao, Jing Xie, Jiahao Li, Yuyan Zhang, Haiyang Liu, Yang Zhang, Jianping He, Guojun Zhang, Nan Wei, et al. Amplification-free detection of sars-cov-2 down to single virus level by portable carbon nanotube biosensors. *Small*, page 2208198, 2023.

[189] Kristina Ditte, Trang Anh Nguyen Le, Oliver Ditzer, Diana Isabel Sandoval Bojorquez, Soosang Chae, Michael Bachmann, Larysa Baraban, and Franziska Lissel. Rapid detection of sars-cov-2 antigens and antibodies using ofet biosensors based on a soft and stretchable semiconducting polymer. *ACS biomaterials science & engineering*, 9(5):2140–2147, 2021.

[190] Sopan Nangare and Pravin Patil. Poly (allylamine) coated layer-by-layer assembly decorated 2d carbon backbone for highly sensitive and selective detection of tau-441 using surface plasmon resonance biosensor. *Analytica Chimica Acta*, page 341474, 2023.

[191] Meiling Zhang, Xiaodan Li, Jialin Pan, Youlin Zhang, Ling Zhang, Chenguang Wang, Xu Yan, Xiaomin Liu, and Geyu Lu. Ultrasensitive detection of sars-cov-2 spike protein in untreated saliva using sers-based biosensor. *Biosensors and Bioelectronics*, 190:113421, 2021.

[192] Antonio Minopoli, Bartolomeo Della Ventura, Bohdan Lenyk, Francesco Gentile, Julian A Tanner, Andreas Offenhäusser, Dirk Mayer, and Raffaele Velotta. Ultrasensitive antibody-aptamer plasmonic biosensor for malaria biomarker detection in whole blood. *Nature communications*, 11(1):6134, 2020.

[193] Takashi Inagaki, RN Hamm, ET Arakawa, and LR Painter. Optical and dielectric properties of dna in the extreme ultraviolet. *The journal of chemical physics*, 61(10):4246–4250, 1974.

[194] Yoh Sano. Optical anisotropy of bovine serum albumin. *Journal of colloid and interface science*, 124(2):403–406, 1988.

List of Figures

List of Tables

Curriculum Vitae

2021–Current	PhD student, RWTH Aachen University, Aachen, Germany
2019–2024	Doctoral candidate, IBI-3, Forschungszentrum Jülich GmbH, Jülich, Germany
2016-2019	Master of Engineering, University of Chinese Academy of Sciences, Beijing, China
2012-2016	Bachelor of Engineering, South China Agricultural University, Guangzhou, China
2009-2012	Feidong No.1 High School, Hefei, China
1993	Born in Anhui Province, China

Author's list of publications

Journal articles

Ruifeng Zhu, Mateo Alejandro Martínez-Roque1, Gabriela Figueroa-Miranda, Ziheng Hu, Adriano Acunzo, Hangyu Li, Qinyu Hu, Justus Bednar, Thomas Gensch, Sven Ingebrandt, Andreas Offenhäusser, and Dirk Mayer. "Plasmon-enhanced fluorescence and electrochemical aptasensor for SARS-CoV-2 Spike protein detection." *Talanta* 281 (2025): 126760.

Lei Zhou, **Ruifeng Zhu**, Gabriela Figueroa-Miranda, Marc Neis, Andreas Offenhäusser, and Dirk Mayer. "Ratiometric electrochemical aptasensor with strand displacement for insulin detection in blood samples." *Analytica Chimica Acta* (2024): 342823.

Ziheng Hu, **Ruifeng Zhu**, Gabriela Figueroa-Miranda, Lei Zhou, Lingyan Feng, Andreas Offenhäusser, and Dirk Mayer. "Truncated Electrochemical Aptasensor with Enhanced Antifouling Capability for Highly Sensitive Serotonin Detection." *Biosensors* 13, no. 9 (2023): 881.

Ruifeng Zhu, Gabriela Figueroa-Miranda, Lei Zhou, Ziheng Hu, Bohdan Lenyk, Sven Ingebrandt, Andreas Offenhäusser, and Dirk Mayer. "A Combined Plasmonic and Electrochemical Aptasensor Based on Gold Nanopit Arrays for the Detection of Human Serum Albumin." *Nanomaterials* 13, no. 16 (2023): 2374.

Lei Zhou, Gabriela Figueroa-Miranda, Song Chen, Marc Neis, Ziheng Hu, **Ruifeng Zhu**, Yaqi Li, Michael Prömpers, Andreas Offenhäusser, and Dirk Mayer. "Flexible multielectrode arrays based electrochemical aptasensor for glycated human serum albumin detection." *Sensors and Actuators B: Chemical* 386 (2023): 133730.

Ruifeng Zhu, Michael Proempers, Andreas Offenhäeusser, and Dirk Mayer. "Non-fully gold nanohole array fabricated by nanoimprint lithography." *In Mikro-Nano-Integration; 9. GMM-Workshop*, pp. 1-4. VDE, 2022.

Contributions in conferences

Ruifeng Zhu, Mateo Alejandro Martínez-Roque, Gabriela Figueroa-Miranda, Ziheng Hu, Sven Ingebrandt, Andreas Offenhäusser, Dirk Mayer. "Plasmon-enhanced fluorescence and electrochemical aptasensor for SARS-CoV-2 Spike protein detection". 4th European Biosensor Symposium, Aachen, Germany (2023)

Ruifeng Zhu, Michael Proempers, Andreas Offenhäeusser, and Dirk Mayer. "Plasmonic and electrochemical aptasensor based on non-fully gold nanohole arrays". GMM Symposium Micro-Nano-Integration (MNI), Aachen, Germany (2022)

Acknowledgements

I would like to express my sincere gratitude to all the people who supported me throughout my doctoral studies at the Institute of Biological Information Processing (IBI-3) of Forschungszentrum Jülich.

First of all, I would like to thank my direct supervisor, **Dr. Dirk Mayer**, for his discussions, the numerous suggestions, and ideas he generously provided for my experiments. His support and guidance steered my thesis in the right direction. I'm also truly grateful for the opportunity he offered me to work in his research group, I still remember how excited I was on the day I received his invitation email. Thank you.

I also want to sincerely thank **Prof. Andreas Offenhäusser** for giving me the opportunity to work in such an interdisciplinary and intercultural academic environment. Thank you again for all your support and advice in research and study.

I am also truly grateful to **Prof. Sven Ingebrandt** for being my university's reviewer, thank you for the papers and posters reviews and suggestions, and thank you for taking your precious time in reviewing my thesis.

I would also like to extend my gratitude to: **Michael Prömpers** for his introduction to cleanroom and mold fabrication, **Elke Brauweiler-Reuters** for her help in SEM, STEM, and FIB characterization, **Bettina Breuer** for her support with supplies, **Ruben Stüttgen** for his assistance in 3D printing chamber design and fabrication, **Dr. Thomas Gensch** and **Dr. Vanessa Maybeck** for their help with fluorescence spectrum, microscopy, and lifetime microscopy measurements.

I want to acknowledge my Chinese friends, **Ziheng, Lei, Ruoyan, Changtong, Qingyu, Hangyu, Song, Zidu, Jiali, Yaqi, Ruiqin, Yinglin** who offered support during the days in Germany.

Thanks to my colleagues, **Gabriela, Adriano, Marc, Mateo, Justus, Bohdan, Ivan, Antonio**, who provided help, particularly in the experimental aspects.

Especially, I am grateful for the financial support provided by the **China Scholarship Council** for my doctoral studies abroad.

Finally, I would like to thank **my wife** for her endless love and support. To **my sweet baby girl, Yanpei**, you are like an angel, a gift in my life, and your presence makes everything meaningful. And to **my parents**, thank you for helping me take care of Yanpei. I could not have completed this doctoral thesis without your support.